
NUMERICAL AND EXPERIMENTAL INVESTIGATIONS
OF PARTICLE STRESS AND FRACTURE FOR
COMPLEX-SHAPED PELLETS

Ado Farsi

Submitted for the degree of Doctor of Philosophy
and the Diploma of Imperial College

Applied Modelling and Computation Group
Department of Earth Science and Engineering
Imperial College London

June 2017

Abstract

Reactors with fixed beds of cylindrical particles have a wide application in the chemical industry. Ceramic particles are pelletized and fired to produce high porosity catalyst pellets of complex shapes. These pellets fill cylindrical reactor columns with particulate packing structures that are key to the in-service performance, but will suffer breakages, which impact on catalyst performance. The combined Finite-Discrete Element Method (FEMDEM) implemented in the Solidity code would appear to be ideally suited to capturing both the multi-body pellet interactions and pellet fracture and fragmentation. However, to put to use the Solidity code for this purpose and establish its capabilities and limitations required a substantive research programme, as reported in this PhD thesis.

Laboratory experiments were performed to evaluate the elastic and fracture properties of reference ceramic samples, as required for input parameters for computer simulation and to investigate code capability to describe fracture in such high strength and porous media for which no previous such simulations had been reported. Each set of specimens was characterised by means of micro- and nano-indentations, ultrasonic and strength tests. Standard laboratory rigs are generally too compliant for capturing the deformations of stiff and tiny ceramic specimens. For this reason, a novel digital image correlation methodology was developed to obtain both strength and stiffness from three-point bending tests on alumina bars which would have been otherwise impossible.

The effects of the catalyst support shapes on their final strength and fragmentation behaviour were investigated through controlled experiments and predominantly 2D plane stress simulations on single pellet shapes. Uniaxial compression tests and high-speed video recordings were employed to estimate the strength and fragment size

respectively. The Solidity FEMDEM code was employed to simulate the effects of geometrical features and loading orientation on the pre- and post-failure behaviour of catalyst supports.

The Solidity FEMDEM code was also used to simulate the deposition of packs of catalyst supports in cylindrical containers. A post processing tool was implemented to extrapolate the packing density profiles, packing structure, bulk porosity and orientation distributions of the resulting bodies making up the pack of pellets. The numerical results were compared with the corresponding experimental packing density profiles and orientation distributions published in the literature, together with other reported simulation results.

The final part of the thesis addresses the goal of this research which is to investigate the effects of pellet shapes on the packing and fragmentation behaviour. The findings suggest that the use of Solidity FEMDEM will have a significant industrial impact by contributing to improvements in the performance of catalysts through understanding of induced packed structures and its associated physical processes including stress and breakages.

Copyright Declaration

The copyright of this thesis rests with the author and is made available under a Creative Commons Attribution Non-Commercial No Derivatives licence. Researchers are free to copy, distribute or transmit the thesis on the condition that they attribute it, that they do not use it for commercial purposes and that they do not alter, transform or build upon it. For any reuse or redistribution, researchers must make clear to others the licence terms of this work.

Declaration

I hereby certify that the work presented in this dissertation is the result of my own investigations during the PhD project. Text and results obtained from other sources are referenced and properly acknowledged.

*Ado Farsi
May 2017*

*With four parameters I can fit an elephant,
and with five I can make him wiggle his trunk.*

John von Neumann

Acknowledgements

The three years and a half that I have spent as a doctoral student here at Imperial College have flown by so fast. In this journey I have been lucky enough to meet people without whose support this would have been a completely different experience.

First and foremost, I would like to express my gratitude to my academic supervisor, John-Paul Latham. He has always been very supportive and dedicated. His positive and open attitude contributed to creating a relaxed atmosphere for discussion and collaboration in our research group. I really appreciate all the time and effort he has put over these years to help me with my research and I hope that we will continue working together in the future.

I would also like to thank Jiansheng Xiang and Andy Pullen: Jiansheng's insights and knowledge of computational tools and Andy's knowledge of experimental techniques have given an extra input to my research and have motivated me to learn more.

I am very grateful for the financial support offered by the Engineering and Physical Sciences Research Council (EPSRC) and the Johnson Matthey Technology Centre.

In particular, I would like to say a special thanks to Michele Marigo, who has been a constant presence in my project. I would also like to thank James Bowen, Mikael Carlsson and Hugh Stitt for their continued help and support, hoping this to be just the first of many collaborations.

I would like to thank Jack Egerton for providing me with experimental and signal processing tools for my ultrasonic tests and Daniel Curry for his help in sample preparation for my mechanical tests.

I also cannot stress how much I appreciate the support I have received from my colleagues in my research group (the Applied Modelling and Computation Group), in particular Qinghua Lei, Nikos Karantzoulis, Asiri Obeysekara, Clément Joulin, Lluis Via-Estrem, Liwei Guo and Gaurav Bhutani, and from the other wonderful people I have met at Imperial, including in particular Den Zenteno Gomez, Giorgia Rossi, Peter Gordon, Renato Brito Moreira Dos Santos, John Tenant, Alessandro Chiarenza, Shahar Amitai, Yacine Debbabi, Miriam Wright, Antje Lenhart, Hamza Javed and Katarina Roele (I apologise if I have forgotten anyone, as I must surely have).

Finally, I would like to thank my father Stefano and my mother Stella for their encouragement and love, and my brother Alessandro (the other A. Farsi on Google Scholar). Last but not least, I want to thank Dario Picozzi, who motivated me to start this journey into the world of scientific research and without whose support and help nothing of this would have been possible.

Table of Contents

1	Introduction	29
1.1	Background	29
1.1.1	Research context	29
1.1.2	FEMDEM community	30
1.1.3	Industrial context	31
1.2	Problem to investigate	33
1.3	Outlines of the thesis	35
2	Mechanical characterisation of high performance ceramics	39
2.1	Introduction	39
2.2	Quasi-static testing methods	41
2.2.1	Three-point bending test	42
3	Numerical methods for fragmentation and multi-body simulations	45
3.1	Simulating fracture propagation	45
3.1.1	Introduction	45
3.1.2	FEMDEM method for fracturing systems	47
3.1.3	Bonded-DEM vs FEMDEM fracture codes	60

Table of Contents

3.2	Simulating multi-body systems	64
3.2.1	Introduction	64
3.2.2	FEMDEM method for multi-body systems	66
3.3	Applicability of DEM and FEMDEM simulations to industrial problems	67
3.3.1	Introduction	67
3.3.2	Domain of applicability of the Solidity FEMDEM code	70
4	Mechanical characterisation	73
4.1	Introduction	73
4.2	Sample preparation	74
4.3	Uniaxial compression	77
4.3.1	Brazilian discs	77
4.3.2	Four-hole cylinders	79
4.4	Ultrasonic test	82
4.5	Nanoindentations	83
4.6	Hg intrusion and BET adsorption	85
4.7	FESEM	87
4.8	Three-point bending test	89
4.8.1	Experimental setup	89
4.8.2	Flexural strength	92
4.8.3	Elastic modulus	93
4.8.4	Digital image correlation analysis	94
4.8.5	Full deflection profile calculation	95
4.8.6	Young's modulus optimisation	98
4.8.7	Uncertainty and optical distortions	100

4.9 Precision and accuracy: a comparison with the standard flexural methods	101
4.10 Comparison of the experimental results	106
4.11 Concluding remarks	112
4.11.1 Cylindrical samples	113
4.11.2 Prismatic bars	114
5 Fracture simulations	117
5.1 Introduction	117
5.2 Three-point bending test simulation	118
5.2.1 Uniaxial compression simulations	125
5.3 Mesh sensitivity analysis	128
5.4 Concluding remarks	132
5.4.1 Three-point bending tests	140
5.4.2 Artificial compliance	141
5.4.3 Brazilian tests	142
5.4.4 Structural strength of complex-shaped pellets	142
6 Packing simulations	145
6.1 Introduction	145
6.2 Axial and radial packing density profiles	149
6.3 Vertical orientation distributions and stereographic projections	151
6.4 Comparison study for packs of cylinders	153
6.5 Comparison study for packs of spheres and trilobes	158
6.6 Concluding remarks	165
6.6.1 Emergent bulk properties	166

Table of Contents

7 Conclusions and future research	169
7.1 Conclusions	169
7.2 Future research	172
References	193

List of Figures

1.1	(a) Scheme of a heated chamber used for hydrogen production. Examples of (b) packed columns and (c) catalyst supports.	32
1.2	(a) Catalyst supports crushing to fragments after several start-up and shutdown cycles. (b) Pressure drops inside the packed columns with a localised temperature gradient (dashed red box), and (c) consequent failure of the reactor.	34
2.1	Effects of the rig self-compliance in the three-point bending tests: expected (dashed red) and recorded (black) load-displacement curve from a three-point bending test on an alumina sample.	43
3.1	Scheme of the key features of the Solidity FEMDEM code: (a) compute the contact interaction and motion of bodies, (b) calculate the stresses and deformations and (c) compute the transition from continua to discontinua when fragmentation occurs.	49
3.2	Objective stress-strain curve to be modelled [Munjiza (2004)].	51
3.3	Strain softening defined in terms of displacements [Munjiza (2004)]. .	51
3.4	A schematic representation of the joint elements.	54
3.5	Single crack model with bonding stress [Munjiza (2004)].	55
3.6	Schematic representation of the crack tip.	56
3.7	Representation of stress field near the crack tip.	57

3.8	Schematic representation of discretisation near the crack tip.	58
3.9	Mohr-Coulomb failure criterion with a tension cut-off.	60
3.10	Strain softening defined in terms of displacements.	60
3.11	Relation between normal and friction force with a Coulomb model of friction.	61
3.12	Example of rheological elements of DEM for the interaction between particles [Sitharam (2000)].	62
3.13	Representation of an alumina specimen microstructure.	71
4.1	(a) Reference alumina powder and (b) compaction die that have been used to produce the four-hole cylinders. (c) Some of the samples that have been tested.	75
4.2	Two frames from the video recording of the uniaxial compression test on a cylinder without holes from Set 1: (a) before and (b) after failure. .	78
4.3	Indirect tensile strength of the <i>Small</i> (solid red) and <i>Big</i> (void red) cylinders evaluated by Brazilian disc test. Average (black) tensile strength obtained for the three sets of samples.	79
4.4	Frames from the video recording of the uniaxial compressive tests on four-hole specimens. (a) Weak and (b) strong loading orientation. . .	80
4.5	Loads at failure for the uniaxial compressive tests on the four-hole specimens from the three set of samples. Results for the (a) weak and (b) strong loading orientation.	81
4.6	Scheme with the path of the first reflected wave (yellow) and two possible paths of the transmitted wave (red and green dashed lines). .	84
4.7	Experimental data of the sound rebound time obtained from an ultrasonic test on a sample from Set 1. In particular, the Hilbert envelope (dashed black), the filter windows (dashed red) and the windowed signal (continuous black).	84
4.8	(a) Histograms, (b) original (dashed) and corrected (continuous) normal probability distributions of the Young's modulus estimations by nanoindentations for a sample of Set 1.	86

4.9	Young's modulus of the four-hole cylinders of the three sets of samples evaluated by nanoindentations.	87
4.10	(a) Pore size distributions from Hg intrusions on a sample from Set 1 (black), Set 2 (blue) and Set 3 (red) and (b) the correlation between the BET area and the pore volume from Hg intrusions.	88
4.11	FESEM images of the fracture surfaces of bar fragments showing the microstructural failure mode for the three sets of samples. The scanning of the fracture surface of a sample from Set 1 shows a fracture surface with an inter-granular morphology (a), whereas the images from Set 2 (b) and Set 3 (c) show fracture surfaces (below) and the external surface of the sample (above), without visible grain boundaries.	90
4.12	(a) Comparison of the microstructure within the thickness of the sample, respectively in black, blue and red bars and the corresponding FESEM images of the (b) left, (c) centre and (d) right portions of the cross section of a sample from Set 1.	91
4.13	Averages and standard errors of the flexural strength obtained with three-point bending tests for the three sets of bar samples.	93
4.14	(a) An example of the frames used to extrapolate the displacement field of the beam during a three point bending test, (b) the vertical displacement field d_v and (c) the horizontal displacement field d_h before failure.	96
4.15	(a) Sample configuration before (black) and during the test (red). Schematic representation of the average vertical displacement correction by applying a rigid vertical translation (b) and rotation (c) to obtain the corrected full deflection profile (d) of each frame.	97
4.16	Typical sequence of deflection profiles before failure (grey). In particular, the profile at 20% (dashed black), 60% (black) and 100% (dashed red) of peak load are shown.	98
4.17	(a) Beam configuration before and after applying a rigid body motion. (b) Optical distortion in the horizontal profile of the vertical displacement of the speckle panel during the experiment. (c) The trend of the estimated maximum errors for each frame.	102

- 4.18 (a) Representation of the points from which the vertical displacements are calculated with a standard method using three different sets of virtual displacement gauges (orange squares, blue triangles and red crosses) and the area used with the proposed methodology (black dashed line). The two arrows (green and magenta) represent the locations of two virtual strain gauges. (b) Schematic representation of the different determination of the vertical displacements with the standard method from three data points at two different locations (yellow, blue and red) and with the proposed methodology from the best interpolation of the full deflection profile (black). 107

4.19 Comparison of the force-deflection curves calculated with the standard method from the three sets of three data points (orange, blue and red) and with the proposed methodology from the best interpolation of the full deflection profile (black). 107

4.20 (a) Subset of the data shown in Figure 4.19 with force as a percentage of the peak load and limited to the range 20% and 80%. The corresponding linear trends (grey dashed lines) obtained from the Young's modulus obtained from the two curves at 20% and 80% of the peak load are also plotted for each set. (b) Comparison of the force-strain curves from the two virtual strain gauges and from the proposed methodology. The corresponding linear trends (grey dashed lines) obtained from the Young's modulus extrapolated from the three curves at 20% and 80% of the peak load are also reported in the graph. 108

4.21 Young's modulus optimisation from full displacement profiles of the bars of Set 1 (light grey), Set 2 (dark grey) and Set 3 (black). 110

4.22 Comparison of the Young's moduli from this optimisation methodology (black), ultrasonic tests (blue) and nanoindentations (red). 111

4.23 Summary of the tensile strengths evaluated for the prismatic bars (squares), small and big cylinders (circles) fired at different temperatures. The results are compared with values of strength of alumna samples with similar green densities and fired at the same temperatures that have been reported in the literature [Lam *et al.* (1994)]. . . 115

5.1	(a) Photograph of the real three-point flexural test apparatus and (b) tetrahedral mesh for the case of a 3D numerical simulation.	119
5.2	(a) Boundary conditions for the three-point flexural experiment and triangular mesh of its 2D numerical simulation. (b) Detail of the specimen discretisation and c) corresponding frame from the high-speed video.	120
5.3	Stress field in a 2D numerical model showing a crack propagating at different times during a three-point flexural test: the mean stress for each time lapse is shown on the image of the apparatus on the left and the horizontal stress is shown on the magnified beam on the right.	122
5.4	Comparison between the model of the specimen after failure in the 2D numerical simulation and a frame from the high-speed video recording of the actual experiment.	123
5.5	Comparison of the applied load and the horizontal stress experienced by the material point as sampled centrally between the two supports just within the bottom side of the beam in the 2D numerical model (red) and in the corresponding analytical solution (black).	124
5.6	Comparison of the load-deflection curve calculated in the numerical simulation (red) and obtained from a test on a bar from Set 1 (black).	124
5.7	Comparison of the deflection profile calculated in the numerical simulation (red) and obtained from a test on a bar from Set 1 (black).	125
5.8	Simulation of the uniaxial compressive test on a cylinder without holes from Set 1: (a) triangular mesh discretisation of the specimen and loading plates. (b) Horizontal tensile stress field before failure reaching the value of tensile strength in the centre of the disc. (c) Crack propagating from the centre of the disc to the two sides and (d) splitting of the two sides of the disc and post failure fragmentation. Two frames from the video recording of the uniaxial compressive test on a cylinder without holes from Set 1: (e) before and (f) after failure.	129
5.9	Load-displacement curve for the uniaxial compressive test on a cylinder without holes from Set 1: comparison between the numerical results (red) and the theoretical curve (black) calculated with equation (5.2).	130

5.10 Load-displacement curves obtained from uniaxial compressive test simulations on the four-hole specimens from Set 1 for orientation angles of: (a) 0° (red), 5° (blue), 10° (orange), 15° (green), 20° (magenta) and (b) 25° (red), 30° (blue), 35° (orange), 40° (green) and 45° (magenta).	131
5.11 Boundary conditions for the Brazilian test of a ceramic pellet with four holes diametrically compressed against two steel plate and triangular mesh of its 2D numerical simulation.	132
5.12 a) Time-lapse numerical results immediately before failure and after failure. Two frames from the video recording of the uniaxial compressive test on a cylinder with four holes from Set 1: (b) before and (c) after failure.	133
5.13 Numerical simulations of the the uniaxial compression tests on the disc with four holes loaded in different orientations.	134
5.14 Relation between the loading orientation and the structural strength of four-hole pellets, normalised with respect to the strength of an equivalent cylinder of identical geometry without holes. Experimental (dots) and numerical (dashed lines) results for Set 1 (blue), Set 2 (black). Experimental results for the weak orientation for Set 3 (red).	134
5.15 Mesh sensitivity analysis for the three-point bending test simulations: (a) triangular mesh discretisation of the test setup and (b) detail of the 1 mm mesh for the bar. (c) Detail of the 150 μm mesh of the bar. (d) Detail of the 100 μm mesh of the bar.	135
5.16 Mesh sensitivity analysis for the three-point bending test simulations: comparison of the load-deflection curve calculated in the numerical simulations for the 1 mm (blue), 150 μm (green), 100 μm (red) mesh and obtained from a test on a bar from Set 1 (black).	136
5.17 Mesh sensitivity analysis for the three-point bending test simulations: comparison of the deflection profile calculated in the numerical simulations for the 1 mm (blue), 150 μm (green), 100 μm (red) mesh and obtained from a test on a bar from Set 1 (black).	136

5.18 Mesh sensitivity analysis for the uniaxial compression test simulations: triangular mesh discretisation of the test setup for the $150 \mu m$ mesh. The mesh is then rotated of 10° , 20° and 30° to preform a comparison of four different mesh realisations with the same element size.	137
5.19 Mesh sensitivity analysis for the uniaxial compression test simulations: triangular mesh discretisation of the test setup for the $100 \mu m$ mesh. The mesh is then rotated of 10° , 20° and 30° to preform a comparison of four different mesh realisations with the same element size.	138
5.20 Mesh sensitivity analysis for the uniaxial compression test simulations: comparison of the load-displacement curve calculated in the numerical simulations for the $150 \mu m$ mesh obtained with 0° (yellow), 10° (green), 20° (blue) and 30° (red) rotation of the original mesh of the disc. The numerical results are compares to the theoretical curve given by the experimental results for Set 1 (black).	139
5.21 Mesh sensitivity analysis for the uniaxial compression test simulations: comparison of the load-displacement curve calculated in the numerical simulations for the $100 \mu m$ mesh obtained with 0° (yellow), 10° (green), 20° (blue) and 30° (red) rotation of the original mesh of the disc. The numerical results are compared to the theoretical curve given by the experimental results for Set 1 (black).	139
6.1 Numerical discretisation of the cylindrical container using the geometry from the experiments presented in Caulkin <i>et al.</i> (2015).	147
6.2 Numerical discretisation of a) the solid simple cylindrical pellet named A38 as used in Caulkin <i>et al.</i> (2015), b) a cylindrical pellet with one hole and c) a tridecagram-shaped pellet.	148
6.3 Final simulated packing structures for the three particle geometries; details of the pack of a,d) A38 cylinders, b,e) one-hole cylinders and c,f) tridecagram-shaped pellets	148
6.4 Representation of the regular grid in the domain of the numerical results. Note, a much finer voxel size is actually used to calculate the solid volume fraction in each slice.	150

6.5 a) Averaging the values of cells along horizontal planes; b) axial packing density profile, c) averaging the values of cells along vertical columns; d) visualisation of the simulated average packing density as if observed perpendicular to the axis of the container together with superimposed radial packing density profile showing periodic wall effect as also seen in the visualisation.	151
6.6 a) Angle between the axis of the catalyst support and the axis of the container; b) plotted pellet orientations as they would appear from above the container; c) stereographic projection of the orientations of a cylindrical catalyst support packed structure.	153
6.7 Axial packing density distributions extrapolated from the X-Ray CT scans (in black) from Caulkin <i>et al.</i> (2015), and from the numerical simulations of simple cylindrical catalysts with different values for friction and damping coefficients (in blue, green, red and yellow). . .	155
6.8 Radial packing density distributions extrapolated from the X-Ray CT scans (in black) from Caulkin <i>et al.</i> (2015), and from the numerical simulations of simple cylindrical catalysts with different values for friction and damping coefficients (in blue, green, red and yellow). . .	156
6.9 Vertical orientation distributions extrapolated from the X-Ray CT scans (in black) from Caulkin <i>et al.</i> (2015), and from the numerical simulations of simple cylindrical catalysts with different values for friction and damping coefficients (in blue, green, red and yellow). . .	156
6.10 Stereographic projections representing the pellet orientations of the numerical simulations with four combinations of friction and damping coefficients.	157
6.11 Numerical discretisation of particle geometry a) spherical glass bead and b) trilobe ceramic pellet as used for the experiments in Nguyen <i>et al.</i> (2005).	160
6.12 Deposition process for the simulated packing structures of the two particle geometries: a) glass beads and b) trilobe pellets.	161
6.13 Final simulated packing structures of the two particle geometries; pack of a) glass beads and b) trilobe pellets.	161

6.14	Packing density fluctuations in spheres: radial packing density distributions extrapolated from the X-Ray CT scans (in black) from Nguyen <i>et al.</i> (2005), and from the numerical simulations in a cylindrical container (red)	162
6.15	Packing density fluctuations in trilobes: radial packing density distributions extrapolated from the X-Ray CT scans (in black) from Nguyen <i>et al.</i> (2005), and from the numerical simulations in a cylindrical container (red)	162
6.16	Variation of packing density in spheres: average packing density perpendicular to the axis of the container as sampled within each x,y location as described in Section 6.2.	163
6.17	Variation of packing density in trilobes: average packing density perpendicular to the axis of the container as sampled within each x,y location as described in Section 6.2.	163
6.18	Axial packing density variations extrapolated as derived from the numerical simulations of spheres (continuous line) and trilobes (dashed line) in a cylindrical container.	164
6.19	Orientation distribution derived from the numerical simulations of packing of trilobes in a cylindrical container.	164
6.20	Stereographic projections representing the pellet orientations as derived from the numerical simulations of packing of trilobes in a cylindrical container.	165
7.1	(a) Intrinsic and (b) extrinsic cohesive law or traction separation law. They are also known as initially elastic and initially rigid traction separation laws [Nguyen (2014)]	173
7.2	Grains constituting the microstructure of a ceramic sample and their equivalent in a simulated volume of ceramic.	176
7.3	A statistical reconstruction of 3D volume from 2D sections.	176

7.4	Different boundary conditions that can be applied to the representative volume to reconstruct the mechanical behaviour of the grain structure and infer the parameters that best describe both ceramics and rocks at the macroscale.	177
7.5	Dynamic three-point bending experiments on bars from Set 1 recorded with (a) standard and (b) high-speed camera.	179
7.6	Triangular mesh of the 2D numerical simulation of a dynamic three-point bending test.	180
7.7	Horizontal displacement field in a 3D numerical model of a dynamic three-point bending test.	180
7.8	Comparison between the model of the specimen (a) before and (b) after failure in the 2D numerical simulation and a frame from the high-speed video recording of the actual dynamic three-point bending experiment.	181
7.9	Double peak in the load-time response of dynamic three-point bending experiments on three sample bars from Set 1.	182
7.10	Fragmentation of a cylindrical pellet with four holes during an impact at 3 m/s against a steel plate.	182
7.11	(a) Scheme and (b) actual rig for the AMCG's pressure sensors that can be employed to obtain experimental statistics of contact force history.	185
7.12	Cylindrical caged shaped pellet with four holes: (a) photograph and (b) its equivalent numerical mesh.	186
7.13	Mesh discretisation of the collapsed pile after lifting the container. . .	186
7.14	Collapsing pile after filling a cylinder (1-2) and lifting it up (3-4). . .	187
7.15	Force chains and the magnitude of the maximum contact force [N] experienced by cylindrical pellets of 2mm diameter with one central hole.	189
7.16	Preliminary simulations of the stresses experienced by cylindrical pellets in a container.	191

List of Tables

3.1	Required parameters for simulating fragmentation with FEMDEM. . .	61
3.2	Material properties of partially dense alumina samples [Lam <i>et al.</i> (1994)] and their numerical discretisation constraints.	72
4.1	Average of the measured dimensions and bulk density of the tested prismatic specimens.	76
4.2	Average of the measured dimensions and bulk density of the tested specimens.	76
4.3	Mean values and standard errors of the Young's moduli from this optimisation methodology, ultrasonic tests and nanoindentations. . .	111

Chapter
ONE

Introduction

1.1 Background

1.1.1 Research context

The Applied Modelling and Computation Group (AMCG) at Imperial College London is working on the development and the application of innovative modelling techniques in earth, nuclear, engineering and biomedical sciences. The group has principal research interests in the development and application of numerical methods for fluids including ocean, atmosphere, and industrial multi-phase flows, for neutral particle radiation transport, for optimization mathematics and its applications, and for the solution of inverse problems. Among other projects, the group is developing the Solidity FEMDEM code, a suite for numerical simulations previously named Virtual Geoscience Simulation Tools (VGeST). This computational tool is based on the combined finite-discrete element method (FEMDEM) and it is employed for

the analysis of discontinuous systems (i.e. elastic-plastic deformations and fracture propagation) and has also been coupled with thermal and fluid fields. There are many examples of engineering problems that are being approached with this technology at the AMCG. For instance, the description of the packing process and of the flow of granular materials has an important application in geoscience for the description of granular avalanches. The same tool has also been applied to the costal engineering field, where this technology is employed to investigate the behaviour of armour unit systems at the scale of unit interactions and at the scale where the solid material as a whole is performing as a granular system. An important aspect of novelty of the Solidity FEMDEM code is that not only permits to describe the motion and interaction of many distinct bodies, but also let to investigate the mechanical solicitations that deform and fracture the bodies. This kind of analysis finds many applications in geomechanics and structural engineering in order to simulate fracturing of quasi-brittle materials. Other possible fields of application are the food, powder and chemical technology, mixing, etc.

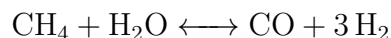
1.1.2 FEMDEM community

Generic algorithms for FEMDEM simulations in 2D and 3D started to be proposed from the early 90s. Extensive developments and applications of the FEMDEM method have been carried out after the release of the open source Y-code in Munjiza (2004), and different versions have been released, including the code developed from the collaboration between Queen Mary University and Los Alamos National Laboratory [Munjiza (2004); Munjiza *et al.* (2015); Rougier *et al.* (2014)], the Y-Geo and Y-GUI software that have been developed by the Grasselli's Geomechanics Group at Toronto University [Mahabadi *et al.* (2010b, 2012)], and VGeST (Virtual Geoscience Simulation Tools) released by the Applied Modelling and Computation

Group (AMCG) at Imperial College London [Xiang *et al.* (2009a); Munjiza *et al.* (2010)]. Recently the AMCG has upgraded and renamed VGeST as 'Solidity'. A commercial FEMDEM code developed by Geomechanica (www.geomechanica.com), has also been released in Canada, although its application has been limited to modelling rock fracture. While the first Y-code employed finite strain elasticity coupled with a smeared crack model to capture deformation, rotation, contact interaction and fragmentation, the AMCG has greatly improved the code, implementing a range of constitutive models in 3D [Karantzoulis *et al.* (2013); Guo (2014)], thermal coupling [Joulin *et al.* (2017)], parallelisation and a faster contact detection algorithm [Xiang *et al.* (2017)].

1.1.3 Industrial context

Many industrial manufacturing processes require hydrogen or one of its derivatives as a reactant, particularly in the petrochemical industries. Usually, hydrogen is produced from hydrocarbon feed via reforming using mixtures of steam reforming and partial oxidation. Steam reforming of the simple hydrocarbon methane occurs with the following reaction [Wagman *et al.* (1945)]:



This reaction is highly endothermic and it is normally performed in multi-tubular fixed-bed reactors. The multiple tubes, which constitute the multi-tubular reactors, are filled with catalysts and the heat carrier circulates externally around the pipes, as shown in Figure 1.1(a) and 1.1(b).

The catalyst typically employed for hydrogen production contains an active nickel (Ni) metal component supported on porous materials with a high surface area, most commonly alumina (aluminium oxide, Al_2O_3) [Rostrup-Nielsen & Rostrup-

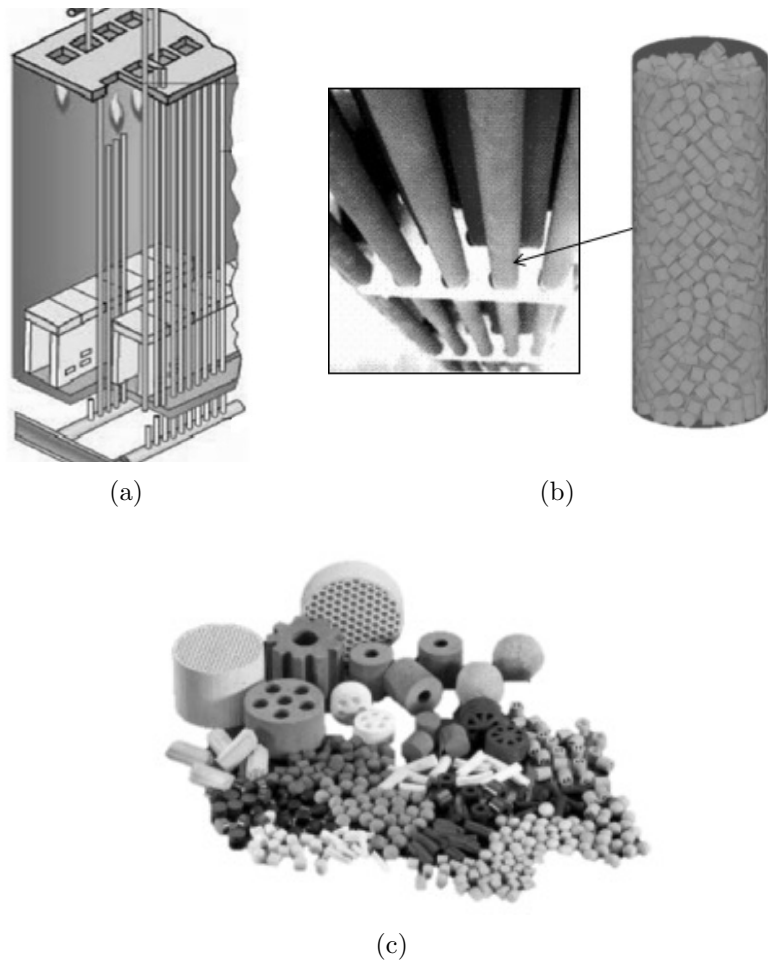


Figure 1.1: (a) Scheme of a heated chamber used for hydrogen production. Examples of (b) packed columns and (c) catalyst supports.

Nielsen (2002)]. To maximize the available surface area and increase heat transfer, these media can be shaped as pall rings, cylindrical pellets, balls or more complex configurations, as shown in Figure 1.1(c). Although fixed-bed reactors are commonly used for highly endothermic reactions, this method brings with it the following problem: after several start-up and shutdown cycles, as shown in Figure 1.2(a), catalysts are partially crushed to fragments due to the different thermal expansion properties between the metal tube and ceramic media. The accumulation of these fragments in turn causes pressure drops inside the tubes: at the same time a local decrease in efficiency of the reaction and an increase of the temperature occurs, as shown in Figure 1.2(b), and this can even cause the failure of the steel tube reactor, as shown in Figure 1.2(c). Pressure drops can also affect the reactor to the point that the catalysts must be removed and replaced every three to five years instead of the optimal ten years. This recurring event has a significant negative impact on plant lifecycle costs (costs for replacements and missing production during the plant downtime). A better understanding of fracture propagation in packed structures of ceramic bodies is crucial in minimising these effects and could also be relevant for further innovations and developments of the fixed-bed reactor technology.

1.2 Problem to investigate

The purpose of this research was to investigate particle stress and fracture propagation in packed bed structures employing a combined finite-discrete element method. This technology enables the modelling of a large number of interacting distinct bodies, each associated with a separate finite element mesh. Continuous deformations are modelled through finite elements while discontinuous behaviours, such as fractures, are analysed by discrete elements. For this reason a combined finite-discrete element method simulation not only allows accurate reconstruction of the packing

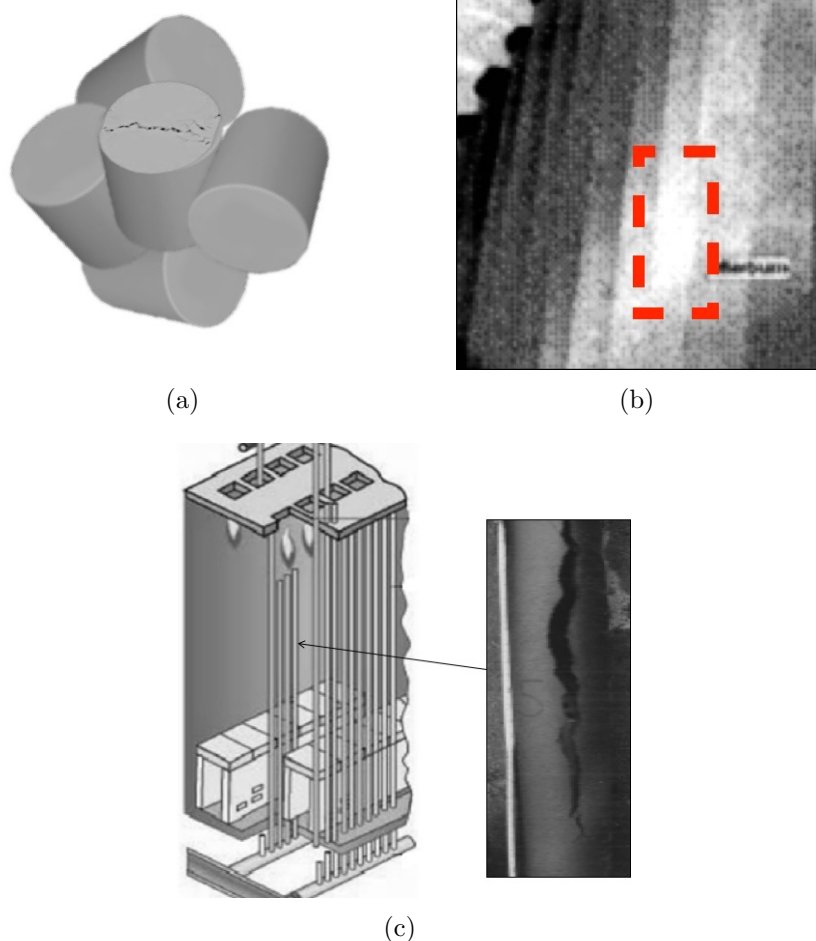


Figure 1.2: (a) Catalyst supports crushing to fragments after several start-up and shutdown cycles. (b) Pressure drops inside the packed columns with a localised temperature gradient (dashed red box), and (c) consequent failure of the reactor.

process, yielding to values for the location and the orientation of each particle in the reactor, but also reveals how stress chains form within packed structures under mechanical solicitations. The goal of this research project is therefore to achieve a better understanding of different pellet shapes and their inherent mechanical properties by means of numerical simulations, the findings of which could be of industrial interest by contributing to improvements in the performance of catalysts. To obtain realistic simulations of fracture propagation of ceramic pellets it is essential to first characterise the mechanical properties of the material that makes up the particles, and then compare the numerical results of idealised experimental conditions with the actual experiments to validate the code for use with such materials.

1.3 Outlines of the thesis

Chapter 2 summarises the standard test methods addressed to the study of the mechanical characterisation of small engineered high performance materials.

Chapter 3 reviews the literature addressed to the simulation of fragmentation and multi-body systems. The review will be essentially focused on the mechanical characterisation of porous ceramics and the simulation of pellet fragmentation and mono-shape, mono-sized systems with the discrete element method (DEM) and the combined finite-discrete element method (FEMDEM). An additional discussion on the applicability and possible advantages of the two methods concludes this section.

Chapter 4 presents the experimental work that have been carried out to determine the material properties of the porous ceramic materials used for the detailed fragmentation study with Solidity FEMDEM numerical simulation illustrated in Chapter 5. This characterisation work has been tackled in this research by employing different testing techniques, including uniaxial compression (Brazilian disc test), ul-

trasonic test, nanoindentations, mercury (Mg) intrusion, Brunauer-Emmett-Teller (BET) adsorption and three-point bending test. A novel optimisation algorithm that have been developed for the characterisation of the Young's modulus of small, highly stiff engineered materials is also introduced. Material presented in this chapter has appeared in the following publication:

Farsi A, Pullen AD, Latham JP, Bowen J, Carlsson M, Stitt EH, Marigo M. 2017. Full deflection profile calculation and Young's modulus optimisation for engineered high performance materials, Scientific Reports, 7, 46190. doi:10.1038/srep46190 (Nature research open access journal, 5-year impact factor: 5.525).

In Chapter 5, the Solidity FEMDEM code is used to first investigate its capabilities in the simulation of fragmentation of porous ceramic specimens, and then to investigate the structural strength of complex-shaped pellets under simplified loading conditions. Moreover, the focus of this chapter is on proving through a series of validation studies that the method can also be applied to fracture of very strong (by comparison with most geomaterials) porous ceramic bodies and to find possible limitations of the method. The chapter therefore follows a progression from simple specimen geometry strength tests simulations (i.e. three-point bending tests and Brazilian disc tests) towards more complex shape specimens. This chapter ends with an example of the code capabilities to design pellets shapes suitable to deliver advantages for the catalyst performance. Here the Solidity FEMDEM code is used to investigate the relation between the structural strength of complex-shaped pellets and the orientation of simplified loading conditions, representing the mechanical loads of the pellets in a reactor. Material presented in this chapter has appeared in the following publication:

Farsi A, Xiang J, Latham JP, Pullen AD, Carlsson M, Stitt EH, Marigo M. 2015. An application of the finite-discrete element method in the simulation of ceramic

breakage: Methodology for a validation study for alumina specimens, Proceedings of the 4th International Conference on Particle-based Methods

Chapter 6 focuses on reproducing experimental packing results when pellets are released into cylindrical containers. Solid cylindrical, spherical and complex-shaped (trilobes) catalyst supports once at-rest in their cylindrical containers are compared to the corresponding experimental results from X-Ray CT scans. The numerical results are analysed with a post-processing tool that has been specifically developed to reproduce the calculation process employed to evaluate the axial and radial packing density profiles and the pellet orientation distribution from the voxelised data format of the X-Ray CT scans employed in the literature. Material presented in this chapter has appeared in the following publication:

Farsi A, Xiang J, Latham JP, Carlsson M, Stitt EH, Marigo M. (2017) Simulation and characterisation of packed columns for cylindrical catalyst supports and other complex-shaped bodies, Proceedings of the 7th International Conference on Discrete Element Methods (This paper was awarded *Best Student Paper* by the conference organisers).

Chapter 7 gives an outline of the main findings discussed in the thesis and of proposed new developments.

Chapter
TWO

Mechanical characterisation of high performance ceramics

2.1 Introduction

Significant recent advancements achieved in manufacturing technology, including the new opportunities made possible by additive layer manufacturing (3D printing) have opened the doors to a range of new engineered materials with complex architectures and enhanced mechanical properties [Lewis *et al.* (2006); Fu *et al.* (2011); Zheng *et al.* (2014); Roohani-Esfahani *et al.* (2016)]. The scope of this research was to study resistant catalytic pellets that can reduce costs in the production of hydrogen, ammonia and other industrial chemicals; but high-performance mechanical components that exhibit high strength and stiffness have found useful applications in different fields in medicine, engineering and technology: stronger and more reli-

able artificial bones can improve the lives of bone cancer patients; the pellets that make up the nuclear fuel in the core of nuclear power plants. In all of these applications, computational tools and numerical simulations have become essential as effort is focussed on process optimisation [Schlereth & Hinrichsen (2014); Palma *et al.* (2016); Deng *et al.* (2001); Helfer *et al.* (2015); Michel *et al.* (2008)]. However, the mechanical properties of this kind of materials are significantly affected by their microstructural design and by the sintering process [Wang *et al.* (2002); Wötting & Ziegler (1985)], (i.e. the geometry and scale of the finished product, type of powder, compaction, extrusion or printing tools, firing time and temperature). Consequently, it is critical that characterisation of the mechanical behaviour of these materials is carried out rigorously and on specimens representative of the final product.

Since porous ceramics are generally considered to be brittle elastic [David (2015)], Young's modulus and tensile strength are two of the main parameters needed in order to predict the mechanical behaviour of systems made from such components. A variety of methods to determine the Young's modulus can be found in the literature: they can be broadly categorised as either dynamic or quasi-static. Dynamic methods (such as ultrasonic, prism resonance and impulse excitation tests) typically use knowledge of the density and geometry of specimens, together with measurements of a dynamic response to a transient or cyclic loading. Quasi-static methods (such as micro- and nanoindentations, direct compression and tension tests, flexural tests) use the deformation or strain response of a specimen to a series of constant loads or a continuous loading applied at a low rate such that inertial effects can be ignored.

Dynamic methods such as resonance frequency methods and ultrasonic tests on the one hand need very little sample preparation and the inferred elastic constants can be related to the static Young's moduli [Ledbetter (1993)]. Because of their sintering processes, many of these materials can only be cast into small pellets, and wave scattering and difficulties in the alignment of tiny samples with the emitting

and receiving beams can sometime constitute a disadvantage in employing these methods.

2.2 Quasi-static testing methods

Nanoindentations are widely employed to characterise the elastic properties and the mechanical behaviour of materials at the micro- and nanoscale [Oliver & Pharr (2004); Pan *et al.* (2016)]. They require high-resolution testing equipment and in some cases also time and particular tools for the sample preparation (i.e. grinding, polishing, etc.). In the context of ceramics, this technique is particularly well suited when applied for the characterisation of the properties of thin films and small samples such as ceramic coatings and small structural features. To increase the accuracy of the tests, the indentations are generally repeated in a certain area of the sample. However, the resulting Young's modulus distributions need to be interpreted as the repeatability is significantly dependent on the experience of the operator. In addition, the inferred Young's modulus reflects the features of the indented portion of the tested material (such as the external surface) and may not be representative of the structural behaviour of the sample at the macroscale.

When possible, other quasi-statically determined parameters such the elastic modulus from uniaxial compression and the flexural modulus, are generally preferred because they require more conventional and simpler testing machineries and specimen preparation. In addition, they are also generally considered to be more representative of in-service loading conditions [Eissa & Kazi (1988)]. One of the main advantages that these tests offer, compared to dynamic methods, is that they can provide an estimate for both the strength and the stiffness of the material with a single experiment. While the strength is just a function of the sample geometry and the load at failure, Young's modulus is also related to the relation between the

applied loads and the corresponding deformations in the sample (i.e. the recorded displacements). Since the deformations of highly stiff materials are inevitably small and therefore not easy to determine with a high level of confidence, the estimated Young's modulus can be significantly affected by experimental errors. Bending tests, compared to uniaxial compressions, have the advantage of emphasising the response of the tested sample to the applied loads, effectively increasing the measurable deformations of the sample during the test.

2.2.1 Three-point bending test

The EN 843-2:2006 Section 4 [British Standards Institution (2007)] describes how the three-point bending test can be employed to evaluate Young's modulus using either the test rig cross-head displacement (Method A.1), displacement transducers (Method A.2) or strain gauges (Method A.3). The Method A.1 is generally not applicable because of the effects of standard rig self-compliance in a three-point bending test for the case of particularly stiff sample bars. This is caused by the great ratio between the applied load and the relatively small deformations of the samples before failure. A typical example for such stiff materials of load-displacement curve of the three-point bending test, shown here for a porous alumina sample, is given in Figure 2.1. About 80% of the total displacement recorded by the rig (continuous line) is not representative of the actual alumina beam deflection but is likely to be due to load-frame compliance, based on the expected specimen displacement (dashed-line). Although EN 843-2:2006 Section 4.4 suggests to repeat the test on a thick metal or ceramic bar to estimate the rig self-compliance, the accuracy of the estimated Young's modulus relies on the assumptions that the thick sample is perfectly rigid and that the rig is responding with the same self-compliances to the transmitted loads, and this might not be true for all the actuators.

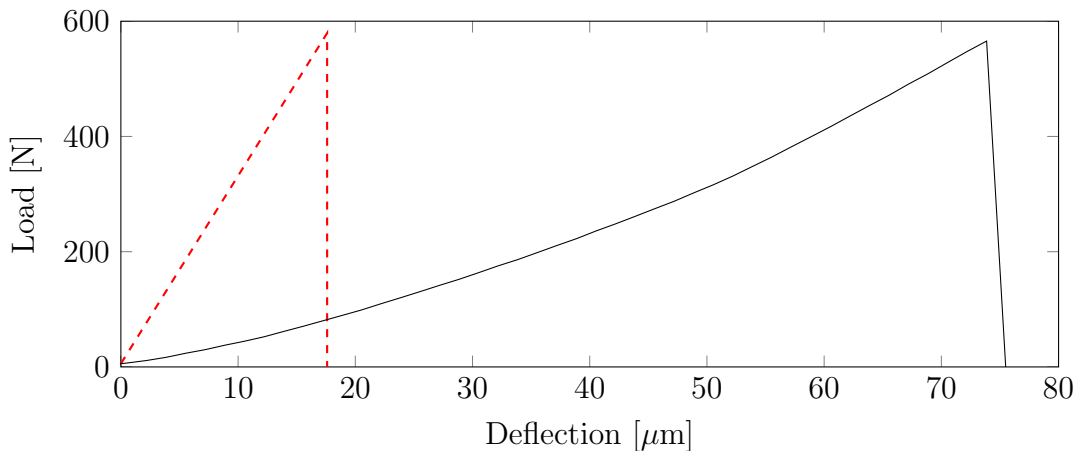


Figure 2.1: Effects of the rig self-compliance in the three-point bending tests: expected (dashed red) and recorded (black) load-displacement curve from a three-point bending test on an alumina sample.

Methods A.2 and A.3 are also not convenient when the specimens are too small to allow a standard transducer or strain-gauge to be accurately installed and employed with a high level of confidence. Digital Image Correlation (DIC) is a non-contact optical method that can be employed for monitoring displacements and deformations from sequences of images [Hild & Roux (2006); Pan *et al.* (2009); Dupré *et al.* (2010); Roux *et al.* (2012)]. This technique can be used to emulate either the arrangement of transducers or the strain gauge as described in Method A.2 and A.3 respectively. Optical observation methods make it possible to eliminate the test rig compliance by tracking discrete optical targets, e.g. discrete markers placed on the two supports and the loading plate in the three-point bending test. It is also possible to average the displacements of a number of random markers in an area expanded around the discrete targets to increase the accuracy of the tracked displacements. Although relatively easy to implement, these methods of harnessing optically recorded data only use data from limited regions of each image, effectively discarding most of the available information. This gave an opportunity for the development of a more reliable method that uses all of the available image deformation

data during bending tests, leading to higher levels of accuracy in deflection calculation and therefore in Young's modulus evaluation. This optimisation methodology is described in Chapter 4, where the results are compared with the ones obtained from other standard tests.

Chapter

THREE

Numerical methods for fragmentation and multi-body simulations

3.1 Simulating fracture propagation

3.1.1 Introduction

Interest in simulating fracture propagation extends across a variety of scientific and engineering fields, such as structural analysis, material design, nuclear waste disposal risk assessment, oil and gas reservoir engineering, and subsurface ore mining [Paluszny & Zimmerman (2011)]. Numerical simulations are performed in order to predict the formation and behaviour of these fracture systems, due to the geomet-

ric and physical complexity inherent in fracture phenomena. Two main modelling approaches can be identified in the literature for fracture analysis: discrete crack and smeared crack models, also known as geometric/non-geometric, or grid/subgrid methods. They were introduced in the late 1960s by Ngo and Scordelis and Rashid in application to the concrete structural analysis [Borst *et al.* (2004)]. The smeared crack model is based on the assumption that in concrete, due to its heterogeneity and the presence of reinforcement, many small cracks nucleate which only in a later stage of the loading process link up to form one or more dominant cracks. Since each individual crack is not numerically resolved, the smeared crack model captures the deterioration process through a constitutive relation, thus smearing out the cracks over the continuum. In this kind of analysis cracks are represented as an isotropic or anisotropic damage concentration band within a mesh element from which fracture geometry can be inferred, instead of being explicitly defined [Jirasek (1998)]. In contrast, the discrete crack model represents cracks discretely and aim to simulate the initiation and propagation of dominant cracks. This kind of analysis can be performed with different approaches, e.g. boundary element based methods (BEM) Carter (2000), peridynamics [Silling (2000); Silling *et al.* (2003)], finite element simulations (FEM) [Lin & Smith (1999); Schöllmann *et al.* (2003)] extended finite element method (XFEM) [Bordas & Nguyen (2007)], discrete element method (DEM) [Sitharam (2000); Tavarez (2007); Huang *et al.* (1999); Wan (2011); Petytody & Cundall (2004)] or combined finite-discrete element method (FEMDEM) [Munjiza (2004)]. An important aspect to underline is that the great majority of geometric methods do not maintain a representation of the fractures separate from the mesh, and rely on mesh editing techniques, such as in situ insertion of new crack nodes, edges and faces, to capture mesh growth. There are also several approaches presented in the literature aimed at describing solid fragmentation using DEM. In Huang *et al.* (1999) numerical simulations of uniaxial compression and

cutting processes of rock have been presented employing packed discrete elements bonded together to represent the bulk rock material. Similar examples are presented to describe tunnelling, flexural and Brazilian tests in Potyondy & Cundall (2004), and powder agglomerates in Liu *et al.* (2010). The standard approach consists of defining a packed structure of particles (generally spheres) with a determined particle size distribution and then defining laws for the contact and interactions between particles (Figure 3.12) on the basis of parameters such as penalty numbers, stiffness of the bonding, etc. and to obtain forces that, once they are applied to the elements, define the movement of the simulated bodies with Newton's laws of motion. These bonded-DEM approaches will be discussed in Section 3.1.3.

3.1.2 FEMDEM method for fracturing systems

3.1.2.1 Introduction

Algorithms for FEMDEM simulations started to be proposed from the 90s. Extensive developments and applications of the FEMDEM method have been carried out after the release of the open source Y-code in Munjiza (2004), and different versions have been released, including the code developed from the collaboration between Queen Mary University and Los Alamos National Laboratory [Munjiza (2004); Munjiza *et al.* (2015); Rougier *et al.* (2014)], the Y-Geo and Y-GUI software that have been developed by the Geomechanics Group led by Giovanni Grasselli at Toronto University [Mahabadi *et al.* (2010b, 2012)], and VGeST (Virtual Geoscience Simulation Tools) released by the Applied Modelling and Computation Group (AMCG) at Imperial College London [Xiang *et al.* (2009a); Munjiza *et al.* (2010)]. Recently the AMCG has upgraded and renamed VGeST as 'Solidity'. A commercial FEMDEM code developed by Geomechanica (www.geomechanica.com), has also been released in Canada, although its application has been limited to mod-

elling geomaterials. While the first Y-code employed finite strain elasticity coupled with a smeared crack model to capture deformation, rotation, contact interaction and fragmentation, the AMCG has greatly improved the code, implementing a range of constitutive models in 3D [Karantzoulis *et al.* (2013); Guo (2014)], thermal coupling [Joulin *et al.* (2017)], parallelisation and a faster contact detection algorithm [Xiang *et al.* (2017)]. The key features of the two-dimensional FEMDEM code that has been implemented in Solidity are the following ones: (a) compute the contact detection, interaction and motion of bodies, (b) calculate the stresses and deformations within bodies and (c) compute the transition from continua to discontinua when fragmentation occurs. The shape of two-dimensional bodies is discretised through a triangular mesh. Each triangle is both a discrete element (DE) and finite element (FE). The Y-code, which was presented in Munjiza (2004), has provided the fundamental theoretical aspects of the contact and cohesive crack model employed in Solidity and will be critically summarised in the following sections.

3.1.2.2 Contact detection and interaction

When two bodies are in contact, some of the elements of the mesh of the first body overlap some elements of the boundary of the second body, as shown in Figure 3.1(a). A contact detection algorithm detects all the couples of DE that are more likely to be in contact, discarding all the couples that are too far to be in contact. This is done to avoid processing the contact interaction of all the possible couple of elements in the system and therefore reducing the run time of the simulation. The contact interaction is implemented through a variational formulation. The penalty function method is used to compute the normal component of the contact force between two bodies by imposing the stationarity of a functional subject to the contact constraints over the boundaries. The contact potential function is defined in the form of equation (3.1), where p is the penalty term, while $f(\mathbf{x})$ is a function of the point \mathbf{x} in the

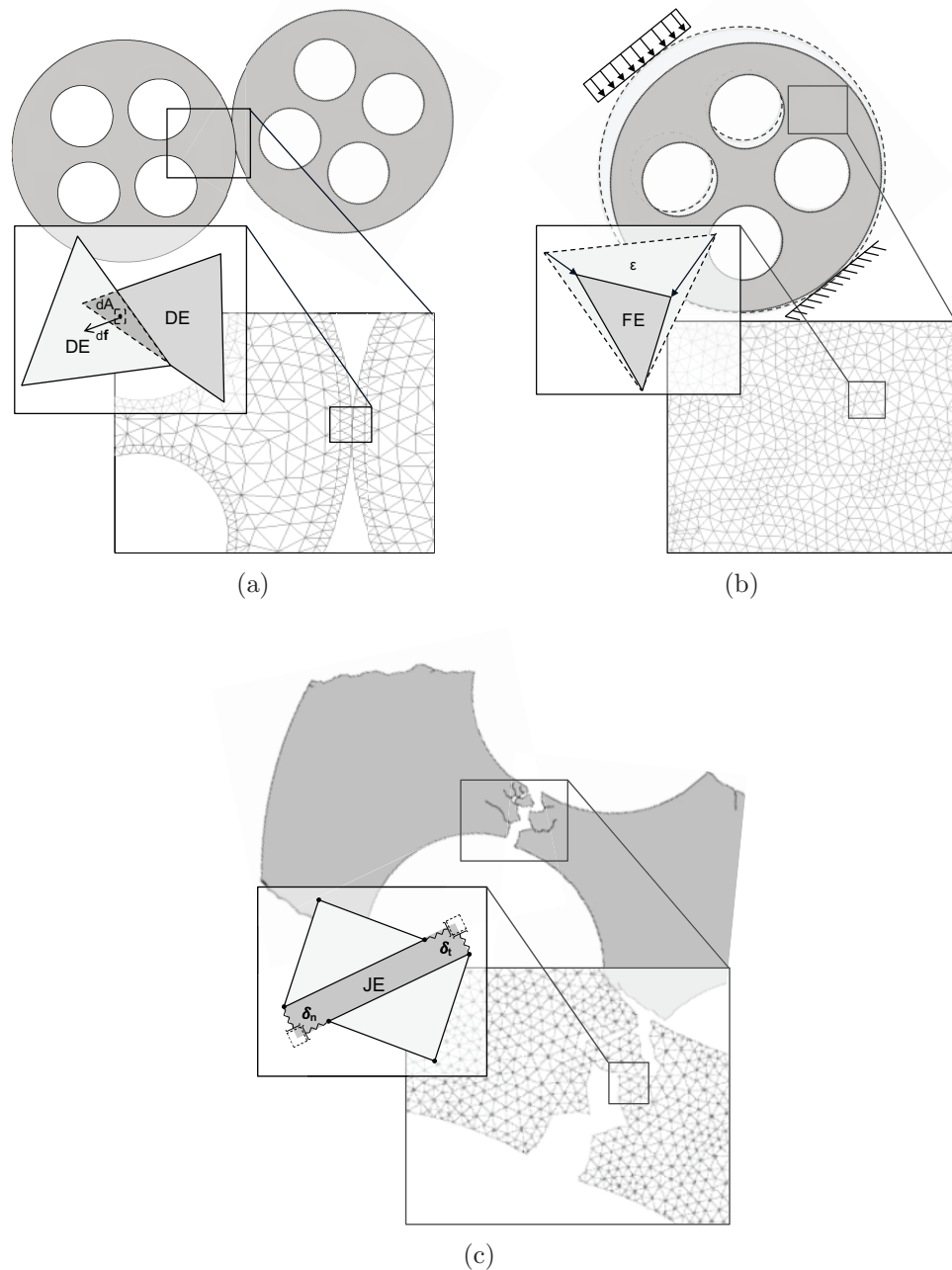


Figure 3.1: Scheme of the key features of the Solidity FEMDEM code: (a) compute the contact interaction and motion of bodies, (b) calculate the stresses and deformations and (c) compute the transition from continua to discontinua when fragmentation occurs.

overlapping discrete elements of the two contacting bodies. The function $f(\mathbf{x})$ is defined in such a way that it is zero outside the discrete element, constant on the boundaries and increasing while moving towards the centre of the discrete elements (triangles in 2D or tetrahedra in 3D). The infinitesimal contact force is defined as the gradient of the corresponding potential function $d\mathbf{F} = -\nabla(\varphi) dA$ in 2D and $d\mathbf{F} = -\nabla(\varphi) dV$ in 3D, where dA and dV are the infinitesimal overlapping area and volume. The total contact force can then be calculated by integrating the infinitesimal contact force field over the overlapping area (in 2D) or volume (in 3D). This ensures that the energy during the contact interaction is conserved, independently of the penalty term, element shape or magnitude of the penetration, as the so-defined contact force field is conservative [Munjiza & Andrews (2000)].

$$\varphi(\mathbf{x}) = p \cdot f(\mathbf{x}) \quad (3.1)$$

Since the solution obtained through the minimisation of the potential function satisfies the constraint of impenetrability only approximately, the contacting couples tend to penetrate into each other, generating distributed contact forces along their boundaries. With a sufficiently large penalty term the extent of the overlapping is negligible as is the related error in the response of the simulated system. The difference between the effects of two different but statically equivalent loads becomes very small at sufficiently large distances from load [de Saint-Venant (1856)], therefore the structural response of a body to contact forces can be well represented even though the mesh discretisation and penalty term might locally influence the correct distribution of the pressure on the contact surfaces of two colliding bodies.

3.1.2.3 Fracture initiation and propagation

The transition from a continuous domain to a discontinuous domain is carried out through fracture and fragmentation processes. The model implemented in the code is based on the assumption that the stress-strain curve consists of a hardening branch (before the peak) and a strain-softening part (where the stress decreases with the strain increasing), as illustrated in Figure 3.2.

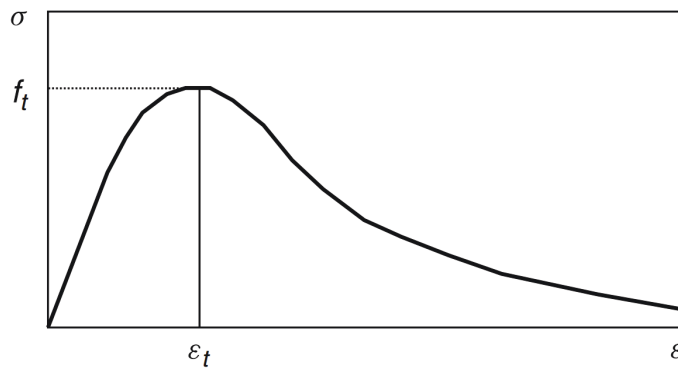


Figure 3.2: Objective stress-strain curve to be modelled [Munjiza (2004)].

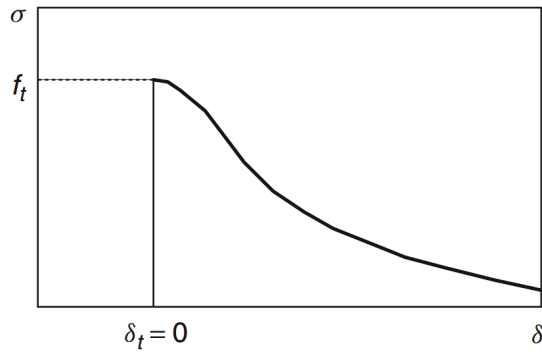


Figure 3.3: Strain softening defined in terms of displacements [Munjiza (2004)].

Figure 3.3 shows the strain-softening relation that has been implemented in the code through the constitutive law of the joint elements in terms of stress and displace-

ments. The strain-softening part is also defined in terms of stress and displacements in order to avoid the ill-posedness of the problem generated by a stress-strain definition. The area under the graph in Figure 3.3 is the energy release rate (G_f), i.e. the energy dissipated in order to extend the surface of the crack. G_f is also equal to twice the surface energy, which quantifies the disruption of intermolecular bonds that occur when a surface is created. The relationship between stresses and displacements is modelled through a single crack model: when the size of separation is zero the bonding stress is equal to the tensile strength (f_t), implying that the separation begins only after reaching this stress value equal to f_t . Once the separation starts to increase, there will be a decrease in bonding stress. When it reaches a limit value of separation (δ_c), the bonding stress tends to zero. In the actual implementation of this model, the separation of adjacent element edges is assumed in advance by introducing joint elements and describing the topology of adjacent elements with different nodes. As no two elements share any nodes the continuity between elements is enforced through the penalty function method. Before the bonding stress reaches the tensile strength its value is given by equation (3.2), where δ_p is the separation corresponding to when the bonding stress is equal to the tensile strength ($\delta_p = 2h f_t/p$), h is the size of that particular finite element and p is the penalty parameter.

$$\sigma = f_t \left[\frac{2\delta}{\delta_p} - \left(\frac{\delta}{\delta_p} \right)^2 \right] \quad (3.2)$$

After the bonding stress has reached the tensile strength, the strain-softening law described in terms of stress and displacements is given by the equation (3.3), where z is a heuristic scaling function representing an approximation of the experimental stress-displacement curves and the parameters a, b and c are obtained from the

interpolation of experimental stress displacement curves. These parameters only define the shape of the softening curve, which is then stretched depending on the material properties of the material (i.e. the energy release rate and the tensile strength). However, the heuristic curve that was implemented in the first Y-code was derived from direct tension experiments on concrete samples. There are other materials that have been tested to obtain a more representative softening curve shape, such as granite, e.g. see Rougier *et al.* (2014). The variable D is given by equation (3.4) and the complete relationship for the normal bonding stress as a function of separation can be written as shown in equation (3.5).

$$\sigma = f_t \left[1 - \frac{a+b-1}{a+b} e^{(D \frac{a+cb}{(a+b)(1-a-b)})} \right] [a(1-d) + b(1-D)^c] \quad (3.3)$$

$$D = \begin{cases} 0 & \delta \leq \delta_t \\ 1 & \delta > \delta_t \\ \frac{\delta - \delta_t}{\delta_c - \delta_t} & otherwise \end{cases} \quad (3.4)$$

$$\sigma = \begin{cases} f_t \left[\frac{2\delta}{\delta_p} - \left(\frac{\delta}{\delta_p} \right)^2 \right] & 0 \leq \delta \leq \delta_p \\ f_t \left[1 - \frac{a+b-1}{a+b} e^{(D \frac{a+cb}{(a+b)(1-a-b)})} \right] [a(1-d) + b(1-D)^c] & \delta > \delta_p \\ f_t \left[\frac{2\delta}{\delta_p} \right] & \delta < 0 \end{cases} \quad (3.5)$$

The implementation of the constitutive law given above can be represented as the interposition of normal and shear springs between the joint nodes of the elements

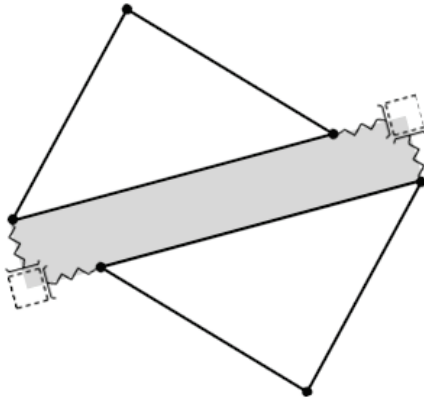


Figure 3.4: A schematic representation of the joint elements.

in contact, as shown in Figure 3.4. The normal springs have a non-linear stress displacement law given by equation (3.5), whereas the shear springs have analogous laws representing shear failures. The normal and shear springs between the joint nodes of the elements in contact are removed once the separation reaches the value δ_c , meaning that the fracture has propagated through the edge. With the bonding stress model as described above, the stress and strain fields close to the crack tip are influenced by the magnitude and distribution of the bonding stress close to the crack tip. In particular the stress field is influenced by the mesh topology close to the crack tip.

In order to have a good approximation of the crack propagation the element size close to the crack tip needs to be much smaller than the size of the plastic zone (Δ), represented in Figure 3.5. The length of the plastic zone proposed in Munjiza (2004) for a plane stress mode I loaded crack can be approximated by equation (3.6). In the next section a slightly different formulation based on Irwin's modification of Griffith's solids theory will be presented and the consequent constraints on the numerical discretization will be discussed.

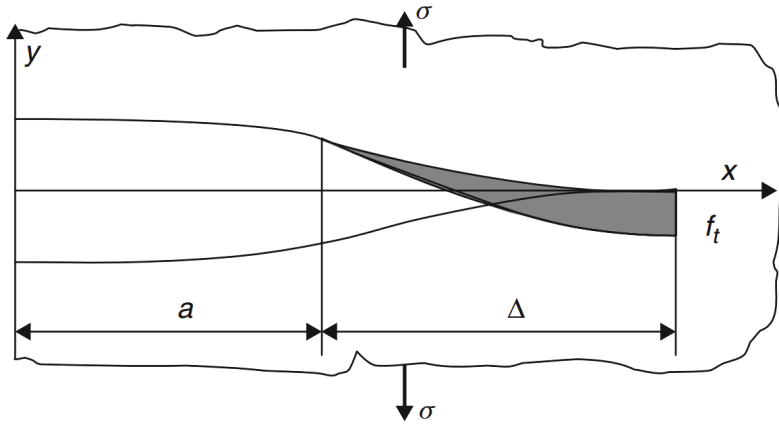


Figure 3.5: Single crack model with bonding stress [Munjiza (2004)].

$$r_p \text{ Munjiza} = \frac{\pi E \delta_c}{32 f_t} \quad (3.6)$$

3.1.2.4 Discretisation of the plastic zone

The toughness, or resistance to crack growth, of a material is governed by the energy absorbed as the crack moves forward. In extremely brittle materials such ceramics with low porosity, this energy is primarily just that of rupturing the chemical bonds along the crack plane. In tougher materials bond rupture plays a relatively small role in resisting crack growth, with by far the largest part of the fracture energy being associated with plastic flow near the crack tip. The elastic stress field near the crack tip is defined in Westergaard (1939) by the system of equations (3.7).

$$\begin{cases} \sigma_x = \frac{K_I}{\sqrt{2\pi r}} \cos \frac{\theta}{2} \left(1 - \sin \frac{\theta}{2} \sin \frac{3\theta}{2} \right) + \dots \\ \sigma_y = \frac{K_I}{\sqrt{2\pi r}} \cos \frac{\theta}{2} \left(1 + \sin \frac{\theta}{2} \sin \frac{3\theta}{2} \right) + \dots \\ \tau_{xy} = \frac{K_I}{\sqrt{2\pi r}} \cos \frac{\theta}{2} \sin \frac{\theta}{2} \cos \frac{3\theta}{2} + \dots \end{cases} \quad (3.7)$$

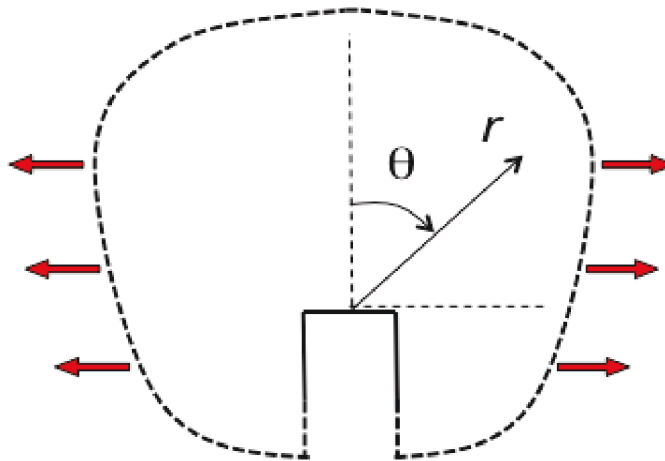


Figure 3.6: Schematic representation of the crack tip.

where r and θ are the polar coordinates on the crack plane, as shown in Figure 3.6, and K_I is the stress intensity factor. This parameter is defined as $K_I = \sqrt{E G_I}$, where E is the Young's modulus and G_I is the energy release rate, which has been defined in the previous section. For distances close to the crack tip, the second and higher order terms of the series that defines the stress at the crack tip can be neglected, as indicated by dots in equations (3.7). By simplifying these expressions, the elastic stress field along the fracture, at a distance r from the crack tip can be approximated by the following equation (3.8).

$$\sigma \approx \sqrt{\frac{E G_I}{2\pi r}} \quad (3.8)$$

As r tends towards zero, the crack tip stresses become singular. This implies that a yielded region will exist in the material ahead of the crack for all reasonable stress values. A plastic zone is present near the crack tip within which the stresses as predicted by the above equation would be above the materials yield stress f_t , as shown in Figure 3.7. The size of the plastic zone first presented in Irwin *et al.* (1958) is given by equation (3.9), and can be estimate by substituting the tensile

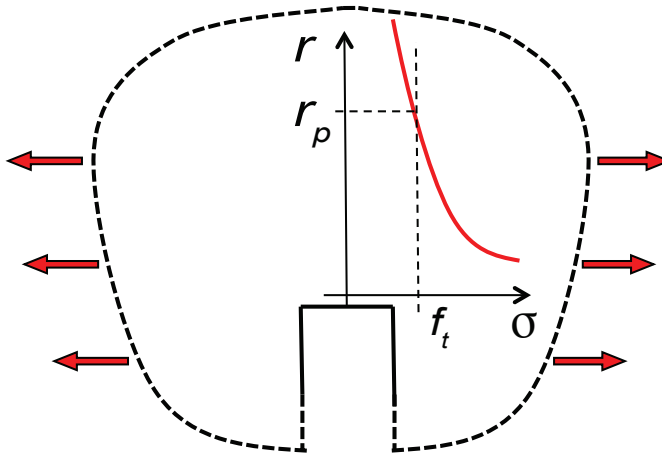


Figure 3.7: Representation of stress field near the crack tip.

strength into equation (3.8).

$$r_{p \text{ Irwin}} \approx \frac{E G_I}{2\pi f_t^2} \quad (3.9)$$

Approximate stress and strain fields close to the crack tip are obtained through a finite element discretisation of the governing equations. As described in the previous section, a cohesive law is implemented in the Solidity FEMDEM code to describe the fracturing process that takes place in the plastic zone. This law gives the relationship between bond stress and separation of two finite elements taking into account the equivalent plastic deformation (and energy consumption) before fracture occurs. With this bonding stress model, the stress and strain fields close to the crack tip are influenced by the magnitude and distribution of the bonding stress close to the crack tip. For this reason it is necessary that the size of finite elements close to the crack tip be smaller (at least one fourth to correctly numerically represent the bonding stress with constant strain triangles) than the actual size of the plastic zone, as illustrated in Figure 3.8. Finally, a relation between the maximum element size h_{max} adopted in the discretisation and the mechanical properties of the analysed structure can be

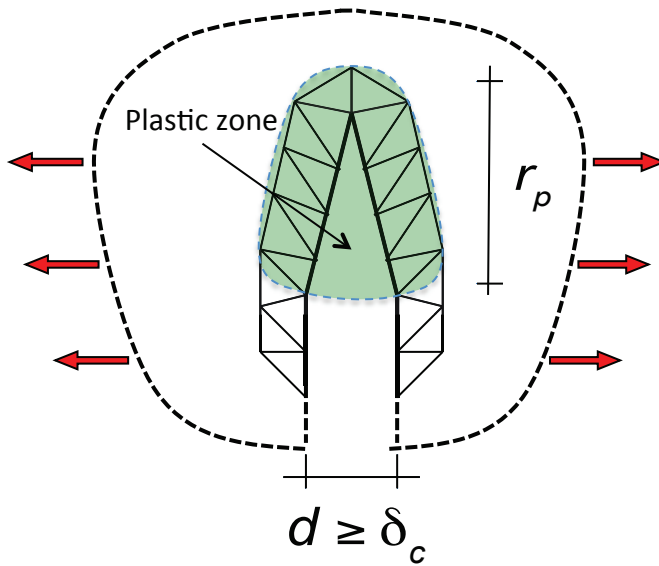


Figure 3.8: Schematic representation of discretisation near the crack tip.

defined in equation (3.10) in order to avoid numerical issues. This constraint on the mesh discretisation represents a strong limitation on the applicability of the method to simulate particular classes of problems and will be discussed in the next sections.

$$h_{max} \approx \frac{E G_I}{8\pi f_t^2} \quad (3.10)$$

3.1.2.5 Required parameters and their physical interpretation

In order to describe a physical system through numerical modelling a set of parameters needs to be determined. An estimate of the values of the parameters in Table 3.1 is needed for the Solidity FEMDEM code in order to simulate fragmentation. A concise theoretical explanation of the physical meaning of each parameter is now presented. The Mohr-Coulomb failure criterion shown in Figure 3.9 represents the linear envelope that is obtained from a plot of the shear strength of a material versus the applied normal stress when failure occurs. The τ axis represents the shear

strength and σ axis represents the normal stress; d is the intercept of the failure envelope with the τ axis, and ϕ is the slope of the failure envelope. The quantity d is called cohesion and the angle ϕ is called angle of internal friction. Compression is here assumed to be positive: in order to have a better description of brittle materials this failure criterion has been provided with a tension cut-off that limits the tensile stress to the value of f_t , which is called the tensile strength. Before reaching the failure envelope the stress-strain relationship is modelled as linearly elastic and it is governed by Young's modulus (E) and Poisson's ratio (ν). When failure occurs, the fracture opening is described in terms of stress-displacement by a heuristic curve governed by the energy release rate (G), i.e. the energy dissipated in order to extend the crack. Figure 3.10 shows the relation between the stresses and displacements of the simulated material until failure. Only when a fracture has opened up, are the two fracture walls considered to be two distinct surfaces of the domain. When two distinct surfaces are in contact, two different processes are defined in the Solidity FEMDEM code. A contact force is applied to two colliding surfaces in order to avoid their conpenetration: this force is implemented through a penalty function method and it is governed by a penalty number (p), which can be assumed to be correlated to the Young's modulus (E). Friction is applied when surfaces slide over each other and its value is implemented with a Coulomb model of friction through a friction coefficient (μ), which change with the materials of the two surfaces (a and b) in contact as shown in Figure 3.11. Since in a real system some stress waves are dissipated in sound, thermal energy or they simply leave the domain, if dissipations are not taken into account, the reflections and superposition of these strain waves may cause unrealistic brittle failure in the structure. To avoid these dynamic effects, a viscous damping proportional to stiffness is applied to finite elements as an energy dissipation mechanism, where viscous forces are calculated using the rate of deformation tensor. As shown in Munjiza (2004), a critical value of viscous damping

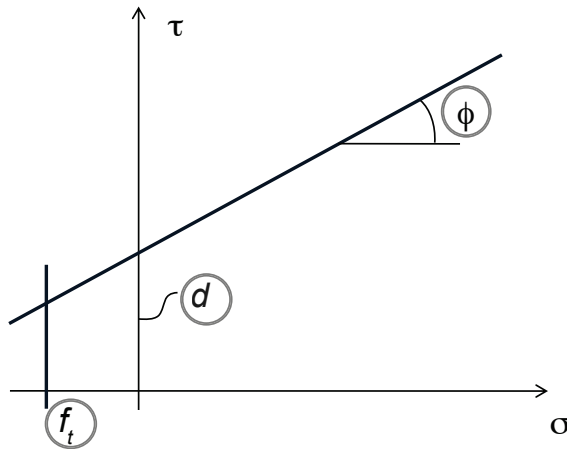


Figure 3.9: Mohr-Coulomb failure criterion with a tension cut-off.

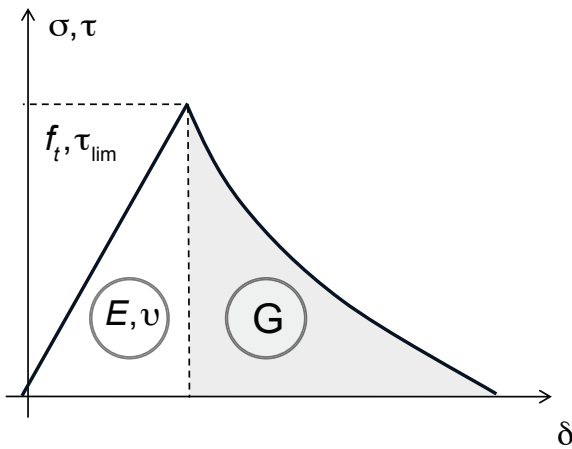


Figure 3.10: Strain softening defined in terms of displacements.

(η) can be correlated, to Young's modulus (E), density (δ) and the element size (h), which is a numerical parameter.

3.1.3 Bonded-DEM vs FEMDEM fracture codes

DEM is a powerful method for computing, with a reasonably small run time, the motion and interactions of a large number of particles. There are several approaches presented in the literature aimed at describing solid fragmentation using DEM. In Huang *et al.* (1999) numerical simulations of uniaxial compression and cutting

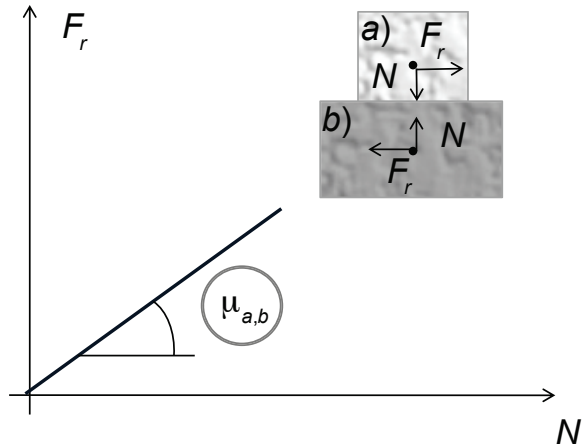


Figure 3.11: Relation between normal and friction force with a Coulomb model of friction.

Table 3.1: Required parameters for simulating fragmentation with FEMDEM.

Name	Symbol	Unit
Cohesion	d	[Pa]
Angle of internal friction	ϕ	[rad]
Tensile strength	f_t	[Pa]
Young's modulus	E	[Pa]
Poisson's ratio	ν	
Energy release rate	G	[J/m ²]
Penalty number	p	[N/m]
Friction coefficient	μ	
Density	δ	[kg/m ³]
Viscous damping coefficient	η	[kg/s]

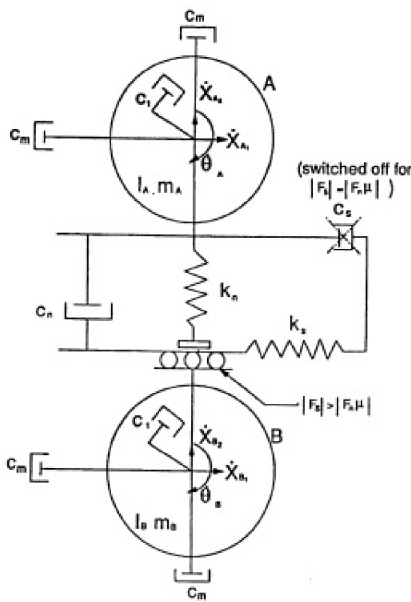


Figure 3.12: Example of rheological elements of DEM for the interaction between particles [Sitharam (2000)].

processes of rock have been presented employing packed discrete elements bonded together to represent the bulk rock material. Similar examples are presented to describe tunnelling, flexural and Brazilian tests in Potyondy & Cundall (2004), and powder agglomerates in Liu *et al.* (2010). The standard approach consists of defining a packed structure of particles (generally spheres) with a determined particle size distribution and then defining laws for the contact and interactions between particles (Figure 3.12) on the basis of parameters such as penalty numbers, stiffness of the bonding, etc. and to obtain forces that, once they are applied to the elements, define the movement of the simulated bodies with Newton's laws of motion.

The material properties are therefore uniquely implemented by means of numerical parameters representing the rheological elements affecting the interaction between particles, and they are moreover affected by the choice of the packed structure employed for idealizing the bulk material. Those parameters have not direct correspondence with the mechanical properties at the macroscale, properties that are generally inferred from standard experiments. For instance one of the parameters

that is generally accepted to describe the elastic deformation phase of materials is the Young's modulus, and it can be easily inferred from the comparison between standard experiments and the analytical solution of the corresponding linear elastic homogeneous model or eventually by consolidated empirical correlations. In a DEM model the equivalent of Young's modulus is a combination of numerical parameters, such as penalty numbers and/or stiffnesses of fictitious springs between particles, and these parameters regulate the forces needed for overlapping and separating two elements. This means that the mechanical description of a DEM model is defined in terms of forces and displacements, assuming rigid particles with contact laws and therefore stresses and strains could be only inferred at a second stage. Consequently it is not easy to characterise a material in a DEM model: on one hand the relationship between these numerical parameters and the conventionally employed mechanical properties is not straight forward, given that these are in terms of forces and displacements and the others are in term of stresses and strains (e.g. one of the parameters that define the relationship between the tensor of the stresses and the tensor of strains is the Young's modulus itself). On the other hand there are no analytical solutions to correlate standard experiments to those numerical parameters and therefore the calibration of a DEM model could be performed only on the basis of numerical correlations and optimizations (such as by inverse analyses). These considerations reveal how combining the finite element method with the DEM can bring considerable advantages: with FEMDEM the mechanics of bodies is defined in terms of stresses and strains, allowing the implementation of generally accepted and consolidated constitutive models that describe the behaviour of different materials (such as glass, concrete, plastics, etc.) and, as a consequence, it is possible to calibrate FEMDEM models with fundamental material parameters that are well characterized in literature. Therefore it is possible to simulate the interaction of large number of particles with great accuracy, revealing stress waves inside bodies

and other features that are not easily exhibited with an uncoupled DEM code. The cost of these features is an additional run time during the calculation. In fact both DEM and FEMDEM are explicit methods that need to reiterate the calculations for all the time steps of the time discretization, but while a single iteration of a DEM code is relatively fast, in a FEMDEM code an additional run time is needed, as more complex calculations are required and moreover a finer time discretization is often necessary. For this reason, with the current CPU performance and grade of sophistication of the algorithm, the domain of applicability of FEMDEM codes, in general, do not include all the possible engineering applications, in particular when a large number of deformable particles, e.g. ones that are also breakable in response to developing stress regimes, needs to be computed (this will be discussed in detail in following Sections). For those applications DEM, or other more efficient methods, represent the only alternative to compute the results in a reasonable run time.

3.2 Simulating multi-body systems

3.2.1 Introduction

The study of the dynamic behaviour of a system with a large number of interconnected bodies, generally called granular media, is an important field in mechanics. Granular materials not only are already present in nature, where grains cover about 90% of the solid surface of the planet, with sizes varying from micrometres (clay) to more than 100 meters (rock blocks); but they are also the matter of study of food, powders and chemical processing and mixing technology, etc. Even though granular materials are used in a variety of fields, the explanation of some trivial behaviour observed in granular systems is not completely clear and is still an open field of study for physicists and engineers. The type of interactions between grains is

wide: factors such as chemical reactions, presence of fluid or particle fragmentation influence their behaviour. In addition to the diversity of materials involved, the granular world also covers a wide range of physical processes: a granular medium can either behave as a gas, a solid or a fluid forming liquid bridges depending on the degree of agitation (related to the granular temperature) of the grains. The granular system is classified as dry granular material when its behaviour is not influenced by the interstitial fluid and cohesive forces between the grains. This class of granular systems has now gained widespread attention due to abundance of the applications associated with it [Guises (2008)].

One of the main topics of interest that is strictly related to the behaviour of a granular system is the study of the packing of particles. This is an extensive field of research with interest covering many different fundamental and applied topics: from the description of fluids and glasses [Berryman (1983); O'Hern *et al.* (2001); Majmudar *et al.* (2007)], to the characterization of the rheology of granular flow [Campbell (1990); Goldhirsch (2003); Forterre & Pouliquen (2008)], or the description of transport properties of rocks. Another important field of application is the description of the packing structure and the force transmission through a grain assembly [Majmudar & Behringer (2005); Mueggenburg *et al.* (2002); Da Silva M & Rajchenbach (2000)]. In all of these applications, computational tools and numerical simulations have become essential as effort is focussed on the understanding of complex processes involving a large numbers of particles. Packing algorithms for non-spherical particles that have superseded the popular type of frozen-once-placed ballistic deposition algorithm once appropriate for spheres (Aparicio and Cocks 1995) or sphere composites, can be broadly divided as follows:

- Purely geometric types include random space filling and collective rearrangement [e.g. Caulkin *et al.* (2008)];

- DEM based on extensions from the original spherical-based approach with geometrically determinate radial contact normals, e.g ellipsoids and superquadrics [e.g. Song *et al.* (2006)];
- DEM based on clustered overlapping variable size spheres [e.g. Caulkin *et al.* (2015)];
- Polyhedral DEM where contact forces can be calculated between arbitrary shaped convex and concave polyhedra with overlapping volume or common plane area repulsive force formulations [e.g. Mack *et al.* (2011)];
- Combined FEMDEM approaches where to create arbitrary complex and convex particles, shapes are constructed from combinations of primitive concave polyhedra that can be rigid or deformable [e.g. Munjiza (2004)].

3.2.2 FEMDEM method for multi-body systems

A challenge for the FEMDEM methods, especially transient dynamic deformable simulations that track the stress waves inside the grains, is that the methods are relatively more expensive in terms of computational time, which limits the number of particles that can be considered or process time that can be modelled. Where the particles are known to have both smoothly curved and flat faces while also having sharp edges, such as cylinders, the number of tetrahedral elements to represent this particle geometry accurately may seem prohibitive. For this reason, in many applications dealing with multi-body systems, DEM capability is justifiably focusing on the dynamic solid particulate flow properties of systems in which millions of particles are involved and where the time of relevance is many seconds or even minutes of real time. Simplifying assumptions are made to achieve run completion in practical timescales.

However, there are certain applications, typically in manufactured particles, where a representative pack is of the order of a thousand particles. More accurate capturing of the influence of complex shape is often necessary to model the topology of the void space e.g. for optimisation of fluid flow properties. Alternatively it may be the force or stress transmission through the contact points that is critical to avoid functional damage, or both structural stability and flow properties are the simulation purpose. In the context of mono-sized, mono-shape packing problem, for applications where special shapes are needed for engineered granular packs, the FEMDEM technology would appear to be ideally suited. The field of applicability of the Solidity FEDEM code is discussed in the next section.

3.3 Applicability of DEM and FEMDEM simulations to industrial problems

3.3.1 Introduction

The verification of simulation results is normally the first step to confirm the applicability of a computational tool to describe a certain industrial problem that needs to be investigated. Model validation is defined in Schlesinger (1979) as the 'substantiation that a computerised model within its domain of applicability possesses a satisfactory range of accuracy consistent with the intended application of the model'. A model should be developed for a specific application and its validity determined with respect to that purpose. If the application of a model is to answer a variety of questions, the validity of the model needs to be determined with respect to each question. Numerous sets of experimental conditions are usually required to define the domain of a model's intended applicability. A model may be valid for one

set of experimental conditions and invalid in another. A model is considered valid for a set of experimental conditions if the model's accuracy is within its acceptable range, which is the amount of accuracy required for the model's intended purpose. This usually requires that the model's output variables of interest (i.e., the model variables used in answering the questions that the model is being developed to answer) are identified and that their required amount of accuracy be specified. The behaviour data of the simulation model and the system can be graphed for various sets of experimental conditions to determine if the model's output behaviour has sufficient accuracy for the model's intended purpose. These comparisons can be used in different ways: graphs can be used in the model development process to make a subjective judgment on whether a simulation model possess sufficient accuracy for its intended purpose. In order to determine how accurate is the level of prediction of the model, a procedure with statistical techniques and a strategy of data collection must be defined for each set of experimental conditions and for each variable of interest [Sargent (2005)].

The mathematical representations of the contact physics between particles and container walls including friction effects have been implemented with varying sophistication by the DEM community and to determine the range of applicability of those models a verification study is consequently crucial. For this reason we can observe a considerable effort in validation studies of DEM numerical simulations in literature. The comparison between packed structures of different shaped pellets and their equivalent numerical simulation has been presented in Caulkin *et al.* (2008), where bulk density, local packing density profiles, and pellet orientation distributions obtained from computational models have been compared with the experimental data sets obtained from X-ray computerized tomography of the packed columns. In Li *et al.* (2005) a validation study has been proposed: they performed experiments to complete the determination of all material properties including friction coeffi-

cients applicable to glass and steel sphere simulations so that sandpile experiments with spherical particles could be numerically simulated with DEM. In Cleary *et al.* (2003) the dynamics of granular systems in flow, flow rates through apertures, velocity field statistics, have been compared with DEM numerical simulations. In Asmar *et al.* (2002) it is shown a different methodology for validation studies: some simple simulations are used to verify code: in fact they do not compare their results with that of experiments, but they set up eight mathematical tests based on artificial situations that can uncover bugs in programs, even if they appear to simulate real experiments reasonably well. In Zhou *et al.* (1999) has been investigated the mathematical importance of rolling friction on the formation of a heap of spheres. The discrete element method has been also coupled with other theories in order to capture more complex phenomena: in Takeuchi *et al.* (2012) and Takeuchi *et al.* (2013) a combines discrete phase and fluid dynamic model has been compared to actual experiments of particle breakage in an impact pulveriser. Combined finite-discrete element method (FEMDEM) codes have also been subjected to validation studies: in Latham & Munjiza (2004) and Xiang *et al.* (2009b) respectively a cube-packing experiments and free balls on a rotating disc have been compared to their equivalent numerical simulations to investigate the capability of the code to represent contact between particles and container walls in packed structures. Mahabadi *et al.* (2010a), Rougier *et al.* (2011) and Knight *et al.* (2013) have presented validation studies on the capability of FEMDEM in the description of solids fragmentation, comparing the behaviour of Brazilian disc specimens as observed in laboratory during dynamic indirect tensile tests to their equivalent numerical simulations.

3.3.2 Domain of applicability of the Solidity FEMDEM code

It is important to highlight the limitations of the current Solidity FEMDEM code in order to understand the domain of applicability. The code has an explicit solver, in other words it discretises the continuous time in time steps and then it calculates the state of a system at a later time step on the basis of the state of the system at the current time step. This implies that, even if only the status of the system at an exact time is required, the code needs to calculate the output for every prior time step until it reaches the required one. To give an example: if you want to calculate the state of a modelled system after three seconds from the initial conditions, the total run time is equal to the run time of a single iteration multiplied by the number of time steps before the required one, in this case three seconds divided by the length of the time step. So, by fixing the real time of the system that needs to be simulated, the total run time is directly proportional to the run time of a single iteration and inversely proportional to the length of the time steps. It is important to bear in mind that the run time of a single iteration increases with the number of elements of the numerical discretization and decreases with the rise of the CPU performance of the computer employed for the calculation. On one hand the length of the time step decreases with the dimension of the elements and on the other hand to enforce accuracy there are numerical limitations that force the use of a large number of small elements. This brings a limitation on the domain of applicability of the Solidity FEMDEM code: when simulating a large number of particles, each individual particle needs to be discretised with several elements. That means that the number and dimension of the elements is practically constraining the maximum real time and in turn the physical process that can be simulated in a reasonable time.

Moreover, when simulating fracturing, a relation between the maximum element size

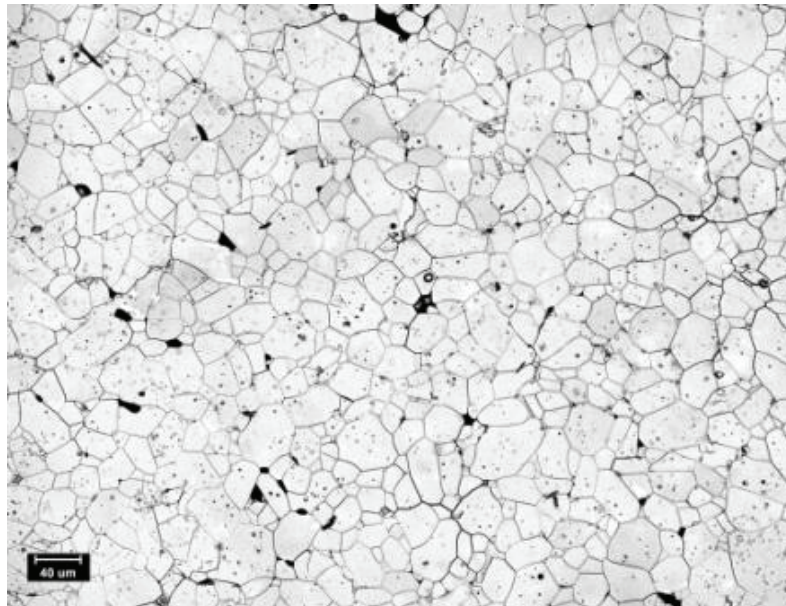


Figure 3.13: Representation of an alumina specimen microstructure.

adopted in the discretization and the mechanical properties of the analysed structure is defined in equations (3.10) and (3.6). This constraint needs to be satisfied in order to avoid numerical issues, as discussed in the previous sections. Some estimates of E (Young's modulus), G (energy release rate) and f_t (tensile strength) are obtained with the correlations presented in Lam *et al.* (1994) for a standard engineering ceramic and the derived maximum element size is reported in Table 3.2. From the table it is clear how this constraint on the numerical discretization affects the run time of the simulation. One last important observation is that the maximum element size could sometime be comparable to the dimension of the grains that constitute the microstructure of the ceramic ($5\text{--}40 \mu\text{m}$), as shown in Figure 3.13.

Table 3.2: Material properties of partially dense alumina samples [Lam *et al.* (1994)] and their numerical discretisation constraints.

Firing temperature [°C]	E [GPa]	Density [kg/m ³]	G [J/m ²]	f _t [MPa]	r _p Irwin [μm]	r _p Munjiza [μm]	h _{max} [μm]
1200	73	2560	7	45	42.1	52.0	13.0
1300	136	2840	14	97	31.8	39.2	9.8
1400	355	3800	36	165	4.5	5.6	1.4

Chapter
FOUR

Mechanical characterisation

4.1 Introduction

The purpose of the experimental work reported in this chapter is to determine the appropriate strength and stiffness parameters for the specific porous ceramic materials which are to be the subject of a detailed fracture and multi-body packing study using numerical simulation with the Solidity FEMDEM code. The combination of high strength, high porosity and necessarily small specimens required that a considerable effort would need to be expended to produce a reliable set of experimental data for assigning material properties. Such a set of properties could then inform the verification process that could ultimately demonstrate convincingly the applicability of the Solidity code for the simulation of high-performance catalyst supports. It is worth recalling that the FEMDEM methods to be used here have not been applied before to materials outside typical brittle geomaterials. As has

been introduced in Section 2.1 the investigation of microstructural properties and the accurate characterization of mechanical properties of porous ceramic samples is a critical issue in material science and has been tackled in this work by employing different testing techniques, including uniaxial compression (creating indirect tension in disc specimens), ultrasonic test, nanoindentations, mercury (Hg) intrusion, Brunauer-Emmett-Teller (BET) adsorption and three-point bending test.

4.2 Sample preparation

The samples were prepared with the help of Daniel Curry (Johnson Matthey). Three sets of prismatic samples were sintered with a reference alpha-alumina powder with an average granulate size in the 170-210 μm range that was compacted at an initial bulk density of 2.25 g/cm³ and then fired at 1200 °C, 1300 °C and 1400 °C to obtain three sets of bars with final bulk porosity of 0.36, 0.26 and 0.15 respectively. The geometry and density of the tested samples are reported in Table 4.1. Three sets of cylindrical samples with three different geometries were also sintered with the same reference alpha-alumina powder that was compacted at an initial bulk density of 2.25 g/cm³. Two sets consist of cylinders with two different sizes (*Small* and *Big*) and one set consists of cylinders with four holes (*4-hole*). The green pellets are then fired at 1200 °C, 1300 °C and 1400 °C to obtain three sets of three group of samples each. The average of the diameter of the cylinders (D), diameter of the holes (d), widths (t) and bulk densities of the tested samples are reported in Table 4.2.



(a)



(b)



(c)

Figure 4.1: (a) Reference alumina powder and (b) compaction die that have been used to produce the four-hole cylinders. (c) Some of the samples that have been tested.

Table 4.1: Average of the measured dimensions and bulk density of the tested prismatic specimens.

Set	L [mm]	H [mm]	Bulk density [g/cm ³]
1	40.20 ± 0.01	4.84 ± 0.01	2.58 ± 2%
2	38.09 ± 0.01	4.64 ± 0.01	3.00 ± 2%
3	36.33 ± 0.01	4.41 ± 0.01	3.25 ± 2%

Table 4.2: Average of the measured dimensions and bulk density of the tested specimens.

Set	D [mm]	d [mm]	t [mm]	Bulk density [g/cm ³]
1	Small	9.59 ± 0.01	-	8.88 ± 0.01
	Big	18.56 ± 0.01	-	19.16 ± 0.01
	4-hole	18.39 ± 0.01	5.14 ± 0.01	12.54 ± 0.01
2	Small	9.19 ± 0.01	-	8.49 ± 0.01
	Big	17.69 ± 0.01	-	18.36 ± 0.01
	4-hole	17.56 ± 0.01	4.88 ± 0.01	12.00 ± 0.01
3	Small	8.76 ± 0.01	-	8.09 ± 0.01
	Big	16.82 ± 0.01	-	17.53 ± 0.01
	4-hole	16.78 ± 0.01	4.68 ± 0.01	11.38 ± 0.01

4.3 Uniaxial compression

4.3.1 Brazilian discs

Brazilian disc tests were performed on the alumina cylinders. The test consists of placing a cylindrical pellet between two plates and diametrically compressing it to failure. A monolithic cylinder of aluminium alloy was placed centrally on the stationary base of the test rig (Instron model 5984 electromechanical test frame). An opposing cylindrical loading platen was mounted centrally on the vertically-moving crosshead of the test rig, below the load-cell. The experiments were performed in displacement control. The test rig control software (Instron Bluehill 3) recorded load and displacement during each experiment, at 0.1 second intervals. The compression applied on the sample by the loading plates induces a stress field with horizontal tensile stress which according to a linear elastic model has its highest value in the centre of the disc. The tensile strength can be calculated based on the two-dimensional elastic solution for a disc with two concentrated forces applied to its vertical extremes. It is then possible to express the horizontal tensile stress experienced by the specimen in the centre of the disc as a function of the applied load (F) and of the geometry of the sample.

$$f_t = \frac{2F}{\pi D t} \quad (4.1)$$

As shown in Figure 4.2 that failure occurs at the point of maximum tensile stress, i.e. at the centre of the disc, the Brazilian disc test formula (4.1) gives an estimate of the indirect tensile strength (f_t), where D is the diameter of the disc and t its

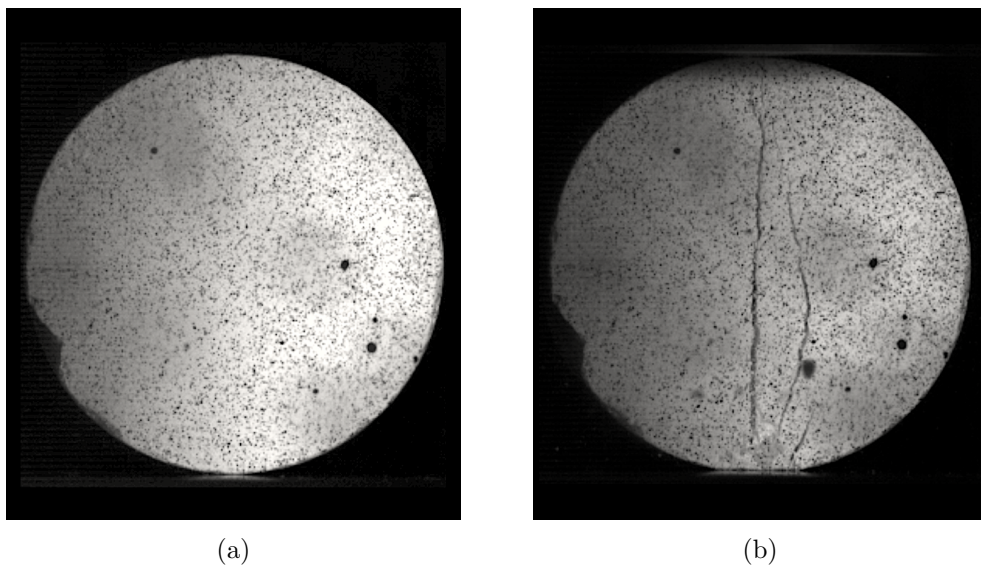


Figure 4.2: Two frames from the video recording of the uniaxial compression test on a cylinder without holes from Set 1: (a) before and (b) after failure.

width, International Society for Rock Mechanics (1978). This relation is only valid for cylinders without holes.

Since the Brazilian disc formula is not valid for specimens with holes, sets of discs of two different sizes (*Small* and *Large*) were produced with same compaction pressures and firing temperatures of the corresponding pellets with four holes. Two disc sizes were taken into account to represent the possible strength variation due to the employment of a different compaction die to cast the cylindrical pellets with four holes. The values of indirect tensile strength were then calculated for 4-6 samples for each set of discs with uniaxial compressions and the results have been reported in Figure 4.3. The strengths of the three sets of cylindrical pellets with four holes were then assumed to be equal to the average strengths of the corresponding sets of discs.

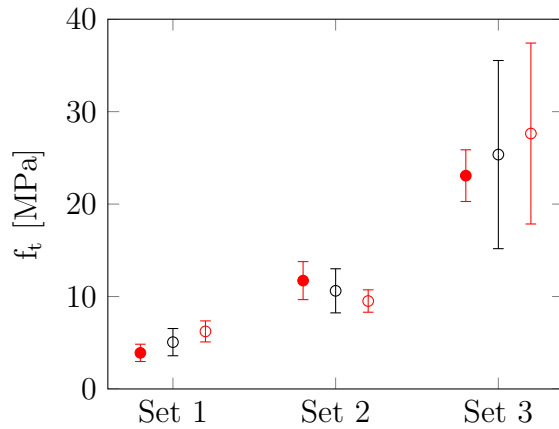


Figure 4.3: Indirect tensile strength of the *Small* (solid red) and *Big* (void red) cylinders evaluated by Brazilian disc test. Average (black) tensile strength obtained for the three sets of samples.

4.3.2 Four-hole cylinders

The four-hole specimens will later be used to illustrate the power of the FEMDEM code to capture the effects of complex geometry and the effect this has on the stress field and susceptibility to fracture in different modes and generate fragments. Uniaxial compressive tests were performed on 8-10 specimens from each of the three sets of four-hole cylinders. Prior to testing, one side-face of each specimen had a random speckle pattern applied. The experiments were performed in displacement control, with a crosshead velocity of 10 mm/s. For each set, the four-hole cylinders were tested in both the weak and the strong orientation of the holes, as shown in Figure 4.4(a) and 4.4(b) respectively.

The experiments were recorded with a high-speed video-camera (Vision Research Phantom v12.1 monochrome, maximum capture rate 16,000 frames/second at full-resolution of 1280 by 800 pixels, fitted with a 100 mm macro lens). The optical axis was set normal to the speckled side-face of the specimen. A high-speed video camera was used to capture the post failure behaviour and fragmentation of the samples at end of the test.

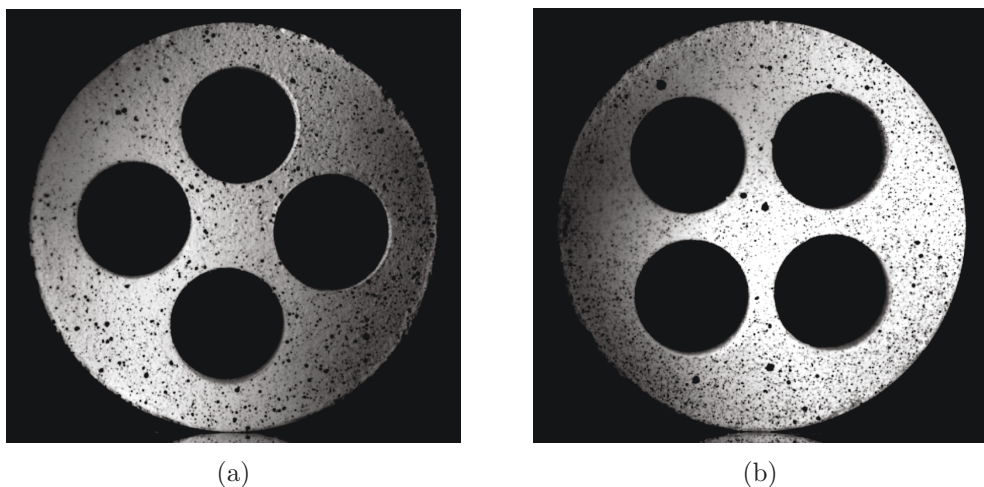
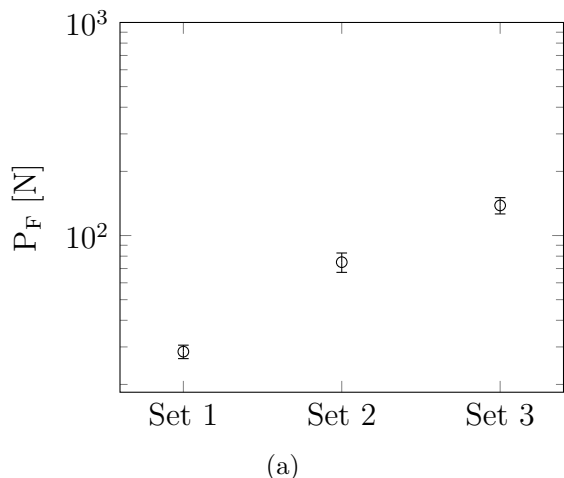
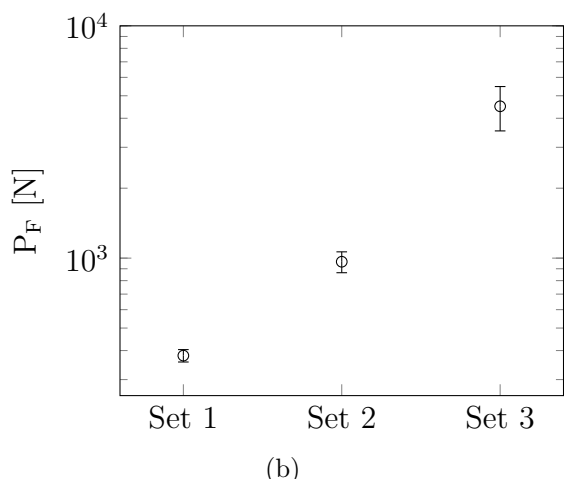


Figure 4.4: Frames from the video recording of the uniaxial compressive tests on four-hole specimens. (a) Weak and (b) strong loading orientation.

The experimental results can be used to quantify the structural strength given a defined configuration of the load, of this type of pellets for two loading configurations (weak and the strong orientation of the holes), i.e. the maximum value of force that the specimen can support without breaking for a given configuration (orientation) of the load. Limitations in the experimental apparatus have not allowed to obtain sufficiently accurate results for the strongest set of pellets (Set 3). The results from the other two sets of samples have shown a quite consistent relation between loading orientation, tensile strength and the structural strength of the pellets. When normalising the load at failure with the failure load of an equivalent cylinder of identical tensile strength and geometry but without holes, all the results converged to a value of about 2% for the weak orientation and about 20% for the strong orientation. It is important to point out that the load values at failure could have been affected by errors as the examination of the video recordings of the tests was required to define the time when the first fracture was visible on the samples, which might have occurred later than when that fracture was actually initiated.



(a)



(b)

Figure 4.5: Loads at failure for the uniaxial compressive tests on the four-hole specimens from the three set of samples. Results for the (a) weak and (b) strong loading orientation.

4.4 Ultrasonic test

The ultrasonic equipment consisted of a 25 MHz piezoelectric transducer, which emits and receives longitudinal waves through a bar sample immersed in a water bath, an amplifier and computer that records and processes the signals. Each tested specimen, after being coated with an impermeable thin layer, was placed on a thin metal support that separates the specimen bar from the bottom wall of the water tank and maintains the sample vertical and parallel with the transducer beam. A partially motored apparatus is then employed to align the ultrasonic beam with the longer dimension of the sample bar. This was done to maximise the length that the waves have to travel before and after being reflected by the bottom surface of the sample so that the recorded signals have two distinctive peaks that represent the top and bottom reflections.

Three specimen from each set of bars were tested with ultrasonics. Figure 4.6 shows a scheme with the path of the first reflected wave (yellow) and two possible paths of the transmitted wave (red and green dashed lines). When the transducer is not aligned with the beam the transmitted wave will follow a longer path (red dashed lines). The procedure followed to align the piezoelectric transducer with the tested samples consisted in tilting the transducer beam until the transmitted wave path was as shorter as possible, in other words when the time interval between the reflected and transmitted wave peak was minimised. Figure 4.7 shows the two distinctive sets of peaks recorded for one of the tests recorded for Set1. Since the path between the transducer and the top surface of the sample is travelled twice both by the top and bottom reflected waves, the distance between the two peaks corresponds only to the time that the waves take to travel twice the length of the specimen. Therefore, the velocity of the longitudinal waves propagating through the sample can be expressed as $V_L = \frac{2L}{\Delta t}$. The relation between density (ρ), Lamé constants (λ and

μ) of the specimen and the longitudinal wave velocity is $V_L = \sqrt{\frac{\lambda+2\mu}{\rho}}$ Timoshenko (1970). By substituting in the previous equation of the wave velocity the relations between the Lamé constants and Young's modulus ($E = \frac{\mu(3\lambda+2\mu)}{\lambda+\mu}$), Poisson's ratio ($\nu = \frac{\lambda}{2(\lambda+\mu)}$), it is possible to express the Young's modulus of the tested specimen as a function of the longitudinal wave velocity, Poisson's ratio and bulk density: $E = V_L^2 \rho \frac{(1-2\nu)(1+\nu)}{1-\nu}$. Since the test apparatus did not allow to transmit transverse wave through the specimen, the Poisson's ratio could not be experimentally estimated. Previous publications on ultrasonic tests on porous alumina samples report a value of 0.17 for the Poisson's ratio, assuming that it is 'approximately independent' of porosity Lam *et al.* (1994); Green *et al.* (1988). In more recent publications Asmani *et al.* (2001); Chang *et al.* (2000) the relation between Poisson's ratio and porosity of alumina samples has been experimentally investigated, showing that samples with similar porosity to the ones employed in the present work have Poisson's ratio in the 0.17-0.20 range. The Poisson's ratio was therefore assumed to be 0.17 as its variability affects the estimated Young's moduli by less than 3%. The experimental and signal processing tools for these ultrasonic tests were provided by Jack Egerton (Imperial College London).

4.5 Nanoindentations

Nanoindentation test results have been provided by James Bowen (Open University). The nanoindentation apparatus has maximum load of 400 mN, load noise of $< 1 \mu\text{N}$, maximum depth of 1,000 nm, and depth noise of $< 0.2 \text{ nm}$. A Berkovich diamond indenter with tip radius of $< 3 \text{ nm}$ has been used to indent the specimen. Each indentation test is performed within 240 s, including a 30 s holding time at the peak load. The testing temperature is maintained within the range of 20-22 °C to reduce thermal drift. The elastic moduli were measured using the Oliver-Pharr method

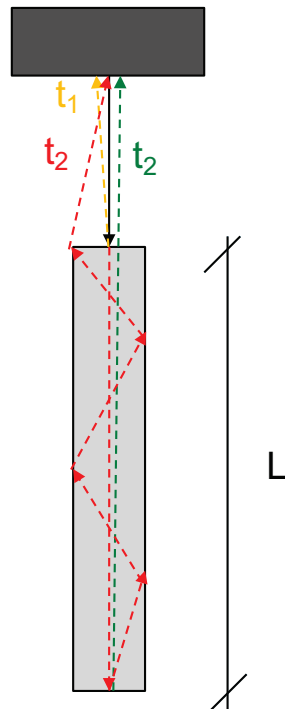


Figure 4.6: Scheme with the path of the first reflected wave (yellow) and two possible paths of the transmitted wave (red and green dashed lines).

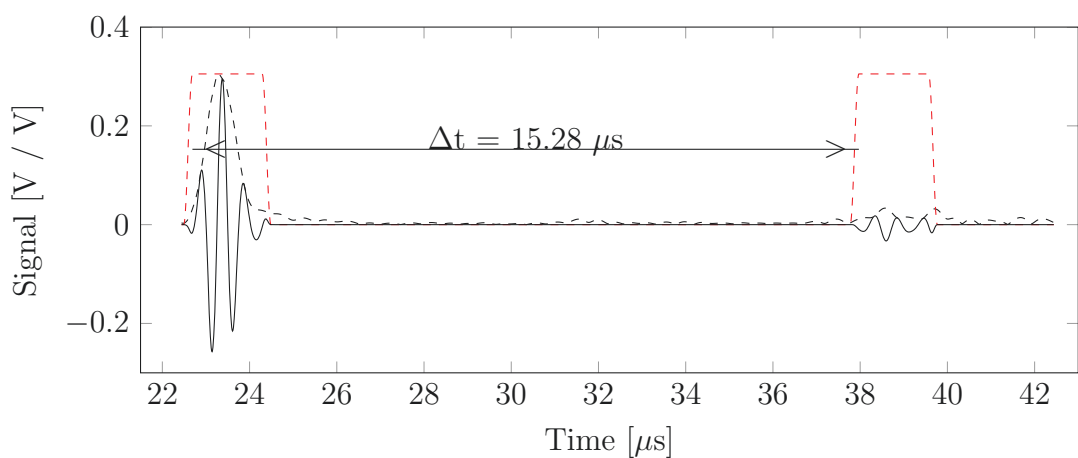


Figure 4.7: Experimental data of the sound rebound time obtained from an ultrasonic test on a sample from Set 1. In particular, the Hilbert envelope (dashed black), the filter windows (dashed red) and the windowed signal (continuous black).

[Oliver & Pharr (1992)].

One specimen from each set of bars was tested with nanoindentations. For each bar, one hundred indentations have been performed for statistical correction to minimize the experimental error. The histograms and normal probability distributions of the Young's modulus were estimated with one hundred nanoindentations on the surface of a sample. A correction was performed by excluding the experimental results that were 50% either lower or higher than the average value of the entire distribution. This correction was done to exclude the indentations that were not representative of the whole sample (e.g. direct indentations of pores or a crystals). The results from the indentations on a sample from Set 1 are shown in Figure 4.8.

Similarly, the Young's moduli of the four-hole cylindrical samples were also inferred by nanoindentations. The mean values and standard errors of the Young's modulus estimated for each set of samples are shown in Figure 4.9.

4.6 Hg intrusion and BET adsorption

Hg intrusion and BET adsorption test results have been provided by Michele Marigo (Johnson Matthey). One sample from each set of bars was analysed using a MicroActive AutoPore V 9600 mercury intrusion porosimeter and a ASAP 2420 BET adsorption apparatus.

The microstructure of the three sets of samples was therefore investigated with Hg intrusion, BET adsorption. Figure 4.10(a) shows that the dominant pore diameter for Sets 1-3 is in approximately 100 nm. There is a slight decrease in the mean pore diameter as the firing temperature increases. Figure 4.10(b) shows that the porous volume available for Hg intrusion decreases with increasing firing temperature. Figure 4.10(b) also displays the anticipated correlation between the internal

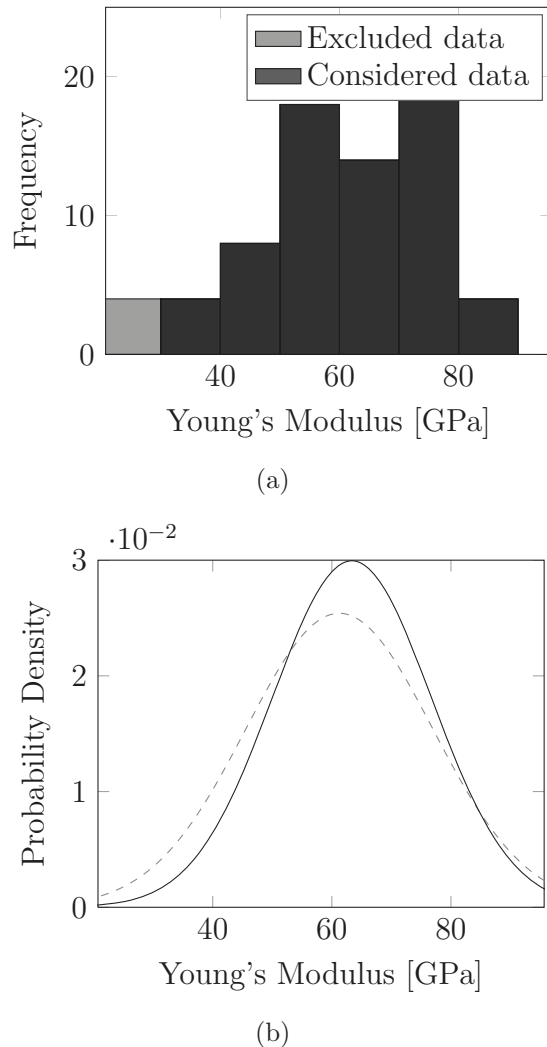


Figure 4.8: (a) Histograms, (b) original (dashed) and corrected (continuous) normal probability distributions of the Young's modulus estimations by nanoindentations for a sample of Set 1.

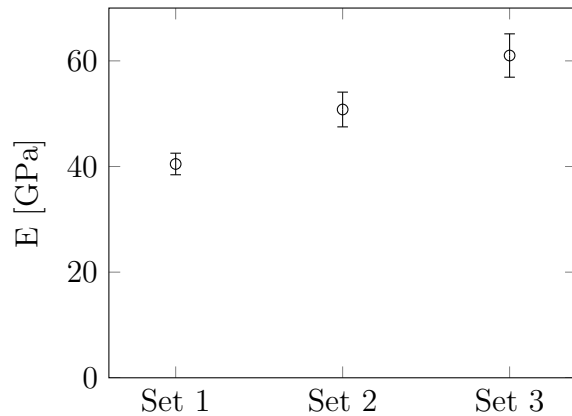


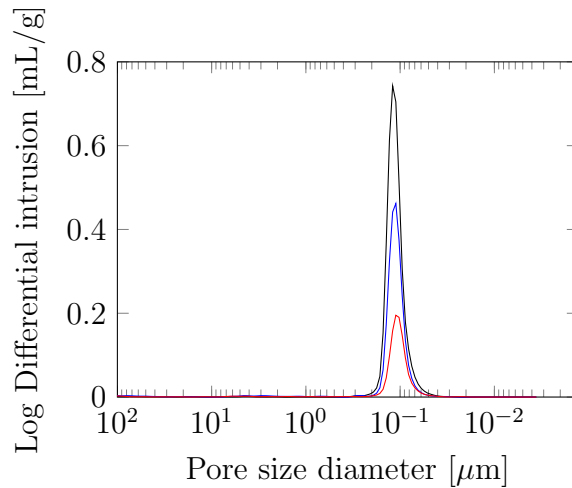
Figure 4.9: Young's modulus of the four-hole cylinders of the three sets of samples evaluated by nanoindentations.

surface area of the sample, measured using BET adsorption, and the pore volume.

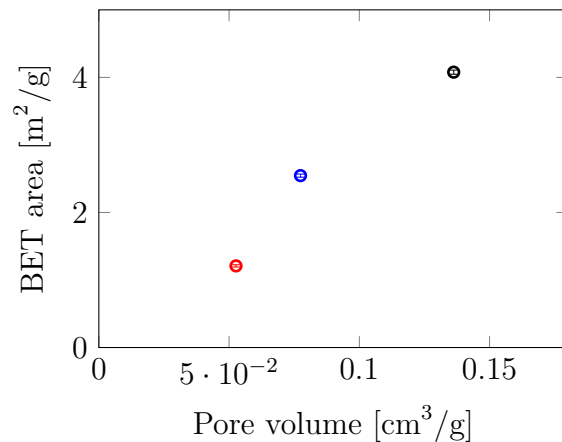
4.7 FESEM

The field emission scanning electron microscopy (FESEM) results have been provided by Dogan Ozkaya (Johnson Matthey). Bars and fragments from the three sets of bars were analysed using a Zeiss ultra 55 field emission electron microscope equipped with in-lens secondary electron and backscattered detectors. The samples were carbon coated prior to analysis to provide a conductive layer for charge dissipation. The high-resolution low-accelerating voltage imaging was performed with an accelerating voltage of 1.6 kV, aperture of 20-30 μm and a working distance of 2-3 mm. The low-resolution general imaging was performed with an accelerating voltage of 20 kV, aperture of 30-60 μm and a working distance of 7-8 mm

The field emission scanning electron microscopy results show that the difference in the microstructure within the samples is not significant. The FESEM analyses of the fragments from the bending tests, show some differences in the microstructural behaviour of the three sets of bars. The fractured sample from Set 1 exhibits mostly



(a)



(b)

Figure 4.10: (a) Pore size distributions from Hg intrusions on a sample from Set 1 (black), Set 2 (blue) and Set 3 (red) and (b) the correlation between the BET area and the pore volume from Hg intrusions.

inter granular fractures, as shown in Figure 4.11(a). The fragments from Set 2 and 3 on the other hand reveal predominantly intra granular fractures, as shown in Figure 4.11(b) and 4.11(c) respectively, indicating stronger grain boundaries.

One sample from each set of bars was also polished to reveal the full cross section to investigate the homogeneity of the microstructure within the samples by comparing the pore size distributions at two sides and in the centre of the cross section. Even though Figure 4.12 shows that the microstructure features within the samples appear to be relatively consistent, this analysis was considered inconclusive. Moreover, due to limitations in the pixel size of the images from the FESEM, the analysis was carried out at scale that was not representative of the actual pore size. The minimum size reported is around $1 \mu\text{m}$ and the average pore size of these samples is about $0.1 \mu\text{m}$.

4.8 Three-point bending test

4.8.1 Experimental setup

The three-point bending test-fixture consists of two supports and a loading platen mounted on instrumented test rig. The parallel pair of semi-cylindrical supports were 20 mm apart and mounted on a monolithic cylinder of aluminium alloy that was placed centrally on the stationary base of the test rig (Instron model 5984 electromechanical test frame). An opposing semi-cylindrical loading platen was mounted centrally on the vertically-moving crosshead of the test rig, below the load-cell, as shown in Figure 5.1(a). The experiments were performed in displacement control, with a crosshead velocity of 0.5 mm/min. The test rig control software (Instron Bluehill 3) recorded load and displacement during each experiment, at 0.1 second intervals. The experiments were recorded with a high-speed video-camera (Vision

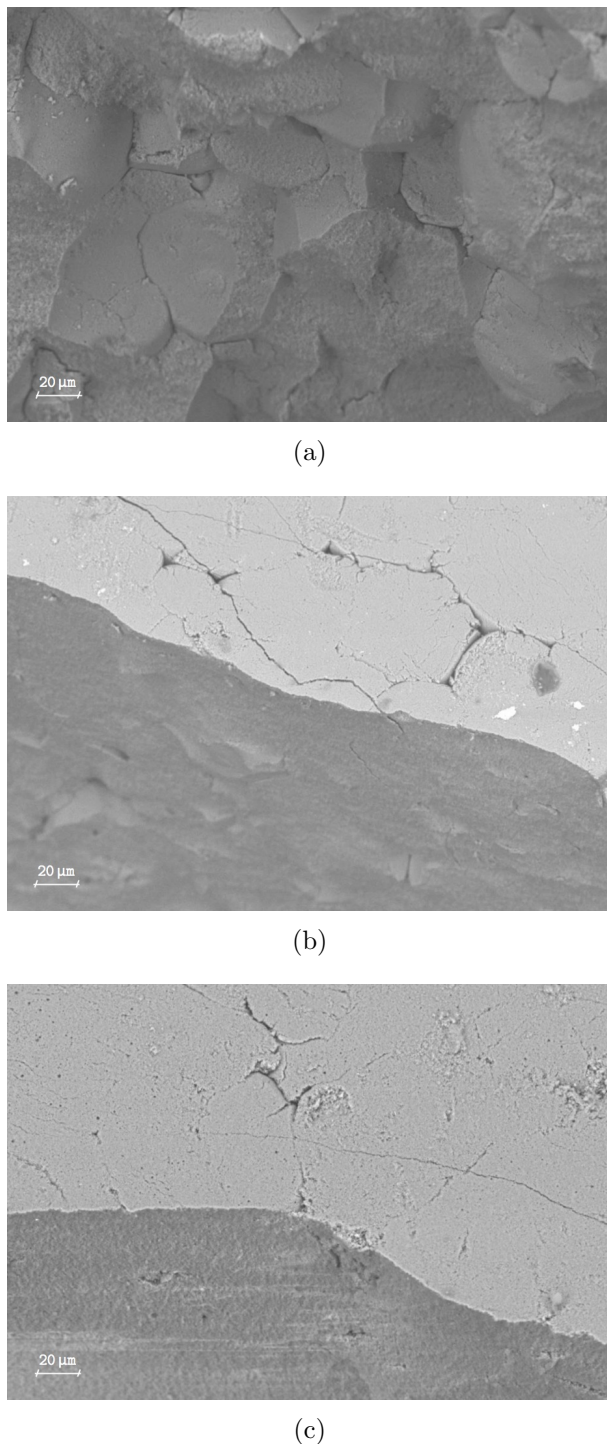


Figure 4.11: FESEM images of the fracture surfaces of bar fragments showing the microstructural failure mode for the three sets of samples. The scanning of the fracture surface of a sample from Set 1 shows a fracture surface with an inter-granular morphology (a), whereas the images from Set 2 (b) and Set 3 (c) show fracture surfaces (below) and the external surface of the sample (above), without visible grain boundaries.

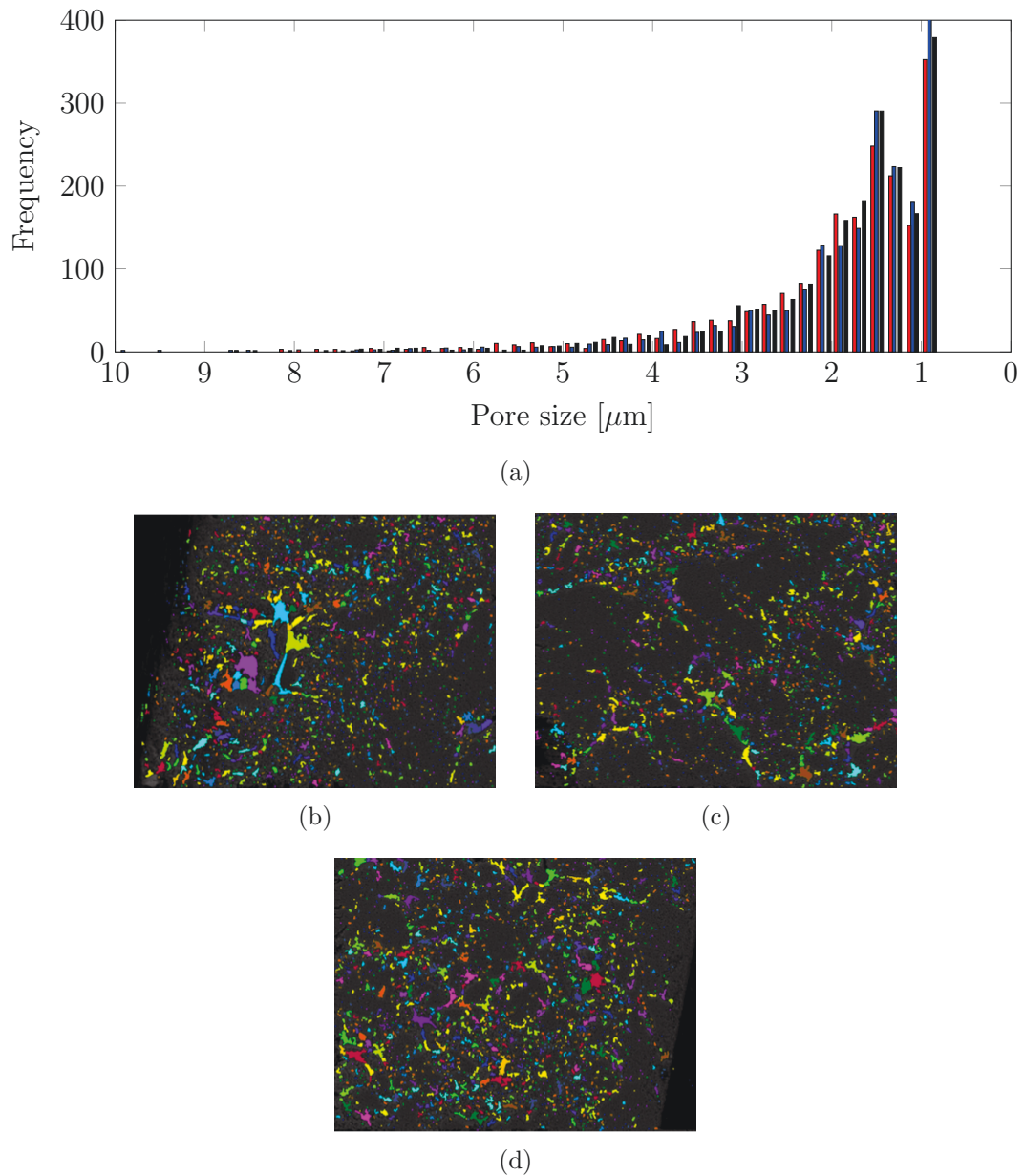


Figure 4.12: (a) Comparison of the microstructure within the thickness of the sample, respectively in black, blue and red bars and the corresponding FESEM images of the (b) left, (c) centre and (d) right portions of the cross section of a sample from Set 1.

Research Phantom v12.1 monochrome, maximum capture rate 6000 frames/second at full-resolution of 1280 by 800 pixels, fitted with a 100 mm macro lens). The optical axis was set normal to the speckled side-face of the specimen. A high-speed video camera was used in order to potentially capture the fracture event at the end of the test, and to allow for the possibility of higher rates of loading in future experiments without a change of equipment. The high-speed capability is not required for this optimisation methodology, however, the monochrome 12-bit (4096 intensity levels) sensor of this camera is well suited to digital image correlation, compared with (for example) a 24-bit (3 x 256 levels) colour sensor.

4.8.2 Flexural strength

Before failure, according to the Euler-Bernoulli beam theory, a homogeneous bar being tested in three-point bending test, experiences the maximum tensile and compressive stress respectively in its bottom and top surfaces, in the exact middle of the two supports. Since the tested material are assumed to fail under tensile stress before failing under compression, a fracture will initiate from the bottom side when the tensile stress reaches the value of the tensile strength of the tested material. By solving the Euler-Bernoulli differential equation it is possible to express the maximum tensile stress experienced by the specimen as a function of the applied load and moreover infer the tensile strength and the Young's modulus from the applied load and the beam deflection. The ISO 14704:2016 Section 8 suggests to evaluate the flexural tensile strength (f_t) with equation (4.2), where s is the span between the two supports and H is the height and width of a bar with a square cross-section. As mentioned before, the stress field induced in the specimen by the controlled boundary conditions not only restricts the area where the fracture can initiate, but also constrains the opening mode when the fracture is propagating. In fact, neglect-

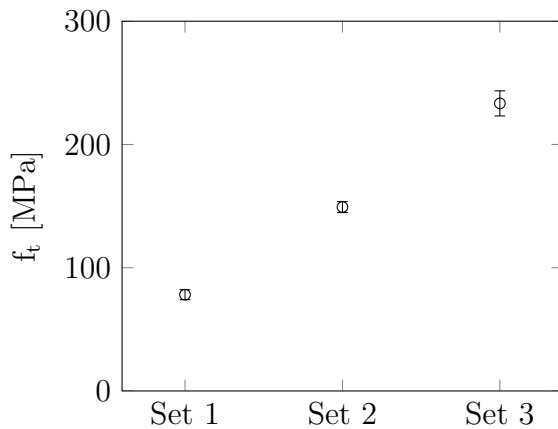


Figure 4.13: Averages and standard errors of the flexural strength obtained with three-point bending tests for the three sets of bar samples.

ing the possible effects of microscale inhomogeneities and anisotropies, the material points that are failing experience a pure horizontal extension, which is normal to the plane of the crack, in a mode I opening fashion. The averages and standard errors of the flexural strengths obtained with three-point bending tests for the three sets of bar samples are reported in Figure 4.13.

$$f_t = \frac{3F_{Max}s}{2H^3} \quad (4.2)$$

4.8.3 Elastic modulus

The European Standard EN 843-2:2006 Section 4 describes the standard methodology to determine the Young's modulus of monolithic ceramics at room temperature. These international guidelines refer to samples that are required to be big enough to employ spans greater than 40 mm. Methods A.1 suggests to record the force-deflection curve during three-point bending tests and employ equations (4.3) to calculate the Young's modulus, where s is the span between the two supports, H is

the height and width of a bar with a square cross-section and ΔF and Δw are the recorded change in force and deflection respectively.

$$E = \frac{\Delta F s^3}{4 \Delta w H^4} \quad (4.3)$$

In some cases, the specimens that are to be tested are too small to allow for a 40mm span, because of either technological or economic constraints, and this was the case of the pellets employed in the study. Since the deformations of highly stiff materials are inevitably small and therefore not easy to determine with a high level of confidence, the estimated Young's modulus with Methods A.1 can be significantly affected by experimental errors. Moreover, Methods A.2 and A.3 from Section 4 of EN 843-2:2006 cannot be applied either, because the specimens are too small to allow a displacement transducer or strain-gauge to be accurately installed and employed with a high level of confidence. As has been introduced in Section 2.1, this gave an opportunity for the development of a more reliable method for the Young's modulus evaluation. This optimisation methodology is described in the next sections and the results are then compared with the ones obtained from other standard tests.

4.8.4 Digital image correlation analysis

Prior to testing, one side-face of each specimen had a random speckle pattern applied. Digital image correlation analyses were performed on the image sequences recorded by the high-speed camera, using commercially available software (LaVision DaVis/Strainmaster) LaVision Inc. (n.d.). For each experiment, each image in the sequence was compared with the same initial or reference image representing the undeformed specimen. The Region Of Interest (ROI) was the full width of the

image (1280 pixels) by typically 220 pixels high, depending on the height of the specimen. Since each image was a single view of the side-face of the specimen, only in-plane deformations of the ROI were produced as an output of the DIC analysis. The primary output of a 2D DIC analysis is a matrix with the vertical (d_v) and horizontal (d_h) displacement values at each location in a regular grid, based on the initial pixel locations or indices of the reference image. For these experiments, the beam specimens were aligned parallel to the image edges, so each x value represented a horizontal position within the specimen and each y value represented a vertical position within the height of the specimen. The d_v and d_h data for each image was exported from the LaVision software and further analysed using MatlabThe MathWorks Inc. (n.d.) for the deflection profile calculation and the Young's modulus optimisation.

4.8.5 Full deflection profile calculation

The samples were prepared and tested as described in the Methods sections. The displacement field of the beam (Figure 4.14) is discretized in a regular grid and for each frame the DIC software calculates the vertical (d_v) and horizontal (d_h) displacement of each cell in the grid. The mean vertical displacement of the bar along the horizontal axis $w'(x)$ is calculated for each frame by averaging the displacement of the corresponding cells through the height of the beam, as shown in equation (4.4). The averaged vertical displacement of the beam is then corrected by fixing the vertical displacement of the left $w(x_l)$ and right $w(x_r)$ support to zero. This is done by applying to the averaged vertical displacement the rigid translation C and rotation φ , as defined in equations (4.5) and schematised in Figure 4.18. The effects of the rotation on the horizontal axis can be neglected since they are much smaller than the cell discretisation. The corrected deflection profile can be calculated for

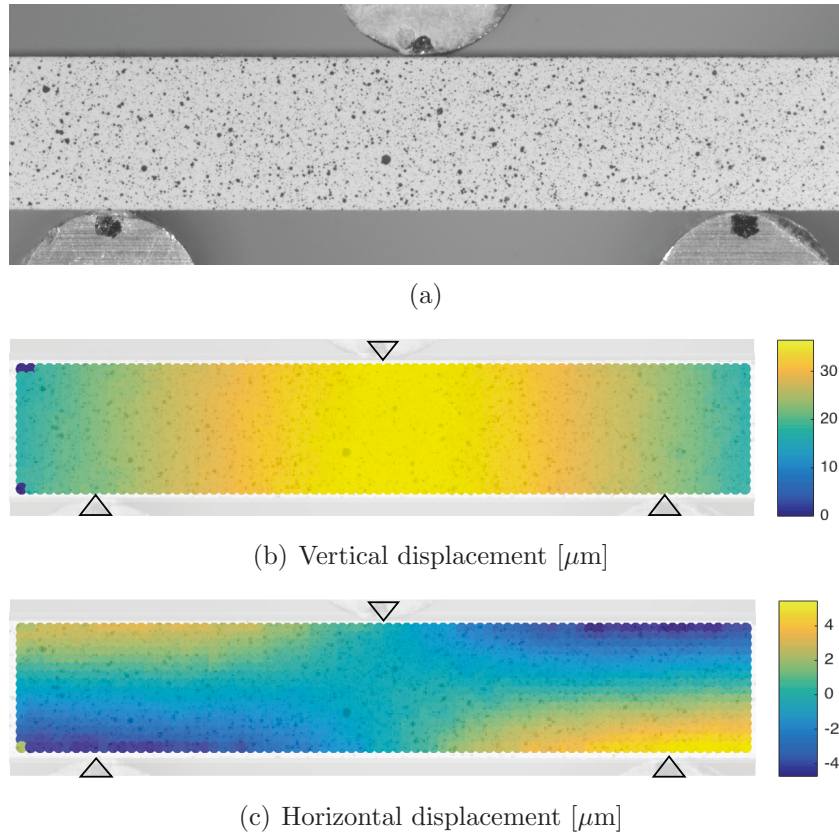


Figure 4.14: (a) An example of the frames used to extrapolate the displacement field of the beam during a three point bending test, (b) the vertical displacement field d_v and (c) the horizontal displacement field d_h before failure.

each frame of the recorded experiment with equation (4.6) and an example is shown in Figure 4.16.

$$w'_i(x) = \frac{\sum_{k=0}^N d_v(x, y_k)}{N} \quad (4.4)$$

$$\begin{cases} C_i &= w'_i(x_l) \\ \phi_i &= \arctan \frac{w'_i(x_r) - C_i}{x_r - x_l} \end{cases} \quad (4.5)$$

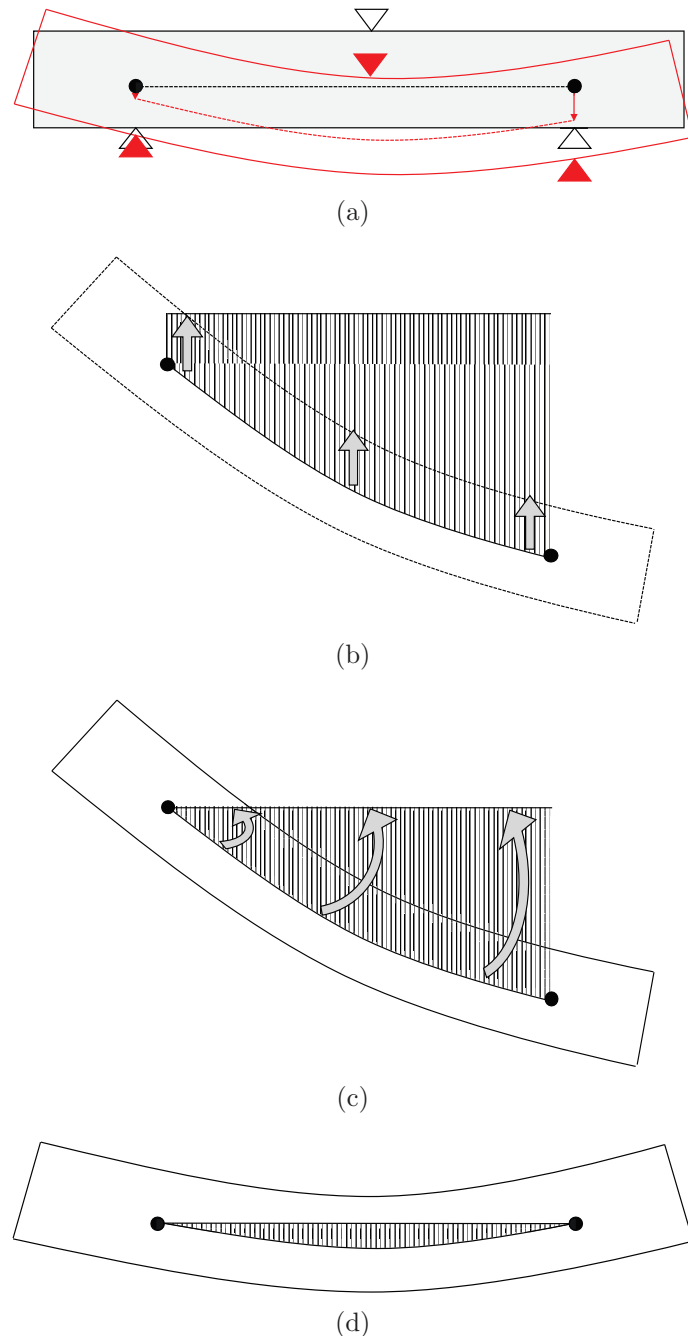


Figure 4.15: (a) Sample configuration before (black) and during the test (red). Schematic representation of the average vertical displacement correction by applying a rigid vertical translation (b) and rotation (c) to obtain the corrected full deflection profile (d) of each frame.

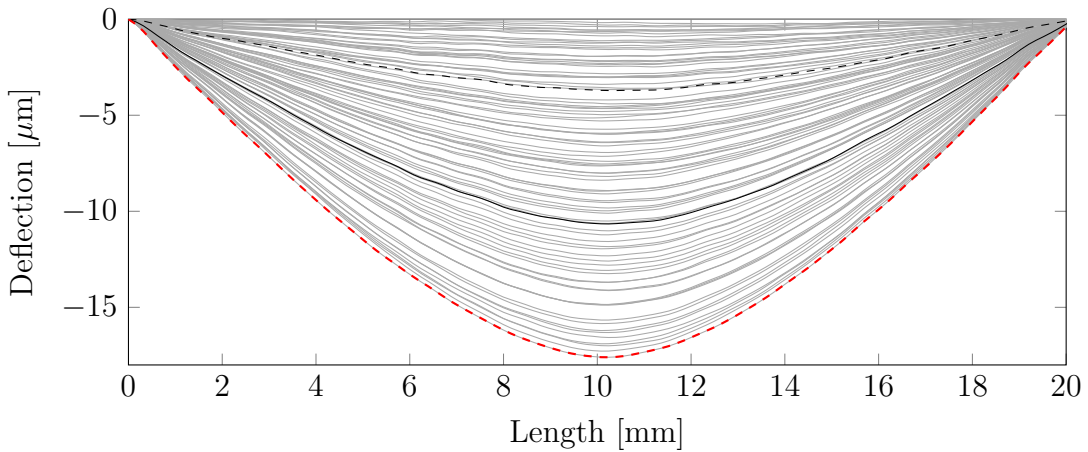


Figure 4.16: Typical sequence of deflection profiles before failure (grey). In particular, the profile at 20% (dashed black), 60% (black) and 100% (dashed red) of peak load are shown.

$$w_i(x) = w'_i(x) - [C_i + (x - x_l) * \sin \phi_i] \quad (4.6)$$

4.8.6 Young's modulus optimisation

The sequences of beam deflection profiles were synchronised with the load histories recorded by the test rig transducer, resulting in a value of applied load for each profile. Assuming that the beam cross sections remain planar and normal to the deformed axis of the beam, the theoretical vertical displacement profile (w_{EB}) associated with the applied load can be express as a function of the Young's modulus (E) of an equivalent linear-elastic isotropic and homogeneous beam with a defined geometry. In equation (4.7) the theoretical vertical displacement is defined as a function of the location (x) and E , whereas the moment of inertia (I) and the span between the two supports (s) are two constants that are fixed with the geometry of the tested beam. A single value of Young's modulus can then be determined for

each frame, index= i , by minimising the sum of the squares of the differences between the theoretical and the corresponding experimental deflection (least squares) along the entire length of the beam between the supports. By repeating the minimisation shown in equation (4.8) for each frame, it is possible to determine a series of intermediate Young's moduli (E_i) that best represent the deflection of the beam for each applied load at each frame. These intermediate moduli can then be used to define a single value of Young's modulus that best represents the linear stress-strain relationship for the tested material over any selected range of applied load. The range between the 20% and 80% of the peak load was selected to define a single value of Young's modulus for each specimen. The intermediate moduli were therefore converted to their corresponding values of deflection at mid-span and a linear least squares regression was performed on the variable of deflection for the applied load in the defined range. A value of Young's modulus was then determined for each specimen with equation (4.9), where H is the height of the sample and m is the slope of the corresponding line of best fit.

$$w_{EB}(x, E) = \begin{cases} -\frac{Px(4x^2 - 3s^2)}{48EI}, & \text{for } 0 \leq x \leq \frac{s}{2} \\ \frac{P(x-s)(s^2 - 8sx + 4x^2)}{48EI}, & \text{for } \frac{s}{2} < x \leq s \end{cases} \quad (4.7)$$

$$\sum_{k=0}^N (w_{EB}(x_k, E) - w_i(x_k))^2 = \min \quad \Rightarrow \quad E = E_i \quad (4.8)$$

$$E = m \frac{s^3}{4 H^4} \quad (4.9)$$

4.8.7 Uncertainty and optical distortions

The proposed approach relies on the assumption that the plane of the target is not displacing significantly in the direction normal to that plane, that is, toward or away from the camera, which would falsely indicate expansion or contraction respectively. For these experiments, this can be said to be true, since the maximum in-plane displacements in the direction of loading, which would be dominant, were of the order of only 1 or 2 pixels. To estimate the error for a possible optical distortion, an independent experiment was considered. A constant vertical displacement was applied to an identical speckle panel connected to the top punch of the three-point bending rig, as shown in Figure 4.17(a). The experiment was performed in displacement control, with a cross-head velocity of 0.4 mm/sec that on average corresponds to a vertical displacement of 0.8 μm per frame. Since the maximum vertical displacement before correction experienced on average by the bars before failure was generally 30-40 μm , depending on the tested sample, e.g. in Figure 4.14, the error was conservatively evaluated over 100 frames that correspond to a total vertical displacement of 80 μm , which is twice the typical displacement range of the tested sample. The same procedure applied to the beam samples was employed to calculate the horizontal profile of the vertical displacement of the speckle panel. In Figure 4.17(b) the corrected beam deflection is shown for each considered frame. Since the panel is subjected to a rigid vertical translation with no deflection, the estimate error for each location of the deflection profile calculated with this optimisation methodology can be defined as the maximum absolute value of the deflection profile in each frame. The estimated error, as shown in Figure 4.17(c) (dashed line), tends to a value between 0.1 and 0.2 μm . This error is too conservative when the deflection profile is employed for the calculation of Young's modulus. In this case all the locations of the deflection profile are instead compared to the theoretical deflection in the optimisation process. The estimate of the deflection error in this case can then be defined as the maximum

deflection (halfway between the two supports) of the best interpolation curve given by the Euler-Bernoulli theoretical deflection profile. In this case the estimated error, as shown in Figure 4.17(c) (continuous line), is lower than the previous. The maximum value of this estimated error tends to $0.1 \mu\text{m}$ and corresponds to a vertical displacement similar to the maximum before failure in the actual test. Since the Young's modulus for any applied load is a linear function of the maximum (middle) value of the beam deflection profile, and that this value varies between 15 and 20 μm , depending on the tested sample, the relative error caused by optical distortions on the last estimates of the Young's modulus calculated before failure is between 0.5% and 0.7%.

4.9 Precision and accuracy: a comparison with the standard flexural methods

In the context of ceramic samples, the European Standard EN 843-2:2006 Section 4 describes the standard methodology to determine the Young's modulus of monolithic ceramics at room temperature. These international guidelines refer to samples that are required to be big enough to employ spans greater than 40 mm.

In some cases, the specimens that are to be tested are too small to allow for a 40mm span, because of either technological or economic constraints, and this was the case of the pellets used in the present work. Moreover, Methods A.2 and A.3 from Section 4 of EN 843-2:2006 cannot be applied to this type of specimens, because they are too small to allow a displacement transducer or strain-gauge to be accurately installed and employed with a high level of confidence. In summary, some specimens that need testing are too small for the standard method to be applied.

Digital Image Correlation (DIC) can be employed to determine full-field displace-

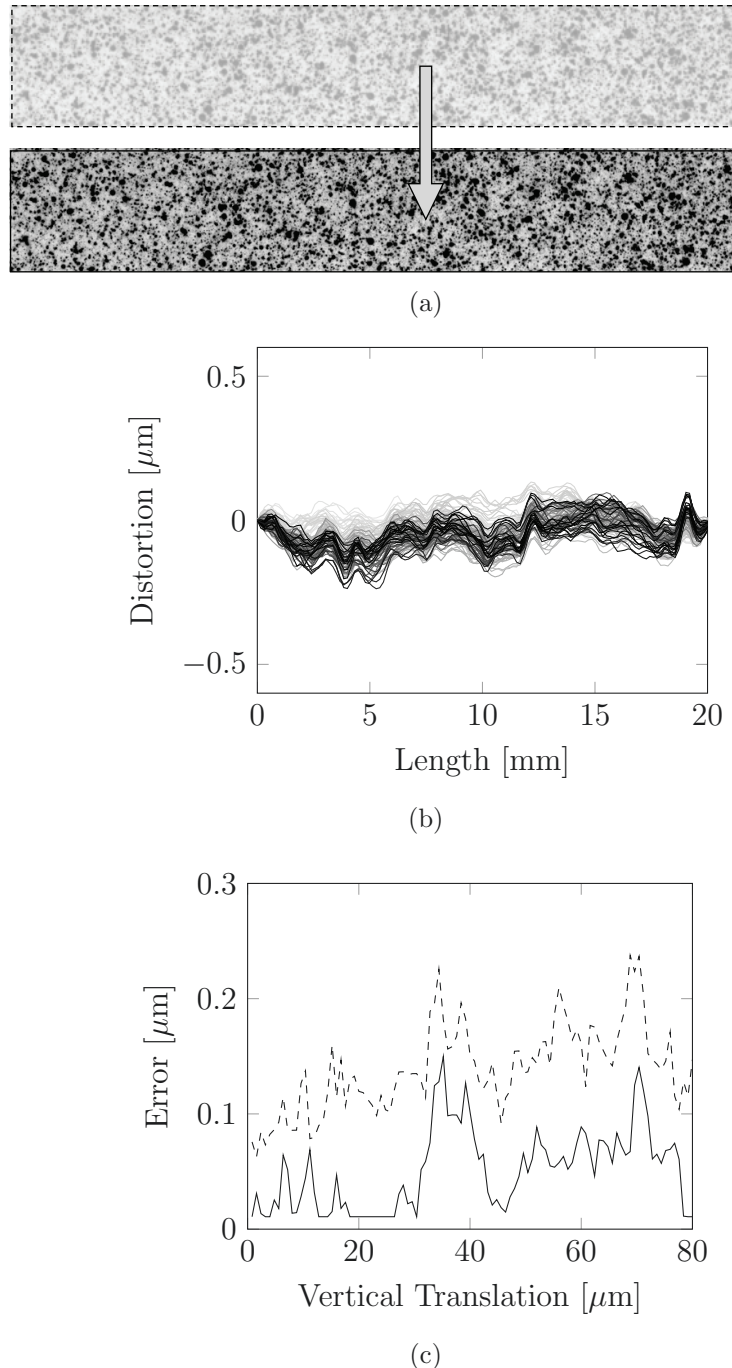


Figure 4.17: (a) Beam configuration before and after applying a rigid body motion. (b) Optical distortion in the horizontal profile of the vertical displacement of the speckle panel during the experiment. (c) The trend of the estimated maximum errors for each frame.

ments, deformations and strains from sequences of images. The use of DIC to obtain equivalent experimental data to that which can be obtained using conventional physical transducers (for example, the vertical displacement of three discrete points on the lower surface of the beam or the span-wise strain at mid-span) is not a standard method that is widely adopted for three-point bending tests. However, it is possible to use sets of DIC data obtained in this manner to calculate the Young's modulus using the algorithms in EN 843-2:2006 Section 4, equations (1) and (6).

What follows is a comparison between the proposed methodology and the standard approaches suggested in EN 843-2:2006, employing both displacement and strain data extracted at discrete locations from the full-field DIC deformation data. As shown in Figure 4.18(a), we compare the following:

- The proposed methodology;
- Three virtual displacements (mid-span and at both supports, three sets placed at different heights on the viewed surface of the beam);
- Two virtual strain gauges placed close to the lower surface of the beam (corrected to indicate a value of strain on the lower surface).

For the purposes of this comparison, data sets from a single representative bending test have been used. This allows to make a comparison based on the different methodology, effectively excluding the impact of quality variations that are normally obtained by comparing different sets of results. The algorithm suggested in EN 843-2:2006 for displacement transducers is equivalent to calculating the Young's modulus by Euler-Bernoulli bending theory, but using only the maximum vertical displacement at mid-span relative to the average vertical displacement at the two supports, as shown in Figure 4.18(b).

The proposed method employs the entire vertical displacement data set, covering the whole observed surface of the beam, in order to obtain the full deflection profile for the specimen. This deflection profile is corrected to eliminate rigid-body translations and rotation, then analysed to determine the Euler-Bernoulli deflection curve of best fit, as shown in Figure 4.18(b). By repeating this process for each frame, it is possible to determine a series of intermediate Young's moduli that best represent the deflection of the beam for each applied load at each frame. These intermediate moduli can subsequently be used to define a single value of Young's modulus that best represents the linear stress-strain relationship for the tested material. The employment of a larger set of displacement data for the determination of the beam bending and of a more sophisticated method to account for the rigid-body translations and rotation are the key features that allow the proposed method to have a higher level of precision compared to the standard method with three displacement transducers.

In order to compare the levels of precision of the two methodologies, the intermediate Young's moduli determined using the proposed methodology were converted back to their corresponding values of deflection at mid-span, for each applied load. In this way it is possible to compare the force-deflection curve from the proposed methodology (i.e. full-field) to those obtained from the DIC-equivalent standard method based on sets of virtual displacement gauges placed at different heights of the beam. The values of force and deflection at 20% and 80% of the peak load were then used to estimate the Young's modulus from the three curves following the suggested procedure in the EN 843-2:2006 Section 4.

The force-deflection curves shown in Figure 4.19 suggest that the standard method can be sensitive to the choice of location of the virtual gauges on the surface of the beam, in particular to whether the virtual gauges are located near the inner or outer arc of the deflecting beam. This variability in the results from the standard

method indicates a lower precision, as it generates in our examples three values of Young's modulus that differ by more than 3%, with a lower value obtained in the location of lowermost positions, which are analogous to the transducer positions indicated in the EN 843-2:2006 Section 4. In the supporting reference for the EN 843-2:2006 Morrell *et al.* (1999) it is noted that the standard quasi-static flexural method generally produces lower values than other standard methods on ceramic materials. Instead, the proposed methodology employs the data from the whole surface of the beam, from the inner to the outer arc, eliminating the variability due to the choices of the virtual transducer locations. The proposed methodology generates a higher Young's modulus than those determined by virtual displacement gauges (using DIC data) and adopting standard calculation methods. This suggests that the proposed methodology achieves higher accuracy and may be removing a potential bias towards lower values that is likely to be imposed by the standard quasi-static flexural method.

In Figure 4.20(a) the force has been normalised with the peak load and the data range has been limited to 20% to 80% of the peak load (within the 10% - 90% range indicated by EN 843-2:2006). Also plotted are the trend lines as determined by the standard analysis method, which only considers values at two operator-selected evaluation points (for example, 20% and 80% of the peak load). A quantification of the level of precision can be obtained by calculating the sum of squared residuals (SSR) between values indicated by the linear trend and the actual deflection data, which represents the measurement deviation from the value indicated by that trend. The proposed full-field methodology has a lower SSR (tabulated within Figure 4.20(a), 4.28 against 5.51, 7.60 and 8.10 μm^2), and therefore a higher level of precision.

The intermediate Young's moduli from the proposed methodology were also used to back-calculate the corresponding values of horizontal strain on the lower surface of the specimen at mid-span for each value of applied load. Comparable values of

horizontal strain were also extracted directly from the full-field DIC deformation data, at two discrete locations just above the lower edge of the observed surface. These were each corrected to an equivalent value at the lower surface. The resulting force-strain data (from 20% to 80% of peak load) is plotted in Figure 4.20(b). The values of force and strain at 20% and 80% of peak load were then used to estimate the Young's modulus, as suggested in EN 843-2:2006 Section 4. Again, a quantification of the level of precision can be obtained also from the calculation of the SSR between values indicated by the linear trend and the actual strain data. The proposed methodology based on full-field DIC has a SSR that is two orders of magnitude smaller than the ones obtained with the standard method (tabulated within Figure 4.20(b) $2.07 \cdot 10^{-8}$ against $1.44 \cdot 10^{-6}$, and $2.08 \cdot 10^{-6}$), and therefore a much higher level of precision.

This comparison has been carried out for an experiment that was recorded with state of the art equipment and therefore only high resolution images were analysed using DIC. It is reasonable to assume that the improvements in precision of the proposed methodology would be more significant for lower resolution images because the entire deformation data set (support to support and over the full height) has been used rather than much smaller subsets of that data representing just a few discrete locations.

4.10 Comparison of the experimental results

This optimisation methodology was applied to the bending test recordings of 15 samples that were sintered, as described in Methods, to obtain three grades of porosity, with Young's moduli expected to be in the 60-250 GPa range. In Figure 4.21 the estimate of the Young's modulus of the tested samples is plotted for each frame as each three-point bending test progresses. The optimisation becomes stable after

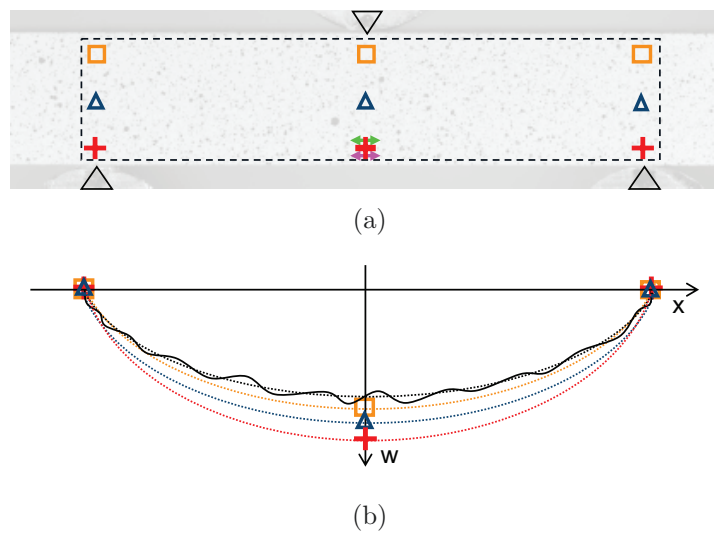


Figure 4.18: (a) Representation of the points from which the vertical displacements are calculated with a standard method using three different sets of virtual displacement gauges (orange squares, blue triangles and red crosses) and the area used with the proposed methodology (black dashed line). The two arrows (green and magenta) represent the locations of two virtual strain gauges. (b) Schematic representation of the different determination of the vertical displacements with the standard method from three data points at two different locations (yellow, blue and red) and with the proposed methodology from the best interpolation of the full deflection profile (black).

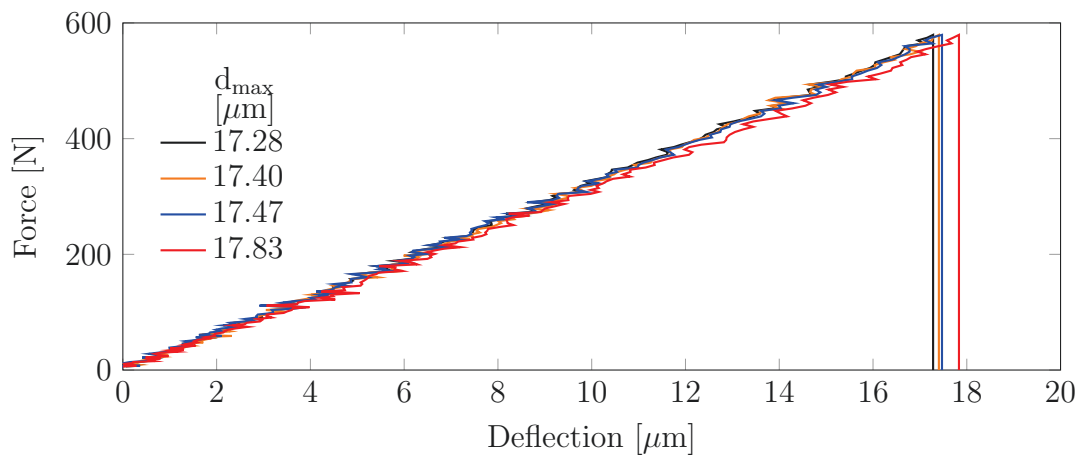


Figure 4.19: Comparison of the force-deflection curves calculated with the standard method from the three sets of three data points (orange, blue and red) and with the proposed methodology from the best interpolation of the full deflection profile (black).

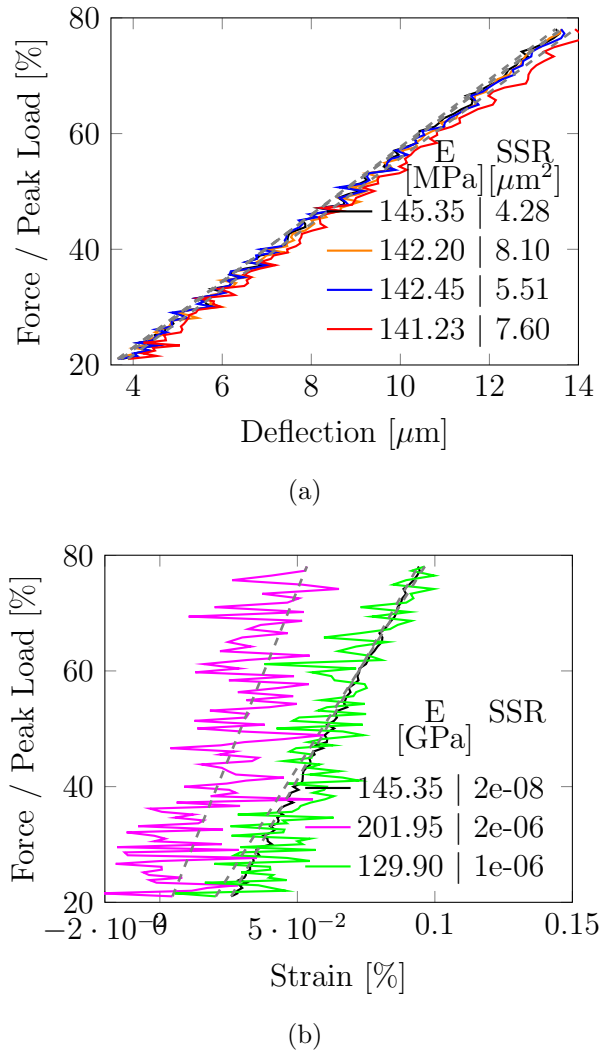


Figure 4.20: (a) Subset of the data shown in Figure 4.19 with force as a percentage of the peak load and limited to the range 20% and 80%. The corresponding linear trends (grey dashed lines) obtained from the Young's modulus obtained from the two curves at 20% and 80% of the peak load are also plotted for each set. (b) Comparison of the force-strain curves from the two virtual strain gauges and from the proposed methodology. The corresponding linear trends (grey dashed lines) obtained from the Young's modulus extrapolated from the three curves at 20% and 80% of the peak load are also reported in the graph.

typically forty frames (about 20-30% of the peak load) due to the fact that in the first phase of the experiment, i.e. when the punch makes contact with the sample, the load and deformations are of very low magnitude and more significantly affected by noise in the signal from the transducer and errors in the DIC analysis. The distribution of results is consistent for the three sets of bars and the mean values and standard errors are reported in Table 4.3.

Bars from the three sets of samples were also tested with ultrasonic techniques. As explained in the previous sections, the velocity of the longitudinal waves propagating through the sample can be expressed as $V_L = \frac{2L}{\Delta t}$. The relation between density (ρ), Lamé constants (λ and μ) of the specimen and the longitudinal wave velocity is $V_L = \sqrt{\frac{\lambda+2\mu}{\rho}}$ [Timoshenko (1970)]. This relation is only valid for a wave propagating through a homogeneous elastic medium.

The microstructure of the three sets of samples was therefore investigated with Hg intrusion, BET adsorption and FESEM. Figure 4.10(a) shows that the dominant pore diameter for Sets 1-3 is approximately 100 nm. There is a slight decrease in the mean pore diameter as the firing temperature increases. Figure 4.10(b) shows that the porous volume available for Hg intrusion decreases with increasing firing temperature. Figure 4.10(b) also displays the anticipated correlation between the internal surface area of the sample, measured using BET adsorption, and the pore volume. The FESEM results show that the difference in the microstructure within the samples is not significant. The FESEM analyses of the fragments from the bending tests, show some differences in the microstructural behaviour of the three sets of bars. The fractured sample from Set 1 exhibits mostly inter granular fractures, as shown in Figure 4.11(a). The fragments from Set 2 and 3 on the other hand reveal predominantly intra granular fractures, as shown in Figure 4.11(b) and 4.11(c) respectively, indicating stronger grain boundaries.

A 25 MHz ultrasonic transducer was employed for the tests and the measured lower

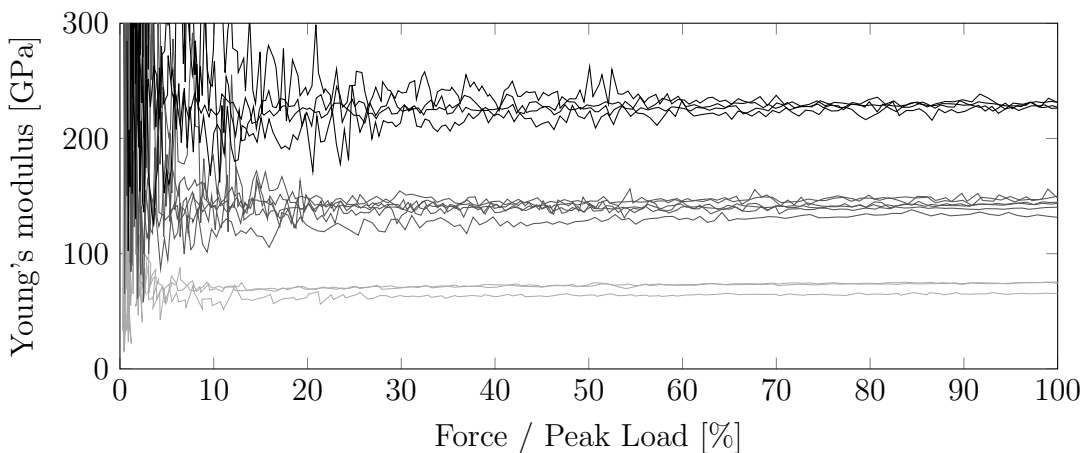


Figure 4.21: Young's modulus optimisation from full displacement profiles of the bars of Set 1 (light grey), Set 2 (dark grey) and Set 3 (black).

wave velocity measured was above 5,000 m/s. Therefore the wavelength of the transmitted waves is above $200 \mu\text{m}$. The high ratio between the wavelength and the average pore size of the specimens ($0.1 \mu\text{m}$) allows to trait the samples as homogeneous media with respect to the transmitted ultrasonic waves.

One specimen from each set of samples was also tested with nanoindentations. For each bar, one hundred indentations have been performed for statistical correction to minimize the experimental error. The histograms and normal probability distributions of the Young's modulus were estimated with one hundred nanoindentations on the surface of a sample. A correction was performed by excluding the experimental results that were 50% either lower or higher than the average value of the entire distribution. The results from the indentations on a sample from Set 1 are shown in Figure 4.8.

The distributions of the extrapolated Young's moduli from the ultrasonic tests and nanoindentations are in agreement with the ones from this optimisation methodology and the mean values and standard errors are also reported in Table 4.3. A comparison of the results from the three tests is also shown in Figure 4.22.

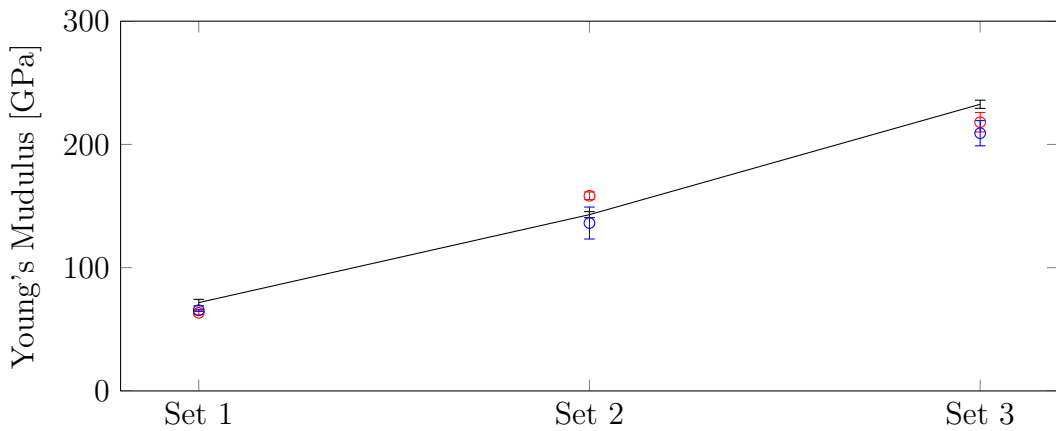


Figure 4.22: Comparison of the Young's moduli from this optimisation methodology (black), ultrasonic tests (blue) and nanoindentations (red).

Table 4.3: Mean values and standard errors of the Young's moduli from this optimisation methodology, ultrasonic tests and nanoindentations.

	Optimisation method Set	Ultrasonic test [GPa]	Nanoindentations [GPa]
1	71.67 ± 2.66	65.45 ± 0.83	63.36 ± 1.59
2	143.04 ± 2.45	136.22 ± 12.98	158.34 ± 3.11
3	232.57 ± 3.31	209.11 ± 10.24	218.02 ± 7.92

4.11 Concluding remarks

As has been described in Section 1.2, the final goal of this research project is to achieve a better understanding of different pellet shapes and their inherent mechanical properties by means of numerical simulations, the findings of which could be of industrial interest by contributing to improvements in the performance of catalysts. To obtain realistic simulations of fracture propagation of ceramic pellets it is essential to first characterise the mechanical properties of the material that makes up the particles and to define all the numerical parameters that are needed for their numerical simulations. These parameters have been described in Section 3.1.2.5, where their physical meaning has also been illustrated. As seen in Section 2.1, the mechanical characterisation of engineered high performance materials (e.g. the ceramics employed as catalyst supports) is a crucial field in material science. Since porous ceramics are generally considered to be brittle elastic [David (2015)], Young's modulus and tensile strength are two of the main parameters needed in order to predict the mechanical behaviour of systems made from such components. Among various testing methods illustrated and employed in this research (e.g. ultrasonic test, nanoindentations, mercury (Hg) intrusion, etc.), quasi-statically determined parameters such the elastic modulus from uniaxial compression and the flexural modulus, are generally preferred because they require more conventional and simpler testing machineries and specimen preparation. In addition, they are also generally considered to be more representative of in-service loading conditions [Eissa & Kazi (1988)]. As discussed in more detail below, the ceramic materials needed to be addressed in this study were found to raise numerous challenges when it came to strength testing.

The material properties of small ceramic samples with different geometries (i.e. prismatic bars, discs and cylindrical pellets with four holes) were needed in order to

perform Solidity FEMDEM numerical simulations and thereby evaluate the likely fracture behaviour of complex shaped pellets. These sets of samples provided by Johnson Matthey were stated to have been sintered with an alumina powder and procedures similar to the processes commonly employed to produce standard catalyst supports used in industrial processes.

4.11.1 Cylindrical samples

The aim of using four-holed pellets under Brazilian disc type compression testing is to compare a complex fracture evolution seen from experiment with that predicted by simulation and hence gain confidence that the code can capture the overall strength reduction of having holes and to a reasonable extent capture the fracture patterns. This was successfully achieved and the effect of the stronger and weaker orientation of the hole positions with respect to the disc loading axis, as captured by the simulations was described in Chapter 3. However, to set the correct material properties for these simulation was somewhat problematic as ceramic properties can easily vary with compaction pressure and firing temperature and it was therefore necessary to perform new Brazilian disc indirect tensile tests on disc pellets with the same compaction pressure and firing temperature as the four-holed pellets. As the four-holed pellets were larger and used a different compaction die than the standard discs used for the Brazilian test, two disc sizes were used to represent the possible ceramic material strength variation. The two sets of values of the Brazilian indirect tensile strength were then calculated and the results were reported in Section 4.3.1. The strengths of the three sets of cylindrical pellets with four holes were then assumed to be equal to the average strengths of the corresponding sets of discs.

Since standard Brazilian disc tests do not provide an estimate of Young's modulus, the values for the four-hole cylindrical samples were inferred by nanoindentations

and the results have been reported in Section 4.5. It is important to point out that the values of strength and stiffness obtained for these cylindrical specimens were lower than the expected values for similar porous alumina samples that have been reported in the literature [Lam *et al.* (1994)]. Figure 4.23 summarises the tensile strengths of the tested samples with different geometries. Arising from this discussion, it is therefore proposed that further research needs to be undertaken to understand how different die compaction and sintering tools can affect the final material properties of catalyst pellets.

In this context, it is interesting to revisit the problem faced early in this research when an estimate for the strength and stiffness parameters of the three prismatic bars samples was also needed to proceed with the code validation campaign. The challenges were to lead to the development of a new three-point bending testing procedure.

4.11.2 Prismatic bars

Three-point bending tests were to be employed to evaluate the flexural strengths of the three sets of bars and the results have been presented in Section 4.8.2. Prima facie estimates of Young's moduli of the three sets of bars could have also been evaluated with the same tests. As illustrated in Section 4.9, the European Standard EN 843-2:2006 Section 4 describes the standard methodology to determine the Young's modulus of monolithic ceramics at room temperature. These international guidelines refer to samples that are required to be big enough to employ spans greater than 40 mm. The specimens that were to be tested in the present work were needed to be representative of the small industrially used pellets and were therefore too small to allow for a 40 mm span. Moreover, Methods A.2 and A.3 from Section 4 of EN 843-2:2006 could not be applied to these specimens, because they were too

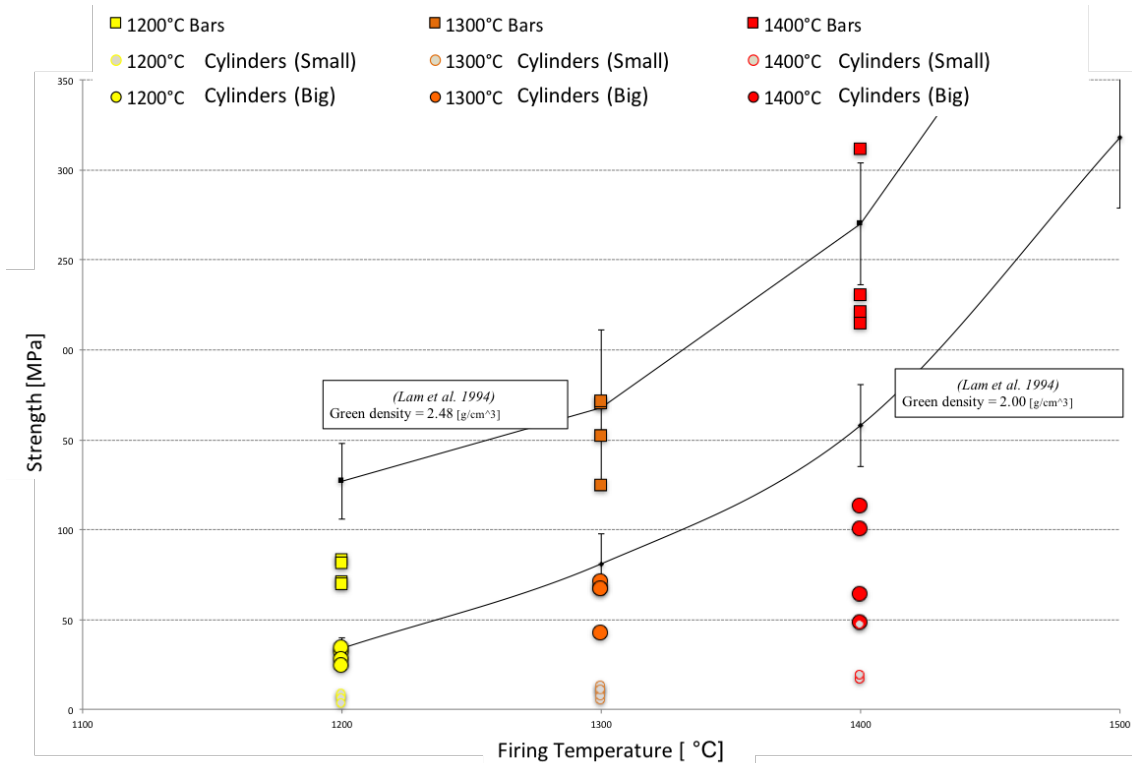


Figure 4.23: Summary of the tensile strengths evaluated for the prismatic bars (squares), small and big cylinders (circles) fired at different temperatures. The results are compared with values of strength of alumna samples with similar green densities and fired at the same temperatures that have been reported in the literature [Lam *et al.* (1994)].

small to allow a displacement transducer or strain-gauge to be accurately installed and employed with a high level of confidence. In summary, the prismatic bars that need testing were too small for the standard method to be applied. For this reason a new methodology for the calculation of the full deflection profile from video recordings of bending tests and an optimisation algorithm for the characterisation of Young's modulus were developed, as shown in Section 4.8.5 and 4.8.6. In order to investigate the applicability of the new method, a quantification of the effects of optical distortions and a comparison with other standard tests have been presented in Section 4.8.7 and 4.9. The presented results not only confirmed that the method could be used to estimate the stiffness of the specimens that were to be tested in the present work, but also showed the capabilities of this procedure to evaluate the Young's modulus of small and highly stiff specimens with greater accuracy than previously possible with bending tests, by employing all the available information from the video recording of the tests. In other words, the proposed methodology extends to this class of materials the possibility to evaluate both the elastic modulus and the tensile strength with a single mechanical test, without the need for other experimental tools. Although the experiments that have been reported refer to prismatic alumina bars, the methodology can be extended to cylindrical or other extruded shapes or even samples with higher aspect ratio that exhibit brittle elastic behaviours. Further research could also be undertaken to extend the method to materials with more complex constitutive behaviour, such as specimens that exhibit significant plastic deformations before failure. Current developments in the Solidity FEMDEM code now allow the simulation of plastic deformations [Karantzoulis *et al.* (2013)]. A possible avenue for future work could be to use the code to perform back analysis of the plastic parameters needed in any given elastic-plastic constitutive model to simulate the performance of structures with elastic-plastic components.

Chapter
FIVE

Fracture simulations

5.1 Introduction

The ultimate purpose of this research project is to investigate the fragility of porous ceramic pellets under complex stress conditions due to the contact interactions between pellets in a container. In this chapter, the Solidity FEMDEM code has been used to first investigate its capabilities in the simulation of fragmentation of porous ceramic specimens, and then to investigate the structural strength of complex-shaped pellets under simplified loading conditions. As pointed out in previous chapters, it is important to recognise that cohesive zone joint element implementations in FEMDEM codes have rarely, if at all, been applied to the modelling of fracture and fragmentation for any materials other than geomaterials. The challenges of obtaining suitable material properties to perform such simulations on porous ceramics were presented in Chapter 2. Here, the focus is on proving through a series of validation

studies that the method can also be applied to fracture of very strong (by comparison with most geomaterials) porous ceramic bodies, ones that could be designed to take on any shape suitable to deliver advantages for the catalyst performance. The chapter therefore follows a progression from simple specimen geometry strength tests towards more complex shape specimens, leaving the reader to infer that given quite complex shapes sometimes resulting in mixed mode failures have been simulated to an unprecedented accuracy, that the same methods will handle fracturing in arbitrarily complex loadings and shapes as the stresses would be captured in just the same way.

5.2 Three-point bending test simulation

As illustrated in the previous chapter, the three-point bending test consists of placing a specimen on two supports and applying a vertical load in the middle of the two supports by means of a punch. The apparatus in Figure 5.1(a) was used for the experiments. A metal support with a 20 mm span is fixed to a steel cylinder. The punch is a steel cross-head instrumented with a load cell and attached to an actuator. The experiment is executed in displacement control, with a cross-head velocity of 0.5 mm/min or 0.0000084m/s

The three-point bending apparatus was mounted on actuators of different size, depending on the velocity of the test. The testing machine can record forces and displacements during the experiment. A second data logger is connected to the force transducer that has been fixed on the cross-head. This makes it possible to record the force at a higher frequency and to have a more consistent set of measurements, for example when the experiment is performed with different actuators. The experiment was also recorded with a high-speed camera, which enables the correction of errors in the force-deflection curve resulting from possible rig compliances

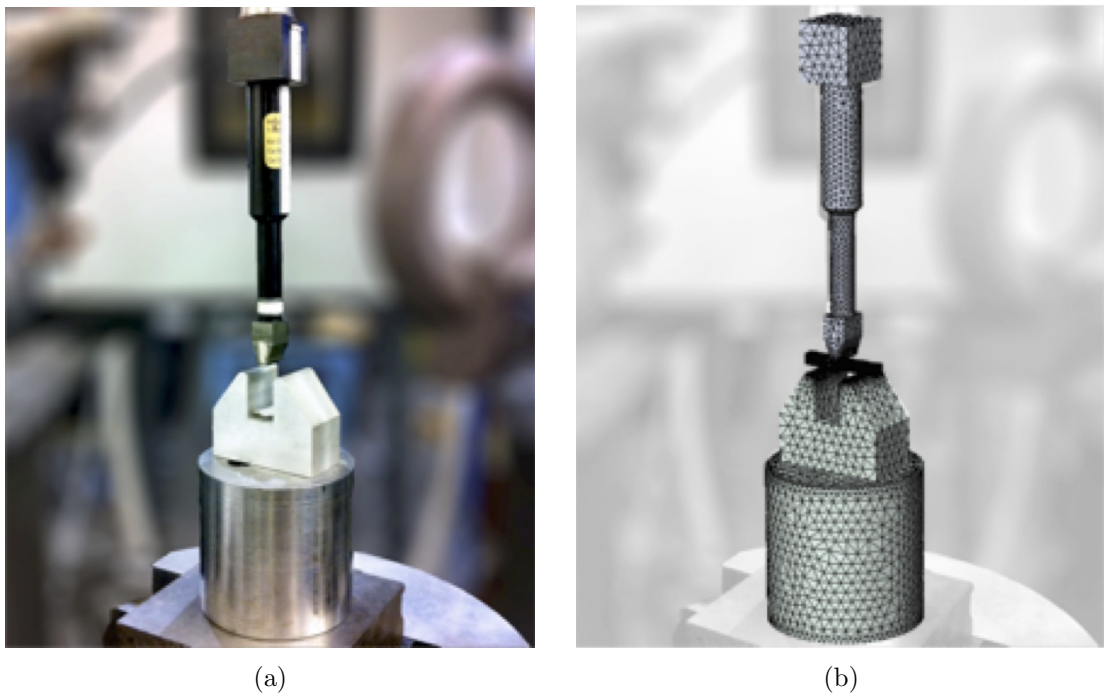


Figure 5.1: (a) Photograph of the real three-point flexural test apparatus and (b) tetrahedral mesh for the case of a 3D numerical simulation.

and localised plastic deformation at the points of contact. The high-speed video was also employed to determine the fracture path and velocity of the fragments.

The experiment has been modelled with 2D and 3D FEMDEM simulations. In this chapter only the 2D simulation results are presented. The boundary conditions and the 2D triangular mesh are illustrated in Figure 5.12. The top of the punch is constrained with constant velocity. To reduce the run time of the numerical simulation, the velocity of the constraint is set to 0.01 m/s. Although this loading rate is higher than the one in the laboratory experiment, it induces a quasi-static response in the bar as there is no significant difference between the force applied by the punch and the one applied by the two constraints. To further reduce the calculation time, when the simulation starts, the punch is in contact with the specimen and for this reason an initial velocity equal to the one applied to the constraint is imposed to the whole punch. The discretisation of the punch and constraints is refined only

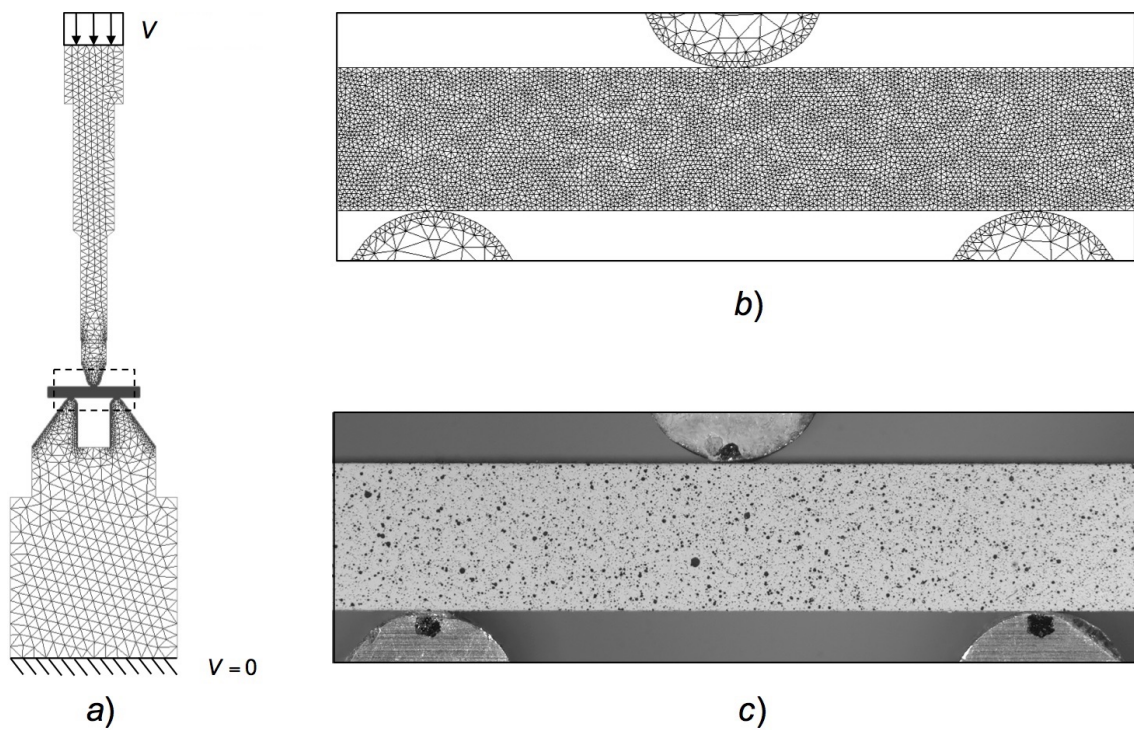


Figure 5.2: (a) Boundary conditions for the three-point flexural experiment and triangular mesh of its 2D numerical simulation. (b) Detail of the specimen discretisation and c) corresponding frame from the high-speed video.

where the contact occurs so as to better represent the geometry of their contours without considerably increasing the computational burden. Since fractures are only allowed within the joint elements, the specimen is discretised with an unstructured fine mesh to better represent both the de-bonding stress during the opening of the crack and the fracture path along the element boundaries. The total number of elements employed in the model is around 20,000. The material properties used to describe the three-point bending apparatus are $E_s=210$ GPa, $\nu_s=0.3$ and $\rho_s=7850$ kg/m², where E_s is the Young's modulus, ν_s is the Poisson's ratio and ρ_s is the density. The material properties used for the specimens vary depending on the porosity of the tested sample. Figure 5.3 shows the simulation results of a bar from Set 1, with $E_c=71.67$ GPa, $\nu_c=0.17$, $\rho_c=2580$ kg/m², $f_t=78.1$ MPa and $G_I=11$ J/m² (values of G_I for similar porous alumina samples have been reported in the literature [Lam *et al.* (1994)]). The frictional interaction between the rig supports and the alumina sample is modelled using a Coulomb coefficient of friction equal to 0.01.

The mean and horizontal stress fields in the apparatus and in the tested specimen respectively at different time lapses are reported in Figure 5.3. The simulated stress field in the bar sample before failure agrees with the theoretical predictions of Euler-Bernoulli beam theory. Equation (5.1) represents the relation between load and the horizontal stresses experienced by the material point between the two supports in the bottom side of the beam before failure. In Figure 5.5 this analytical solution is compared with the horizontal stress calculated in the corresponding FEMDEM simulation. In accordance with the analytical solution, the horizontal stress that has been extrapolated from the simulation increases linearly until it reaches the value of the tensile strength (78 MPa) and then, when the fracture starts to propagate, it drops to zero. The numerical model slightly overestimates the displacements (and thus underestimates the stiffness) due to the joint element discretisation Lorentz (2008). This leads to a slightly lower gradient for the numerical curve in Figure 5.5

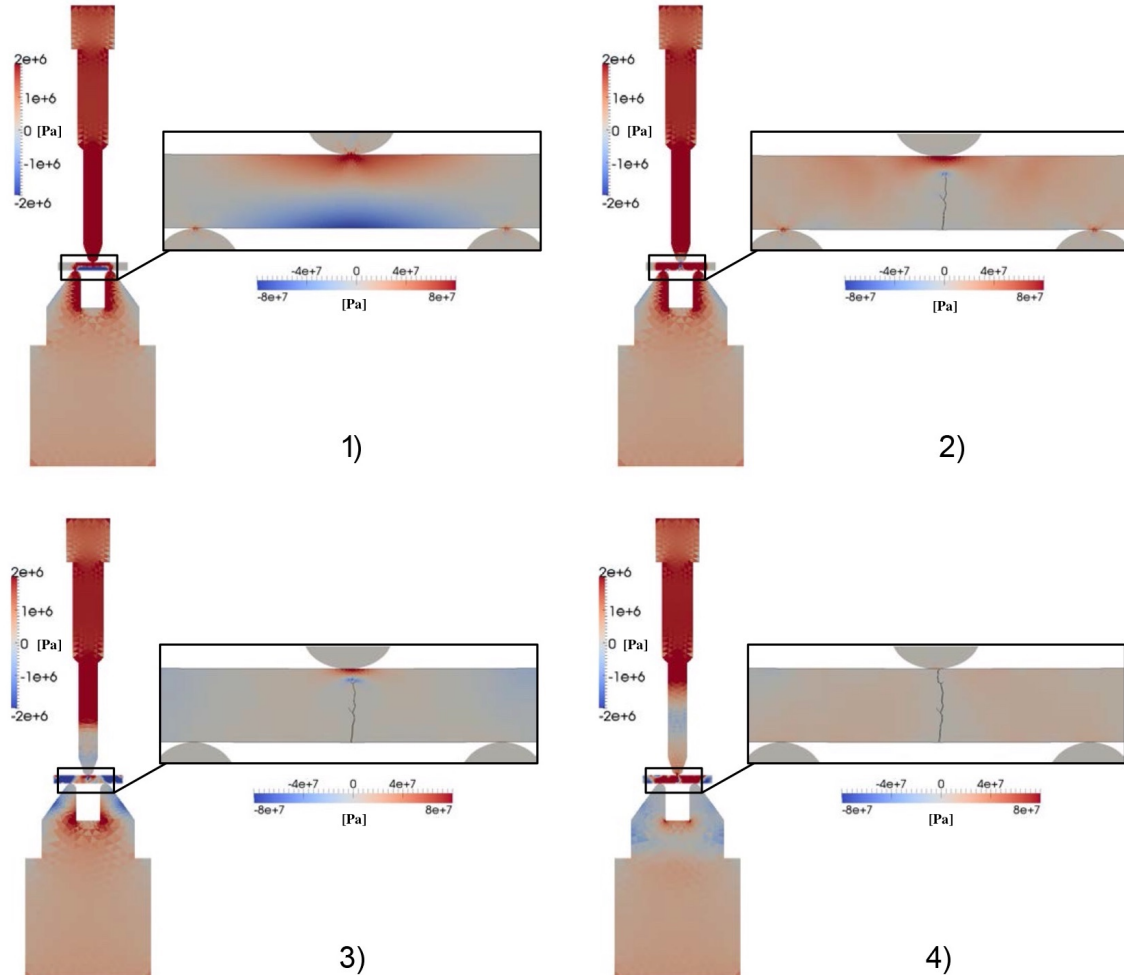


Figure 5.3: Stress field in a 2D numerical model showing a crack propagating at different times during a three-point flexural test: the mean stress for each time lapse is shown on the image of the apparatus on the left and the horizontal stress is shown on the magnified beam on the right.

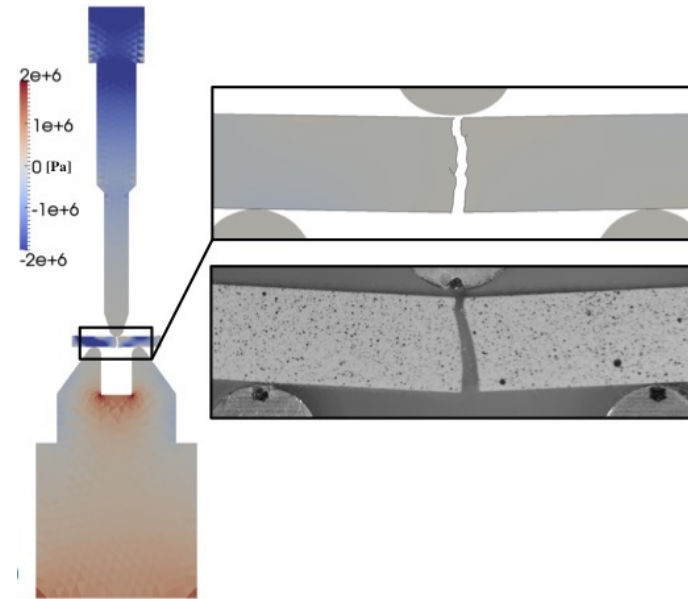


Figure 5.4: Comparison between the model of the specimen after failure in the 2D numerical simulation and a frame from the high-speed video recording of the actual experiment.

and an overestimation of the simulated bending profile, as shown in Figure 5.7. This aspect relating to the potential for a numerically induced slightly reduced stiffness being caused by the use of discontinuous joint elements needed to capture fracture paths will be discussed in Section 5.3 in more detail. In Figure 5.6 the load-deflection curve calculated in the numerical simulation is compared with the experimental results. The maximum value for the contact force is slightly higher in the numerical results than in the theoretical prediction. This can be caused by the mesh elements not being perfectly aligned across the vertical plane where the stress field develops its maximum tension. The fracture path produced in the numerical simulations is close to the one observed in the experiments as shown in Figure 5.4.

$$\sigma_h = \frac{3s}{2H^3}F \quad (5.1)$$

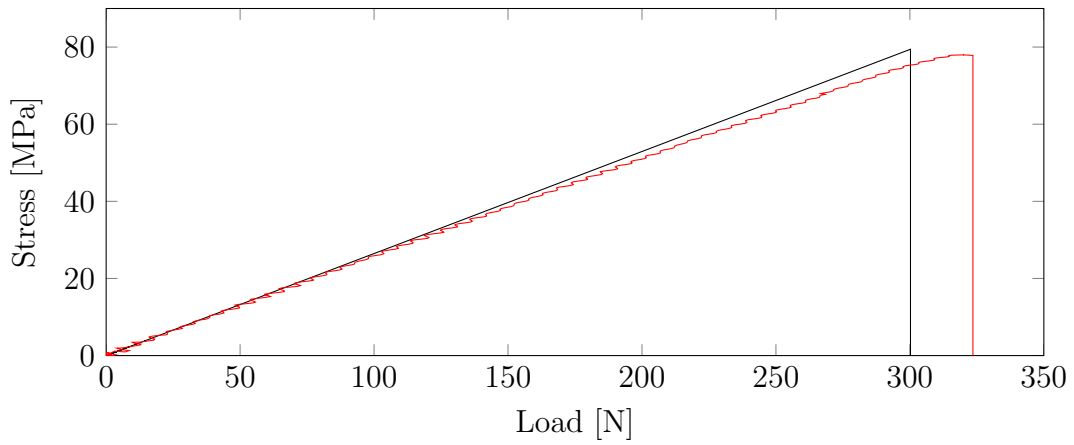


Figure 5.5: Comparison of the applied load and the horizontal stress experienced by the material point as sampled centrally between the two supports just within the bottom side of the beam in the 2D numerical model (red) and in the corresponding analytical solution (black).

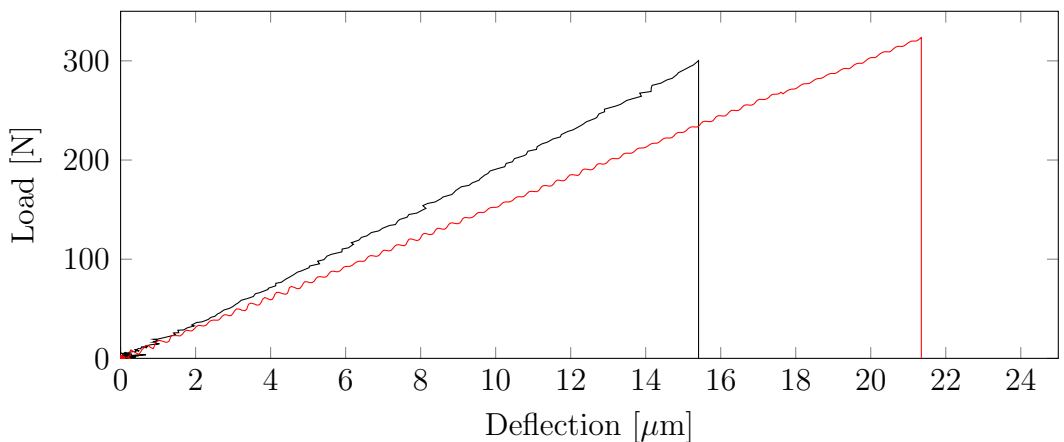


Figure 5.6: Comparison of the load-deflection curve calculated in the numerical simulation (red) and obtained from a test on a bar from Set 1 (black).

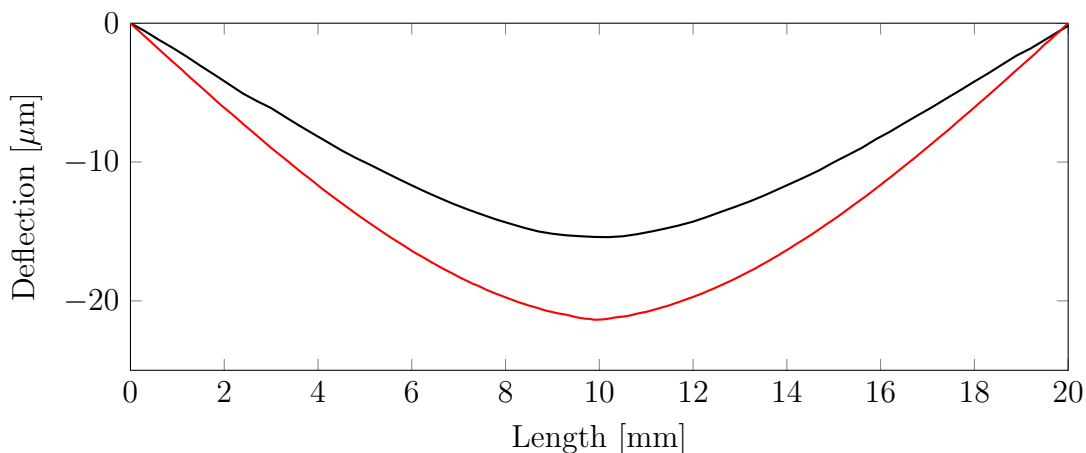


Figure 5.7: Comparison of the deflection profile calculated in the numerical simulation (red) and obtained from a test on a bar from Set 1 (black).

5.2.1 Uniaxial compression simulations

The uniaxial compression test apparatus was mounted an actuators to apply a uniaxial load, as described in the previous sections. The loading plates and the tested samples have been modelled with 2D simulations. Both tests and simulations have been performed on discs with and without holes, the mesh and boundary conditions are shown in Figure 5.8(a) and 5.11 respectively. The experiment was also recorded with a high-speed camera to determine the fracture path and velocity of the fragments. The top loading plate is constrained with constant velocity. The velocity of the constraint is set to 0.01 m/s, which is the loading rate that was set in the laboratory experiments. To reduce the calculation time, when the simulation starts, the top plate is in contact with the specimen and for this reason an initial velocity equal to the one applied to the constraint is imposed on the loading plate. The specimen is discretised with an unstructured fine mesh to correctly represent both the de-bonding stress during the opening of the crack and the fracture path along the element boundaries. The total number of elements employed in the simulations of discs with and without holes is about 37,000 and 53,000 respectively. The material properties used to describe the loading plates are $E_s=210$ GPa, $\nu_s=0.3$ and

$\rho_s=7850 \text{ kg/m}^2$, where E_s is the Young's modulus, ν_s is the Poisson's ratio and ρ_s is the density. The material properties used for the specimens vary depending on the porosity of the tested sample. Figure 5.8 shows the simulation results of a disc with no holes from Set 1, with $E_c=40.05 \text{ GPa}$, $\nu_c=0.17$, $\rho_c=2310 \text{ kg/m}^2$, $f_t=50.7 \text{ MPa}$ and $G_I=0.2 \text{ J/m}^2$. The strength and stiffness of the prismatic samples were reasonably aligned with values of energy release rate for the three sets of bars were available in the literature [Lam *et al.* (1994)]. Since a value of fracture toughness was not available for the cylindrical samples (the different tools employed for the sintering of these pellets generated weaker sets of specimens compared to the sets of prismatic bars), in this case values G_I have been optimised for the three sets of sample to obtain the correct failure mechanism for the uniaxial compression of a disc. In other words G_I have been selected from the simulation showing a fracture initiating from the centre of the disc and propagating to the two contact points. The same values of energy release rate have been used for the simulations of uniaxial compression of pellets with four holes.

The interaction between the steel and the alumina sample is modelled using a Coulomb coefficient of friction equal to 0.01. Figure 5.8(b) shows the horizontal stresses reaching the value of tensile stress (red) in the centre of the disc before failure. After that point, a fracture initiates from the centre and propagates diametrically to the two points of contacts, as shown in Figure 5.8(c). While the fracture reaches the two points of contact, also the applied load drastically decreases and the two halves of the disc fragment under the action of the two loading plates as shown in Figure 5.8(d). The simulation results can be compared with two frames obtained from the high-speed video recordings of the test of a disc with no holes from Set 1 shown in Figure 5.8(e) and 5.8(f). Assuming an elastic response of the disc and that the applied load is transmitted by each loading plate on a flat $200 \mu\text{m}$ portion of the disc surface ($\alpha = 0.6^\circ$), an approximate solution for the relation between the

plate displacement and applied load during the test can be defined in equation (5.2) [Wang *et al.* (2004)].

$$d = -\frac{2P}{\pi E t} \left[(1 - \mu) - \log \left(1 + \frac{4}{\sin^2(\alpha)} \right) \right] \frac{\alpha}{\sin(\alpha)} \quad (5.2)$$

In Figure 5.9 the load-displacement curve calculated in the numerical simulation is compared with the approximated experimental curve. The maximum value for the contact force is slightly higher in the numerical results than in the theoretical prediction. This could be because the mesh elements are not all perfectly aligned across the vertical plane where the stress field develops its maximum tension.

Numerical simulations of the uniaxial compression tests on the disc with four holes have been carried out loading the specimens in different orientations, i.e. with respect to the angles between the line of the contact points and the symmetry axes of the discs created by the four hole locations. When the two hole centres lie directly in line with the loading points, this is the weak orientation. Loading orientations at intervals of 5° have been considered between the weak (0°) and the strong (45°) orientation configuration of the four-hole disc. Figure 5.10 shows the load-displacement curves obtained from uniaxial compressive test simulations on the four-hole specimens from Set 1. The load that makes the first fracture initiating within the pellet (i.e. when the first joint element reaches breakage) is determined by inspecting the fracture walls in the numerical results. This value of load is generally a few orders of magnitude smaller than the loads related to the post-failure fragmentation process. Figure 5.11 and 5.12(a) respectively, show boundary conditions and the stresses reaching the value of tensile stress (blue) in the top right and bottom left hole. After that point, almost simultaneously, two fractures initiate and propagate towards the two points of contact with the loading plates,

and at the same time two new fractures propagate horizontally between the two top and two bottom holes. While the fracture reaches the two points of contact, also the applied load decreases and the two bigger fragments of the disc can break under the action of the two loading plates. The simulation results can be compared with two frames obtained from the high-speed video recordings of the test of a disc with four holes from Set 1 shown in Figure 5.12(b) and 5.12(c). The similarity is remarkable, consider for example the shape of the central piece broken out when the four holes are all joined by fractures as seen in the last frame.

In Figure 5.14 the load at failure calculated in the numerical simulation for the different orientations is compared with the experimental data. The values of load have been normalised with respect to the strength of an equivalent cylinder of identical geometry without holes. The load required to break the samples from Set 3 in their strong configuration exceeded the capabilities of the experimental apparatus used in this study. The numerical results are in good agreement with the experimental data and provide a relation between the loading orientation and the structural strength of the four-hole discs which is consistent between different sets of samples. The numerical results slightly overestimate the structural strength of the four-hole discs at 0° and underestimate the strength at 45° . This could be due to material inhomogeneity defects in the real sample and difficulties in the definition of a precise value of load at failure in the actual experiments.

5.3 Mesh sensitivity analysis

A mesh sensitivity analysis has been carried out for the three-point bending test simulations. The sample bar from Set 1 was discretised with four meshes with four different sizes: 1 mm , $150\text{ }\mu\text{m}$ and $100\text{ }\mu\text{m}$, as shown in Figure 5.15. The force-deflection curves calculated in the numerical simulations for the three mesh sizes

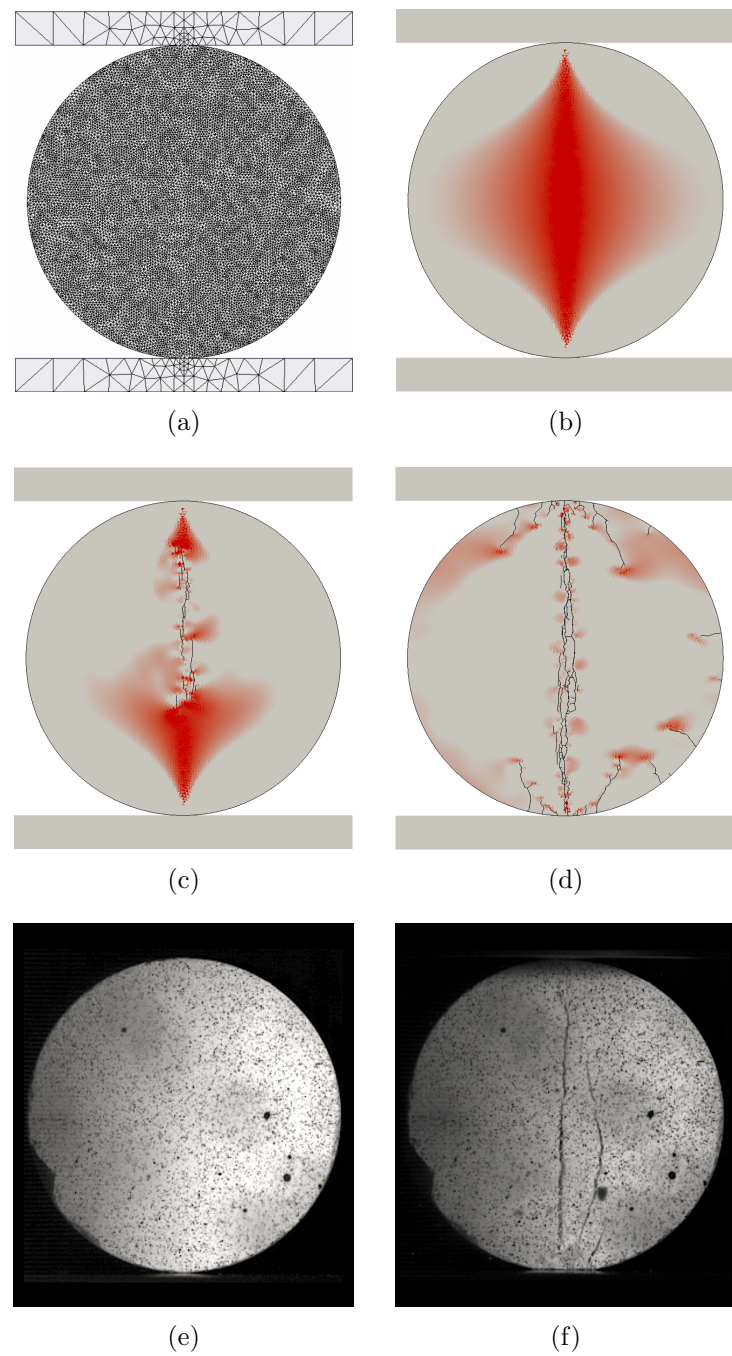


Figure 5.8: Simulation of the uniaxial compressive test on a cylinder without holes from Set 1: (a) triangular mesh discretisation of the specimen and loading plates. (b) Horizontal tensile stress field before failure reaching the value of tensile strength in the centre of the disc. (c) Crack propagating from the centre of the disc to the two sides and (d) splitting of the two sides of the disc and post failure fragmentation. Two frames from the video recording of the uniaxial compressive test on a cylinder without holes from Set 1: (e) before and (f) after failure.

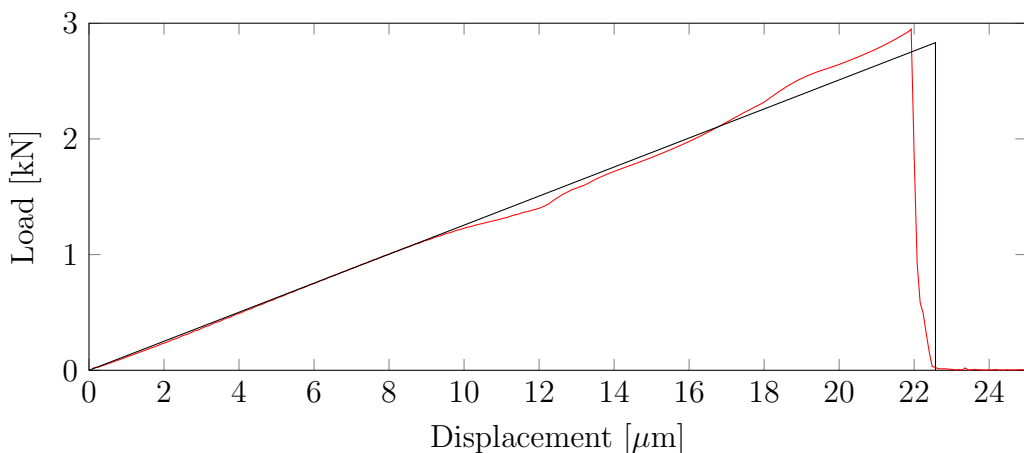


Figure 5.9: Load-displacement curve for the uniaxial compressive test on a cylinder without holes from Set 1: comparison between the numerical results (red) and the theoretical curve (black) calculated with equation (5.2).

are shown in Figure 5.16. The peak force at failure for the three simulations is consistent with the experimental value and it is relatively insensitive to the mesh size. Figure 5.16 and 5.17 show that the structural stiffness of the simulated bar is strongly sensitive to the mesh size. This is due to the fact that when the element size is reduced, the number of finite elements and joint elements is increased. Each joint element allows a certain degree of relaxation of the constraint on the relative displacements between adjacent finite element nodes and the larger the number of joint elements, the higher is the artificial compliance that they generate. This artificial compliance problem has been discussed in Lorentz (2008).

A mesh sensitivity analysis has also been carried out on the uniaxial compression test simulations. The disc without holes from Set 1 has been discretised with four different realisations of a $150 \mu\text{m}$ element size mesh (Figure 5.18) obtained with three different values for the rigid rotation about the centre of the disc. With the same process, four different realisations of a $100 \mu\text{m}$ element size mesh have also been obtained, as shown in Figure 5.19. The load-displacement curves for the four realisations of a $150 \mu\text{m}$ element size mesh are shown in Figure 5.20. Figure 5.21

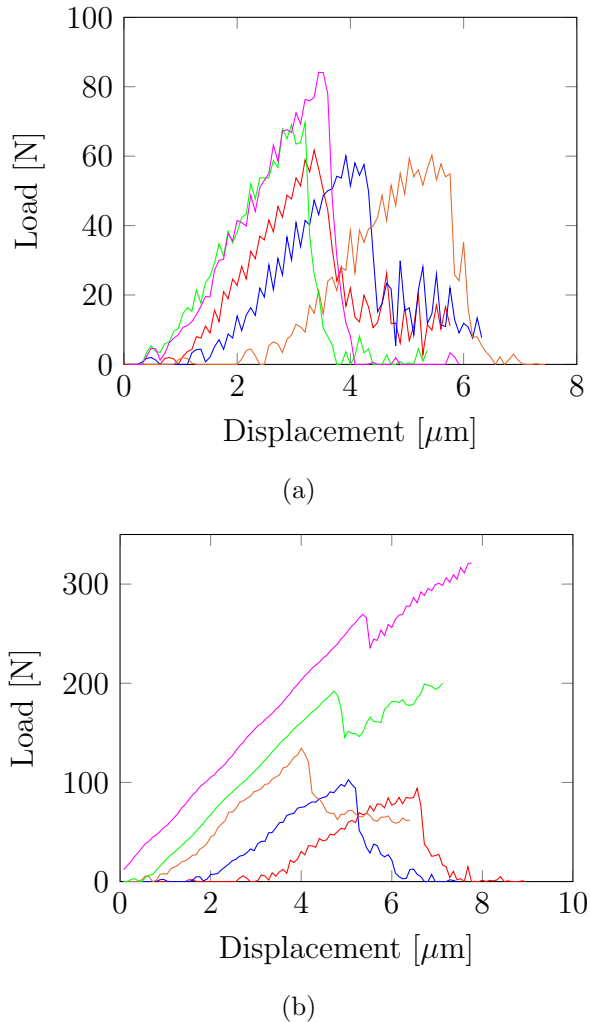


Figure 5.10: Load-displacement curves obtained from uniaxial compressive test simulations on the four-hole specimens from Set 1 for orientation angles of: (a) 0° (red), 5° (blue), 10° (orange), 15° (green), 20° (magenta) and (b) 25° (red), 30° (blue), 35° (orange), 40° (green) and 45° (magenta).

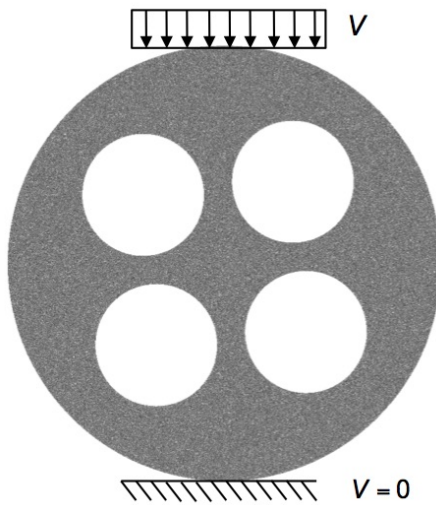


Figure 5.11: Boundary conditions for the Brazilian test of a ceramic pellet with four holes diametrically compressed against two steel plate and triangular mesh of its 2D numerical simulation.

shows the load-displacement curves for the four realisations of a $100 \mu m$ element size mesh. The initial part of the plots show the load take up with displacement is sensitive to the initial contact condition of the specimen with the two loading plates, which varies in due to the rigid rotation of the mesh. This causes small fluctuations in the load-displacement curves in Figure 5.21. The peak values of the load for the 8 realisations of the $150 \mu m$ and $100 \mu m$ element size are consistent with the theoretical peak load values also plotted in the figures, suggesting there are no significant unintended anisotropies in stiffness and strength imposed by the unstructured meshing tool employed.

5.4 Concluding remarks

The results that have been presented in Chapter 4, provided considerably more information than simply the material property parameters that were needed for the numerical simulations. The availability of full deflection profiles in which the effects

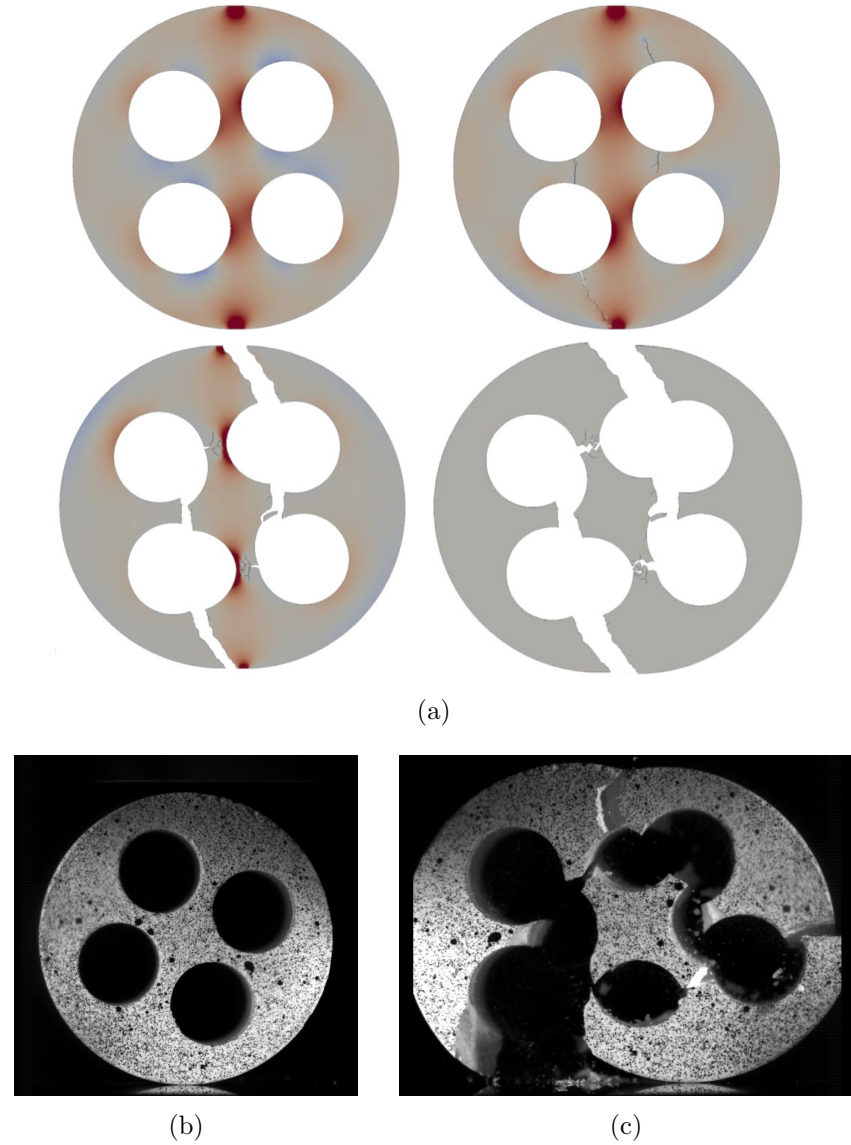


Figure 5.12: a) Time-lapse numerical results immediately before failure and after failure. Two frames from the video recording of the uniaxial compressive test on a cylinder with four holes from Set 1: (b) before and (c) after failure.

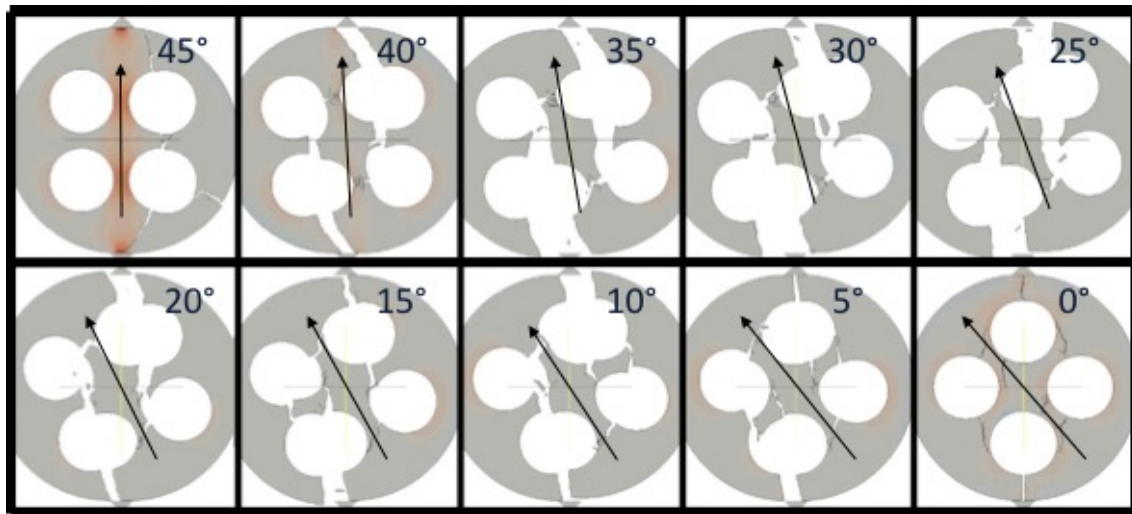


Figure 5.13: Numerical simulations of the the uniaxial compression tests on the disc with four holes loaded in different orientations.

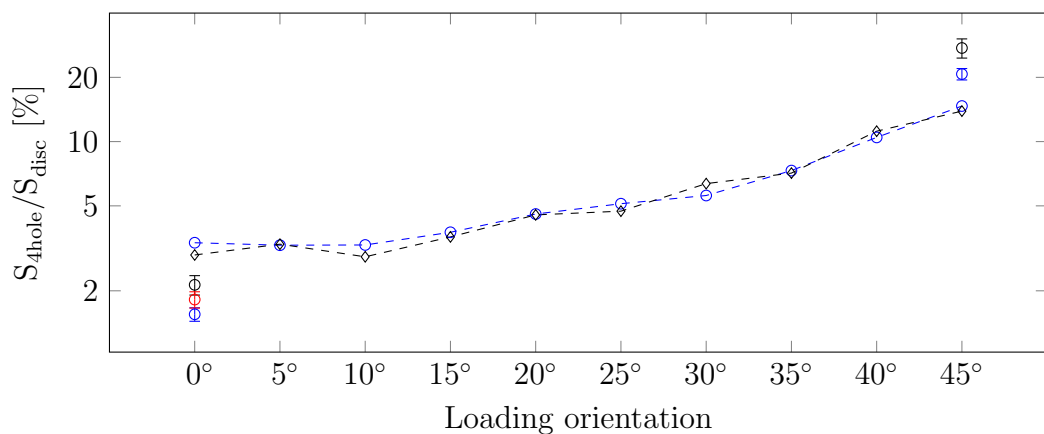


Figure 5.14: Relation between the loading orientation and the structural strength of four-hole pellets, normalised with respect to the strength of an equivalent cylinder of identical geometry without holes. Experimental (dots) and numerical (dashed lines) results for Set 1 (blue), Set 2 (black). Experimental results for the weak orientation for Set 3 (red).

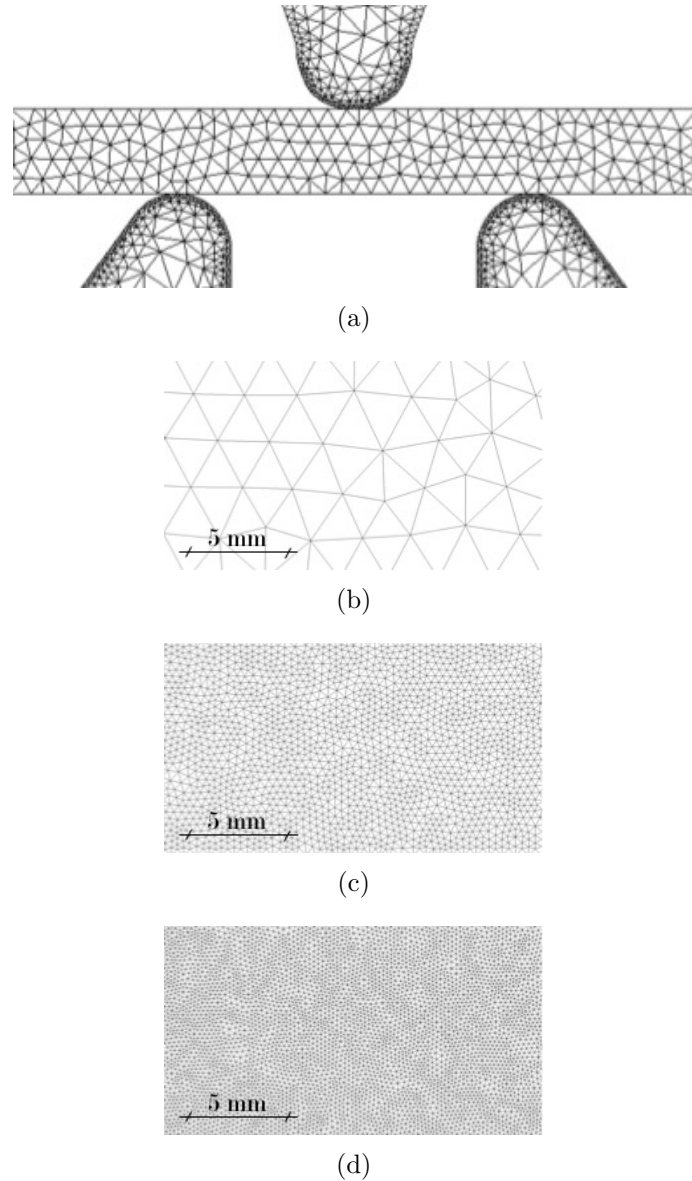


Figure 5.15: Mesh sensitivity analysis for the three-point bending test simulations:
 (a) triangular mesh discretisation of the test setup and (b) detail of the 1 mm mesh for the bar. (c) Detail of the 150 μm mesh of the bar. (d) Detail of the 100 μm mesh of the bar.

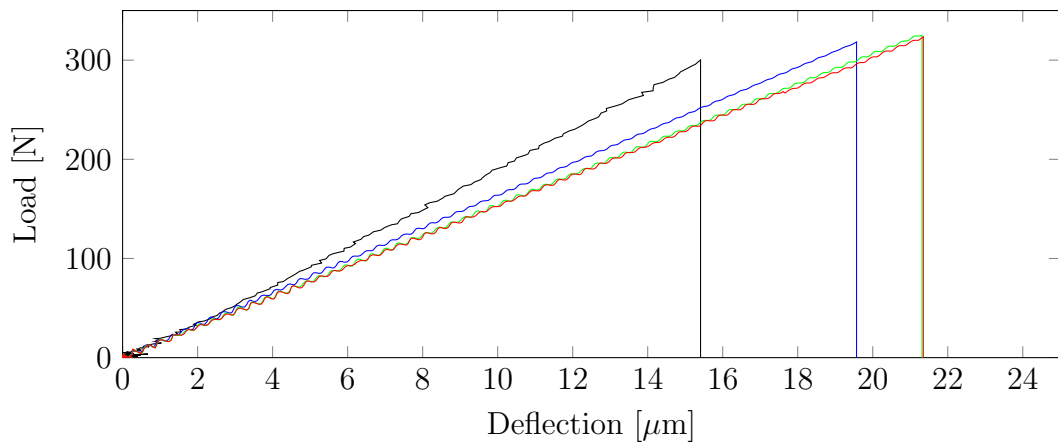


Figure 5.16: Mesh sensitivity analysis for the three-point bending test simulations: comparison of the load-deflection curve calculated in the numerical simulations for the 1 mm (blue), 150 \mu m (green), 100 \mu m (red) mesh and obtained from a test on a bar from Set 1 (black).

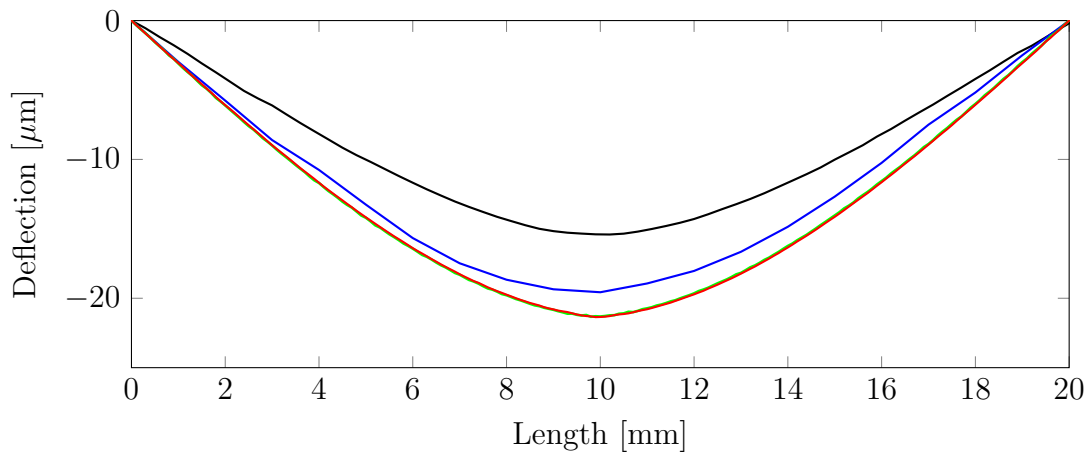


Figure 5.17: Mesh sensitivity analysis for the three-point bending test simulations: comparison of the deflection profile calculated in the numerical simulations for the 1 mm (blue), 150 \mu m (green), 100 \mu m (red) mesh and obtained from a test on a bar from Set 1 (black).

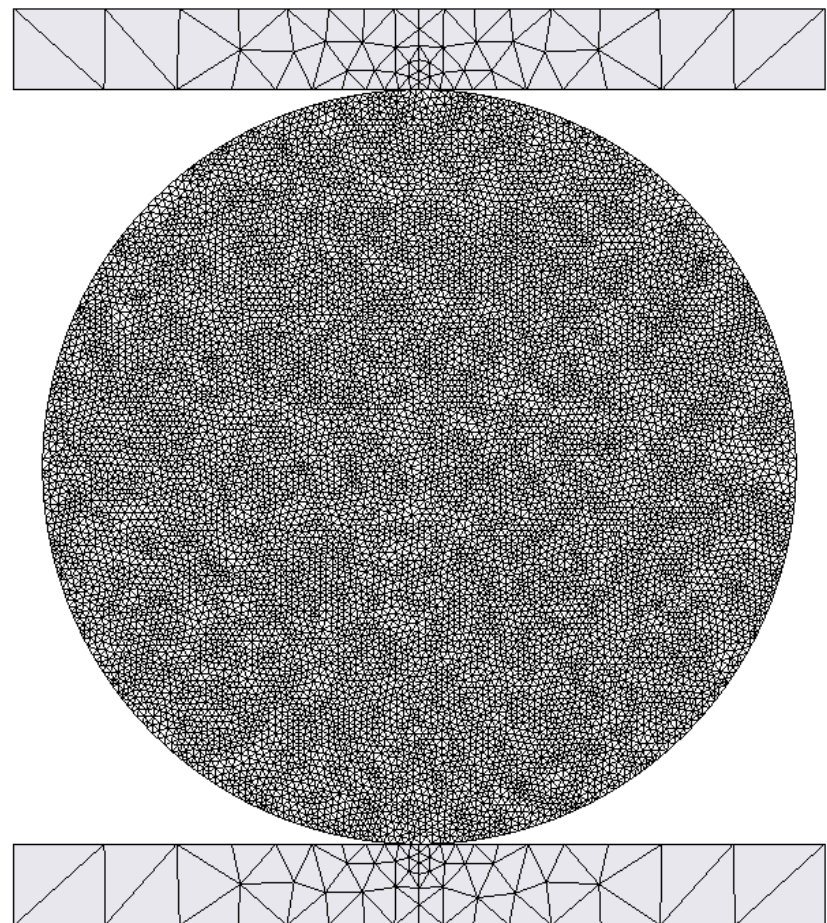


Figure 5.18: Mesh sensitivity analysis for the uniaxial compression test simulations: triangular mesh discretisation of the test setup for the $150 \mu m$ mesh. The mesh is then rotated of 10° , 20° and 30° to perform a comparison of four different mesh realisations with the same element size.

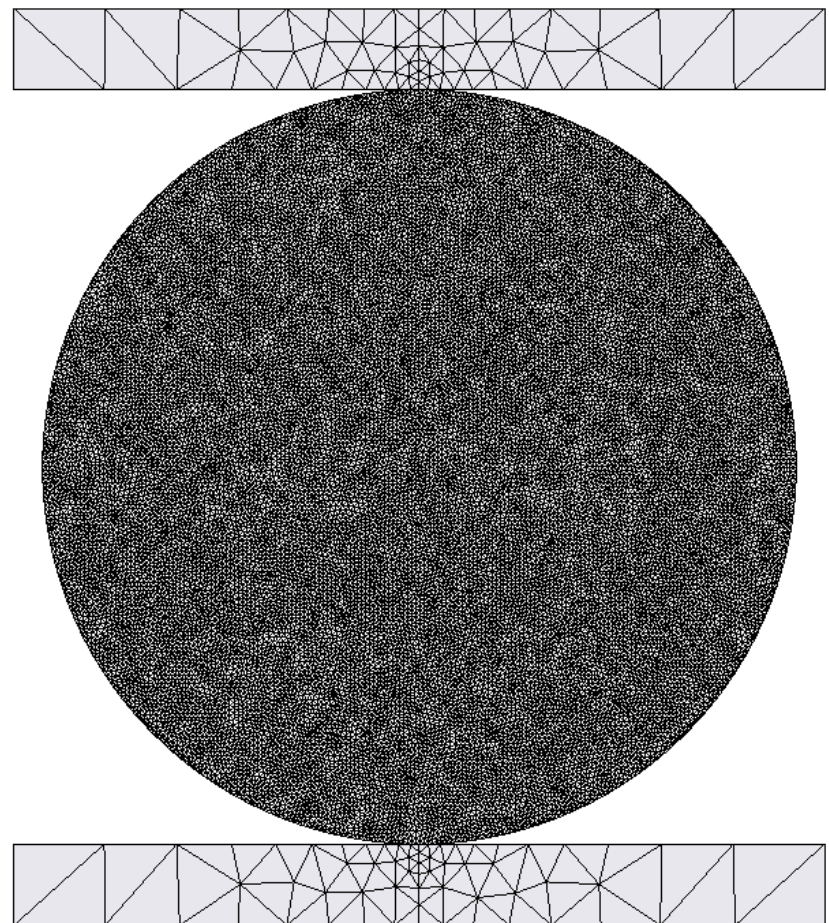


Figure 5.19: Mesh sensitivity analysis for the uniaxial compression test simulations: triangular mesh discretisation of the test setup for the $100 \mu m$ mesh. The mesh is then rotated of 10° , 20° and 30° to perform a comparison of four different mesh realisations with the same element size.

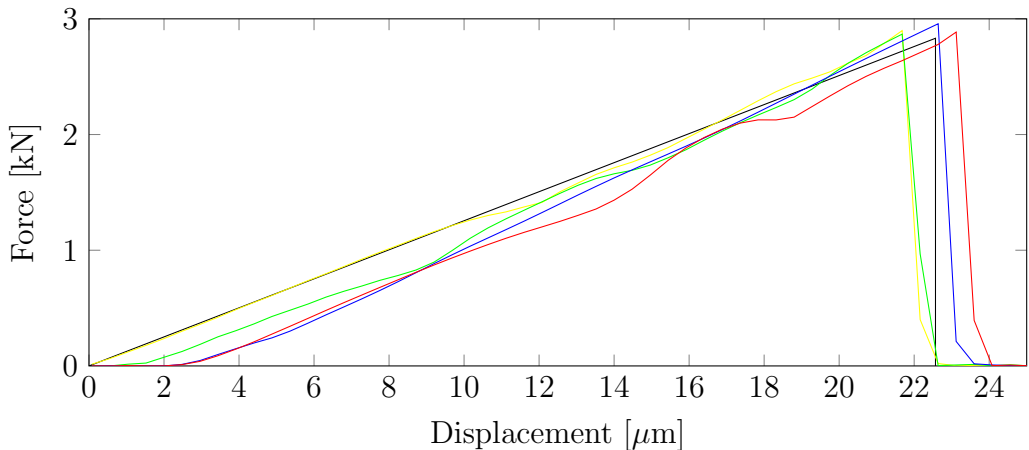


Figure 5.20: Mesh sensitivity analysis for the uniaxial compression test simulations: comparison of the load-displacement curve calculated in the numerical simulations for the $150 \mu\text{m}$ mesh obtained with 0° (yellow), 10° (green), 20° (blue) and 30° (red) rotation of the original mesh of the disc. The numerical results are compared to the theoretical curve given by the experimental results for Set 1 (black).

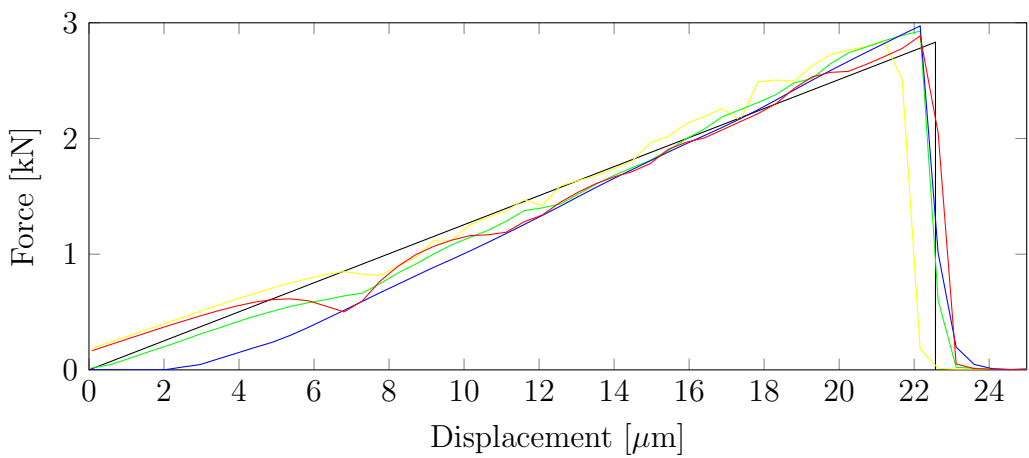


Figure 5.21: Mesh sensitivity analysis for the uniaxial compression test simulations: comparison of the load-displacement curve calculated in the numerical simulations for the $100 \mu\text{m}$ mesh obtained with 0° (yellow), 10° (green), 20° (blue) and 30° (red) rotation of the original mesh of the disc. The numerical results are compared to the theoretical curve given by the experimental results for Set 1 (black).

of the rig self-compliance and bar specimen readjustments (due to geometrical imperfections and local crushing) were corrected, offered also a great opportunity to investigate the Solidity FEMDEM code capabilities in the simulation of stiff porous ceramic specimens. Solidity, previously named VGEST (virtual geoscience simulation tools), has to date been largely used for the study of the mechanical behaviour of geomaterials [Lisjak & Grasselli (2014)]. The focus of Chapter 5 has been to provide confirmation, through a series of validation studies, that the FEMDEM method can also be applied to the simulation of fragmentation of very strong (by comparison with most geomaterials) porous ceramic bodies, ones that could be designed to take on any novel or traditional shape suitable to deliver advantages for the catalyst performance. In Chapter 3, a progression from simple specimen geometry strength tests towards more complex shape specimens was presented in the context of a validation study.

5.4.1 Three-point bending tests

In Section 5.2 results from the numerical simulations of three-point bending tests have been compared to the corresponding experimental results confirming that the simulations of mode I fracture in porous ceramic bars matches the experimental results. Some limitations of the code were identified and are worthy of further discussion.

The value of peak force is slightly higher in the numerical results than in the theoretical prediction. This is probably caused by the mesh elements not being perfectly aligned across the vertical plane where the stress field develops its maximum tension. This is a marginal issue that has not a great impact on the final results and one that can be minimised by employing an unstructured mesh.

5.4.2 Artificial compliance

Another code limitation that became very apparent from the verification work that has been presented in section 5.2 is the artificial compliance generated by the joint element discretisation. The same process that was used to generate the corrected full deflection profiles from the experimental data described in Chapter 4, have also been applied to the displacement field that was calculated in the Solidity FEMDEM simulations. This has been done to obtain comparable sets of data since the idealised three-point bending experiment reproduced in the numerical simulation is not capable of representing small specimen imperfections, local crushing near contact points and the self-compliance of the rig actuator. The results that have been presented in Section 5.3 show that the simulated structural stiffness is strongly sensitive to the mesh size. This is due to the fact that when the element size is reduced, the number of finite elements and joint elements is increased. Each joint element allows a certain degree of relaxation of the constraint on the relative displacements between adjacent finite element nodes and the larger the number of joint elements, the higher is the artificial compliance that they generate Lorentz (2008). This is a strong limitation in the applicability of the code for the simulation of these types of stiff porous ceramics. On the one hand, as shown in Section 3.1.2.4, the high strength and relatively low energy release rate require the code user to reduce the element size and in turn increase the number of joint elements. On the other hand, the large number of joint elements generate an artificial compliance in the simulated elastic behaviour that does not allow the correct representation of the actual high stiffness of the ceramic samples. New code implementations in the Solidity FEMDEM code are now under development to reduce this artificial compliance and will be discussed in Section 7.2.

5.4.3 Brazilian tests

The numerical simulation results of uniaxial compressive tests on cylinders without holes (Brazilian disc tests) have been presented in Section 5.2.1. The contact force extrapolated from the numerical simulations has been compared to the corresponding theoretical values giving further confirmations of a correct simulation of mode I fracture in porous ceramic pellets. The strength and stiffness of the prismatic samples were reasonably aligned with values of energy release rate for the porosities of the three sets of bars that were available in the literature [Lam *et al.* (1994)]. As was pointed out, since a value of fracture toughness was not available for the cylindrical samples (the different tools employed for the sintering of these pellets generated weaker sets of specimens compared to the sets of prismatic bars), in this case values G_I were optimised for the three sample sets to obtain the correct tensile initiation and failure mechanism for the uniaxial compression of a disc. For each set of samples, a series of numerical simulations with different values of G_I in the 0.01-4 J/m² range were performed. Consequently, a value of G_I was selected when the simulation was showing a fracture initiating from the centre of the disc and propagating to the two contact points. The same values of energy release rate were used for the simulations of uniaxial compression of pellets with four holes. It is important to point out that the values of G_I deduced in this way as being applicable were lower than the corresponding values obtained in the literature for a similar porous alumina sample.

5.4.4 Structural strength of complex-shaped pellets

The experimental results of the uniaxial compressive tests that were performed on the three sets of four-hole cylinders have been presented in Section 4.3.2. The experimental results give an insight into the mechanical behaviour of catalyst supports,

since they quantify the structural strength of these type of pellets for two loading configurations (weak and the strong orientation of the holes). Even though, as it has been pointed out, limitations in the experimental apparatus did not allow sufficiently accurate results to be obtained for the strongest set of pellets (Set 3), the results from the other two sets of samples have shown a quite consistent relation between loading orientation, tensile strength and the structural strength of the pellets. When normalising the load at failure with the failure load of an equivalent cylinder of identical tensile strength and geometry but without holes, all the results converged to a value of about 2% for the weak orientation and about 20% for the strong orientation. As previously pointed out, the load values at failure could have been affected by errors as the examination of the video recordings of the tests was required to define the time when the first fracture was visible on the samples, which might have occurred later than when that fracture was actually initiated.

The structural strength of complex-shaped pellets under simplified loading conditions was investigated also with numerical simulations and the results have been presented in Section 5.2.1. Loading orientations at intervals of 5° have been considered between the weak (0°) and the strong (45°) orientation configuration of the four-hole discs. The load at failure calculated in the numerical simulation for the different orientations have been compared with the experimental data. The values of load normalised with respect to the strength of an equivalent cylinder of identical geometry without holes not only have been shown to be in good agreement with the experimental data for the weak and strong orientations, but also provide a relation between the loading orientation and the structural strength of four-hole discs which is consistent between different sets of samples. As previously pointed out, the reason why the numerical results slightly overestimate the structural strength of the four-hole specimens at 0° and underestimate the strength at 45° might be due to difficulties in the definition of the experimental failure loads and material

inhomogeneity defects in the real samples.

Apart from the structural strength of catalyst supports, other interesting insights can be obtained from the Solidity FEMDEM numerical results. These include the capability of extracting the fragment size distribution from the simulated crushed pellets leading to the characterisation of the post-failure behaviour associated with a certain shape. Future research can be undertaken to determine numerically the tendency of a certain shaped catalyst support to break into fine or bigger fragments which could be of industrial interest by contributing to pressure drop prediction and improvements in the performance of catalysts.

As shown in Section 3.1.2.5, the Solidity FEMDEM code can also simulate shear failure and given the complex shapes and loading conditions, it should not be assumed that the compressions of pellets would not result also in different modes of failure initiation i.e. both shear, tensile and mixed fracture. Since only Mode I parameters were characterised (with the generally accepted assumption that ceramics fail mostly in tension) shear failure was not taken into account in the presented simulations. Future research on microstructure and its representation in simulating failure with FEMDEM could be carried out to study the alternative modes of failure of the samples and will be discussed in Section 7.2.

Turning now to dynamic fracture, the results that have been presented in Chapter 5 have only described quasi-static loading conditions. Catalyst supports could also experience dynamic loads, for instance during the pouring process, when the pellets are deposited inside the reactor. Preliminary investigations of the Solidity FEMDEM code capabilities in the description of pellet fragmentation due to dynamic loads have also been conducted though not reported in Chapter 3 and these have given first confirmations of the applicability of the code. Indeed this is known to be one of the strengths of the FEMDEM method and will be discussed in Section 7.2.

Chapter
SIX

Packing simulations

6.1 Introduction

As stated earlier, the ultimate purpose of this research project is to investigate the fragility of porous ceramic pellets under complex stress conditions due to the contact interactions between pellets in a container. In the previous Chapter it has been shown how Solidity FEMDEM simulations can be employed for the evaluation of the structural strength of catalyst support for simplified loading conditions, to study ways to improve their mechanical performance and ideally reduce the number of fine fragments at failure. The optimisation that designers seek is complex and although finer broken fragments increase surface area for catalytic reaction, they reduce bulk permeability which is detrimental overall. The aim of simulation must therefore be to create highly accurate descriptions of the void geometry for further CFD and heat flow modelling, as well as to represent more realistic loading conditions

that can lead to the crushing of catalyst supports. The capabilities of the Solidity FEMDEM code for the simulation of packed structures of catalysts in fixed-bed reactors therefore need to be assessed for both the creation of the void topology associated with the solid skeleton and the accurate creation of contact loading on individual pellets. In either case, the problem begins with simulating the packing of pellets. The packing of solid cylindrical bodies in a cylindrical container has been approached with numerous computational techniques in the literature. In Caulkin *et al.* (2008) the packing process is simulated with both a semi-stochastic approach, where the particle path is randomly determined on the basis of the overlapping of voxels (DigiCGP), and a deterministic approach, where the repulsive forces and torques applied to the particles are calculated by measuring the number of their overlapping voxels and their voxel-level contact forces (DigiDEM).

In this context, a validation study of Solidity FEMDEM simulations is presented in this chapter where the focus is on reproducing experimental packing results when pellets are released into cylindrical containers. Solid cylindrical, spherical and complex-shaped (trilobes) catalyst supports once at-rest in their cylindrical containers are compared to the corresponding experimental results from X-Ray CT scans. The geometries of cylindrical catalyst support (A38) and their corresponding cylindrical container refer to Caulkin *et al.* (2015), whereas the geometries of the spheres, trilobes and their corresponding container refer to Nguyen *et al.* (2005). All the geometries have been imported from CAD drawings. The geometries of complex-shaped bodies and the container itself can be discretised with a tetrahedral mesh, as shown in Figure 6.1 and 6.2. As seen in Section 3.1.2.2 and 3.1.2.5 the contact forces are calculated with a penalty method and a Coulomb model of friction. The energy loss during the impacts is modelled with a damping force proportional to the particle velocity during the impact.

The particles are introduced in the domain above the container base with random



Figure 6.1: Numerical discretisation of the cylindrical container using the geometry from the experiments presented in Caulkin *et al.* (2015).

orientations and zero initial velocity. This process is completely automated through POSITIT, a pre-processing tool that facilitates the control of filling conditions and avoids the need for a manually defined 3D space for the initial conditions of each single pellet. The history of particle entry and coalescence (e.g. entry rate and velocity) can influence the final pack in terms of spacing and the randomness of the orientation. This will be discussed later in this chapter. The simulation runs in parallel on ten cores in less than twenty-four hours. The numerical results are then analysed with a post-processing tool (PORO) to estimate the axial and radial packing density profiles and the pellet orientation distribution. These post-processing tools are described in the following Sections. The state-of-rest can also be easily visualised and scrutinised with remarkable detail. In Figures 6.3, Paraview has been used to show the entire pack and a window into the details, where the complexity of the pellet geometry and its resulting pack derived from the FEMDEM solver appears to be only limited by CAD description and mesh resolution.

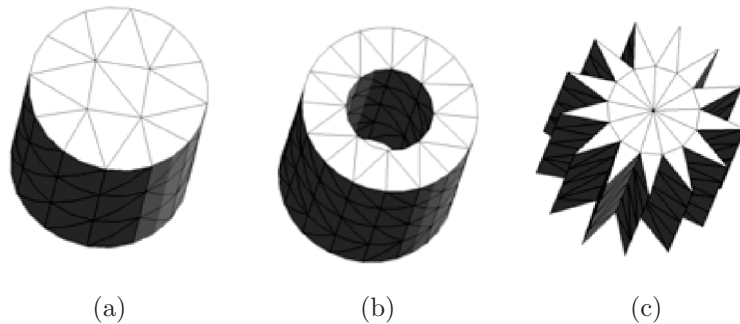


Figure 6.2: Numerical discretisation of a) the solid simple cylindrical pellet named A38 as used in Caulkin *et al.* (2015), b) a cylindrical pellet with one hole and c) a tridecagram-shaped pellet.

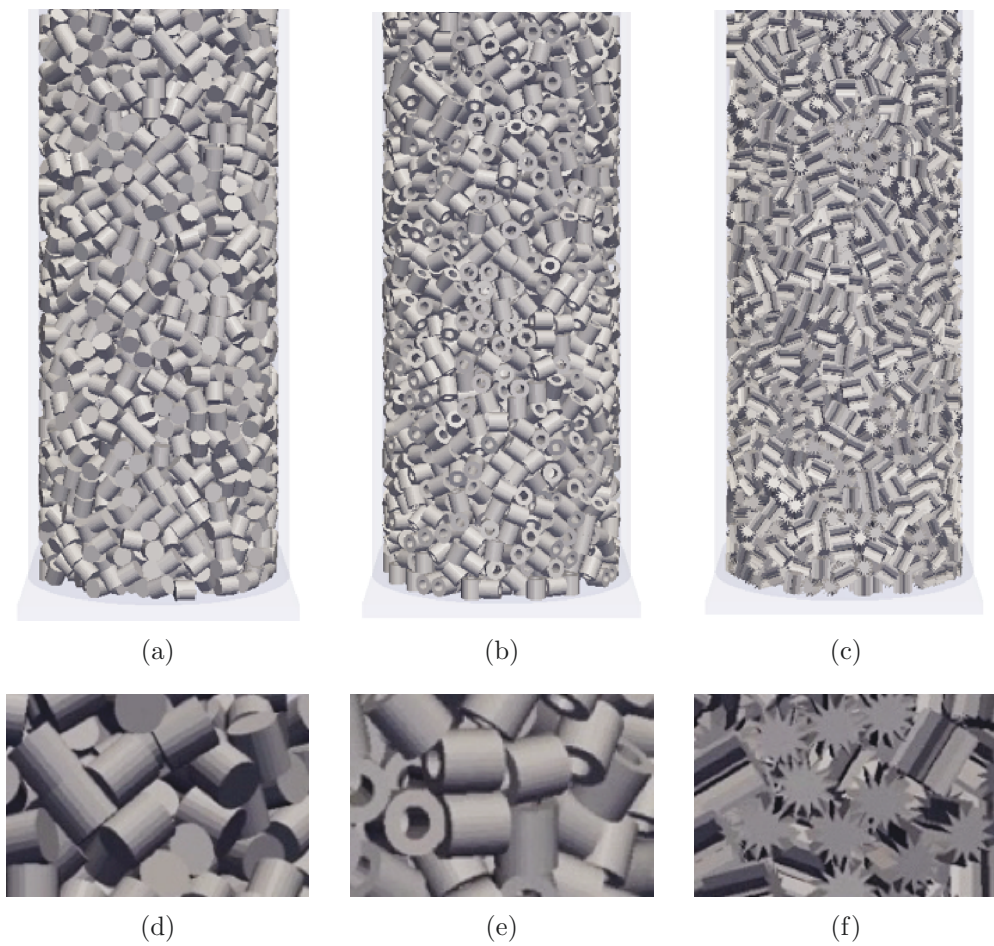


Figure 6.3: Final simulated packing structures for the three particle geometries; details of the pack of a,d) A38 cylinders, b,e) one-hole cylinders and c,f) tridecagram-shaped pellets

6.2 Axial and radial packing density profiles

The numerical results are analysed with Poro, a post-processing tool that has been specifically developed to reproduce the calculation process employed to evaluate the axial and radial packing density profiles and the pellet orientation distribution from the voxelised data format of the X-Ray CT scans that has been employed in Caulkin *et al.* (2015) and Nguyen *et al.* (2005). A regular grid to generate an equivalent voxel structure is defined in the domain of the numerical results. A value of 1 is assigned to the centroid of the voxel cells that are inside a tetrahedron of the solid mesh and 0 is assigned otherwise. For the sake of clarity, in Figure 6.4 the cell dimension is shown here to be similar to the dimension of the pellets. The real cell dimension chosen for the calculations is less than one tenth of the elements size, allowing a more precise discretisation of the packing density. The binary values of each cell is then summed and averaged within each horizontal plane from bottom to top to calculate the axial packing density profile, as shown in Figure 6.5(a) and 6.5(b). The cells are then averaged along columns to obtain a planar profile of the average packing density perpendicular to the axis of the container as shown in Figure 6.5(c). The values on the plane are then averaged along concentric rings to calculate the radial packing density profile, as illustrated in Figure 6.5(d), from concentric halos of equal areas.

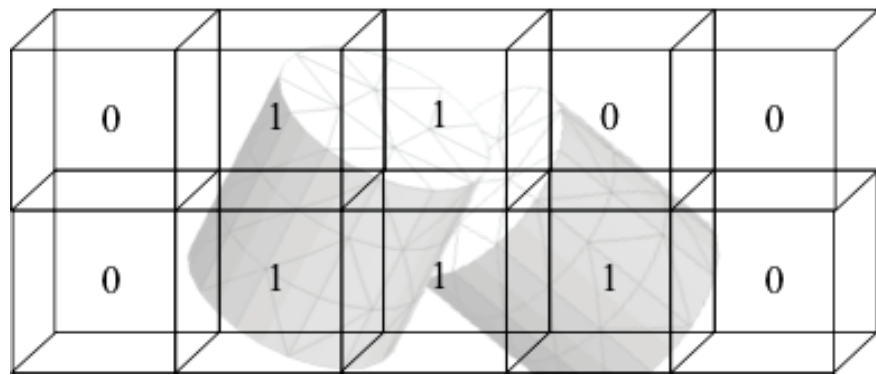


Figure 6.4: Representation of the regular grid in the domain of the numerical results. Note, a much finer voxel size is actually used to calculate the solid volume fraction in each slice.

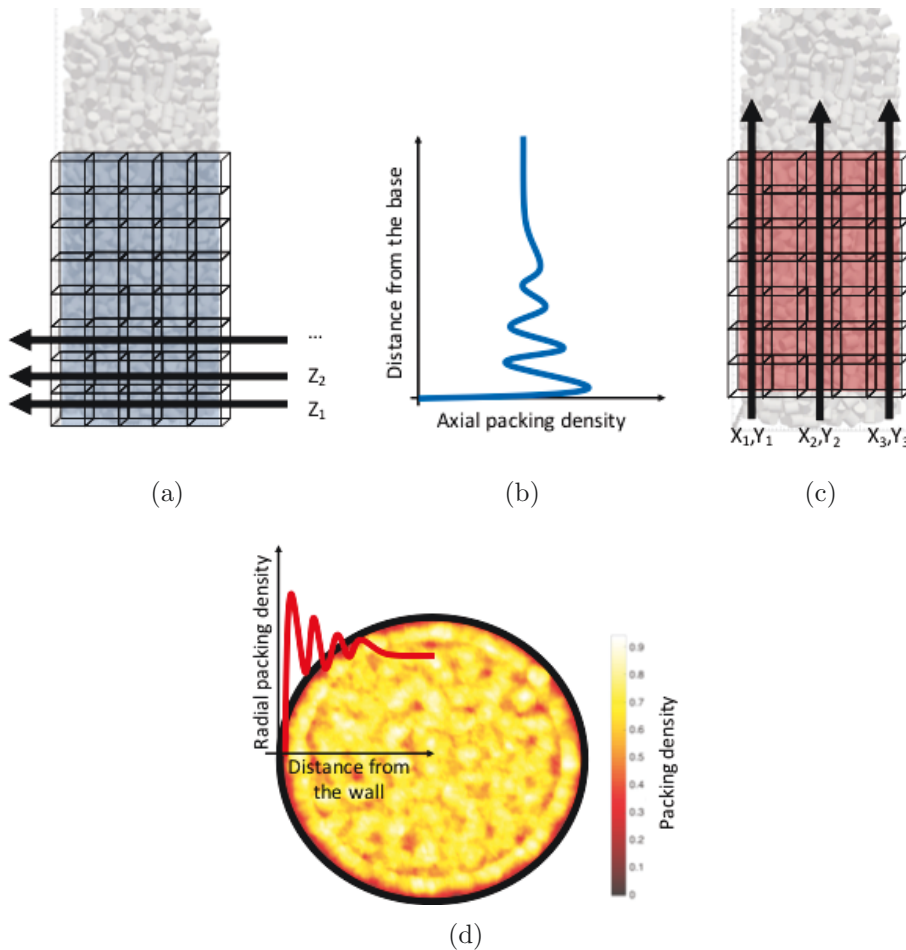


Figure 6.5: a) Averaging the values of cells along horizontal planes; b) axial packing density profile, c) averaging the values of cells along vertical columns; d) visualisation of the simulated average packing density as if observed perpendicular to the axis of the container together with superimposed radial packing density profile showing periodic wall effect as also seen in the visualisation.

6.3 Vertical orientation distributions and stereographic projections

The coordinates of the axis of each pellet are calculated using the inertia tensor of the bodies that are calculated to compute the rotational effects of contact forces

in the rigid Solidity FEMDEM simulations. This data set is exported at the end of the simulation to further characterise the packed structure. In particular, the angle between the axis of the catalyst support and the axis of the container (Figure 6.6(a)) is employed to generate statistics of the pellet orientations distributions that are then compared with the corresponding data from the X-Ray CT scans from Caulkin *et al.* (2015). Lambert Equal Area lower hemispherical projections are generally used for presenting three-dimensional information on a two-dimensional plot. Stereographic projections are commonly employed in structural geology and geotechnical engineering applications [Lisle & Leyshon (2004)], but they have been used also for assessing randomness and clustering of orientations of symmetry axes of concrete armour units within breakwater armour layers [Latham *et al.* (2013)] and pharmaceutical tablets [Ketterhagen (2011)] orientation representation. Visual representation of the relationships between the angles of crystals are also provided by stereographic projections [Smallman (1969)]. In Figure 6.6(b) the equatorial reference frame represents the plane of the container base and the plotted pellet orientations are illustrated as they would appear from a top view. In Figure 6.6(c) the stereographic projection for the orientations of a simulated cylindrical catalyst support packed structure has been shown.

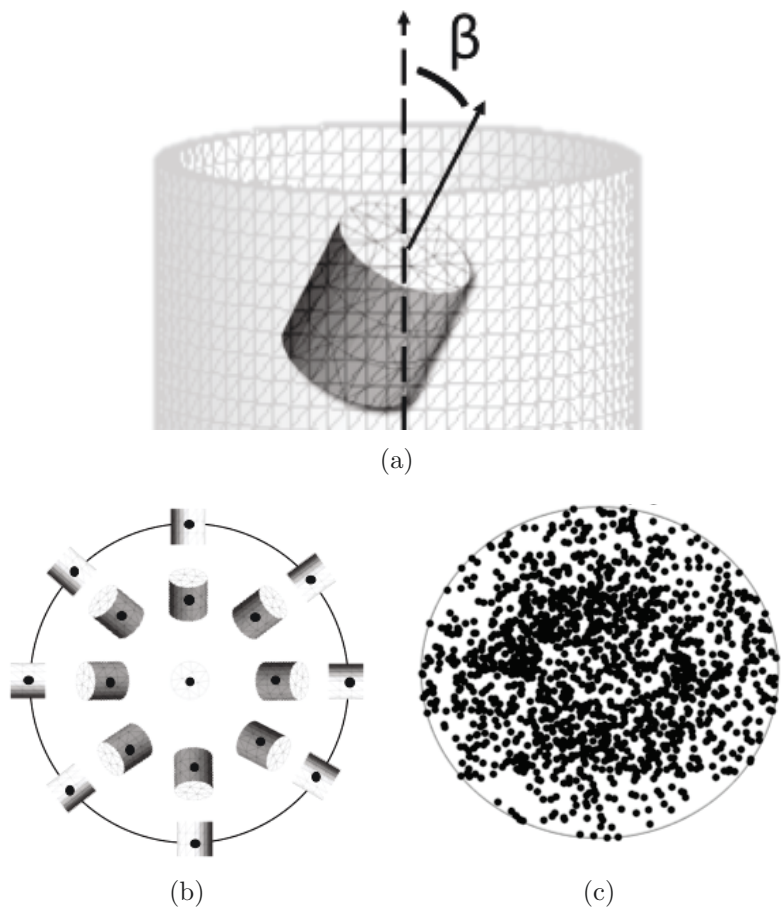


Figure 6.6: a) Angle between the axis of the catalyst support and the axis of the container; b) plotted pellet orientations as they would appear from above the container; c) stereographic projection of the orientations of a cylindrical catalyst support packed structure.

6.4 Comparison study for packs of cylinders

A 44.5 mm inner diameter cylindrical container has been filled with more than three thousand ceramic pellets. The A38 catalyst support (one specific size and aspect ratio considered by Caulkin and co-workers in their experiments for which X-Ray CT analysis is available) is a cylinder of 3.42 mm in diameter and 3.46 mm in width, which gives a 3.90 mm volume-based particle diameter (i.e. the diameter of a sphere

with the same volume as one of the pellets is 3.90 mm). As shown in Figure 6.1 and 6.2(a), this pellet is discretised with 159 tetrahedra and the cylindrical container with 29,327 tetrahedra, for a total of approximately five hundred thousand elements for the whole model. In the numerical simulations the particles are modelled as rigid bodies with a density of 2.41 g/cm^3 and the interaction between each pellet is computed with a Coulomb coefficient of friction in the range 0.6-0.9. This range was considered on the basis of the published sliding friction coefficients for ceramic materials [Denape & Lamon (1990)]. The damping coefficient employed to represent the energy loss due to the impacts is in the range 0.4-0.6. The particles are introduced in the domain above the container base in layers of forty-nine pellets each, from a fixed height, with random orientations and zero initial velocity. The axial packing density profiles that have been calculated for the numerical simulations for the packing of the A38 catalyst supports have been plotted with the corresponding curve extrapolated from the X-Ray CT scans in Figure 6.7. Four Solidity FEMDEM simulations, corresponding to the four possible combinations of the extreme values for the friction and damping coefficients in the considered parameter space have been compared to the experimental results. Due to experimental constraints, the profile that has been reported in Caulkin *et al.* (2015) represents the axial packing density from 3 to 17 particle diameters only. Because of this, it has not been possible to compare the wall effects at the bottom of the container that have been captured by the FEMDEM simulations with the experimental curve. The numerical results for the average packing density within the range of friction and damping coefficients investigated are in agreement with the corresponding experimental results from the X-Ray CT scans. The fact that the simulated profiles present a higher amplitude and a frequency close to the particle size when compared to a relatively flat experimental profile suggests that the final packing structure in the numerical simulations is more ordered than the experimental pack. This could be an effect of possible

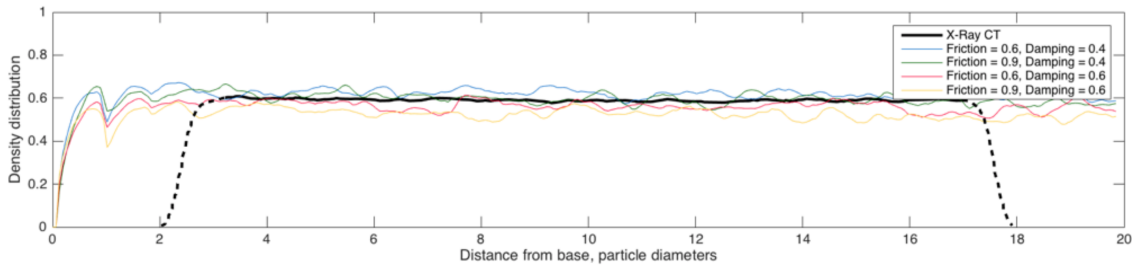


Figure 6.7: Axial packing density distributions extrapolated from the X-Ray CT scans (in black) from Caulkin *et al.* (2015), and from the numerical simulations of simple cylindrical catalysts with different values for friction and damping coefficients (in blue, green, red and yellow).

differences in the loading i.e. particle entry conditions that have not been reported in Caulkin *et al.* (2015), such as the dropping height, the number and the way the particles have been dropped inside the container, etc. Similarly, the radial packing density profiles in Figure 6.8 show almost as good a match between the numerical and the experimental results and confirm the stronger regularity in the simulated packing structures.

The statistics of the pellet orientations for the angle between the axes of the cylindrical pellets and the axis of the container were extrapolated by Caulkin *et al.* (2015) from their X-Ray CT scans. The corresponding numerical simulations of the A38 catalyst support pack are shown in Figure 6.9. Also in this case the numerical results are in general terms in close agreement with the experimental distributions. The stereographic projections representing the pellet orientations of the four numerical simulations are shown in Figure 6.10. Since the experimental statistics for the pellet axis azimuth angles have not been provided in Caulkin *et al.* (2015), it has not been possible to make a comparison for this dataset. However, it is interesting to comment on the four stereographic projection patterns which suggest some qualitative differences already seen in Figure 6.10 are indicated such as the large proportion of 45° inclinations for these cylindrical pellets.

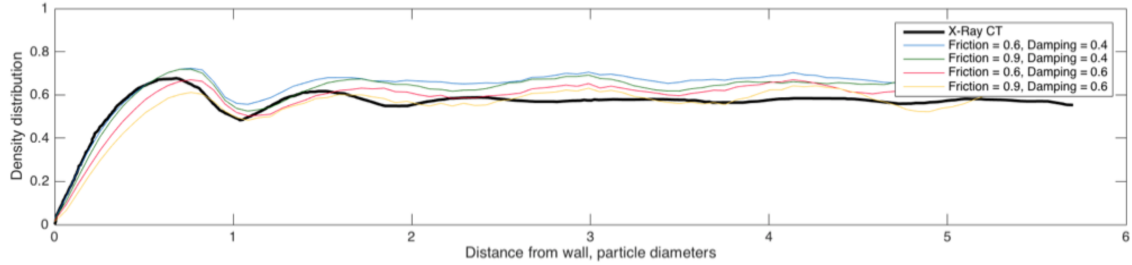


Figure 6.8: Radial packing density distributions extrapolated from the X-Ray CT scans (in black) from Caulkin *et al.* (2015), and from the numerical simulations of simple cylindrical catalysts with different values for friction and damping coefficients (in blue, green, red and yellow).

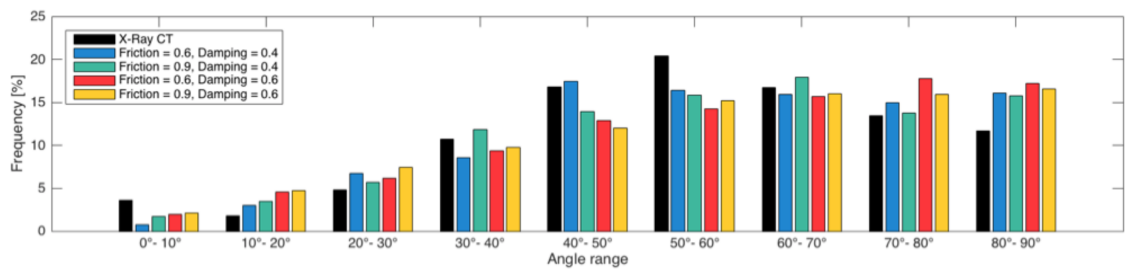


Figure 6.9: Vertical orientation distributions extrapolated from the X-Ray CT scans (in black) from Caulkin *et al.* (2015), and from the numerical simulations of simple cylindrical catalysts with different values for friction and damping coefficients (in blue, green, red and yellow).

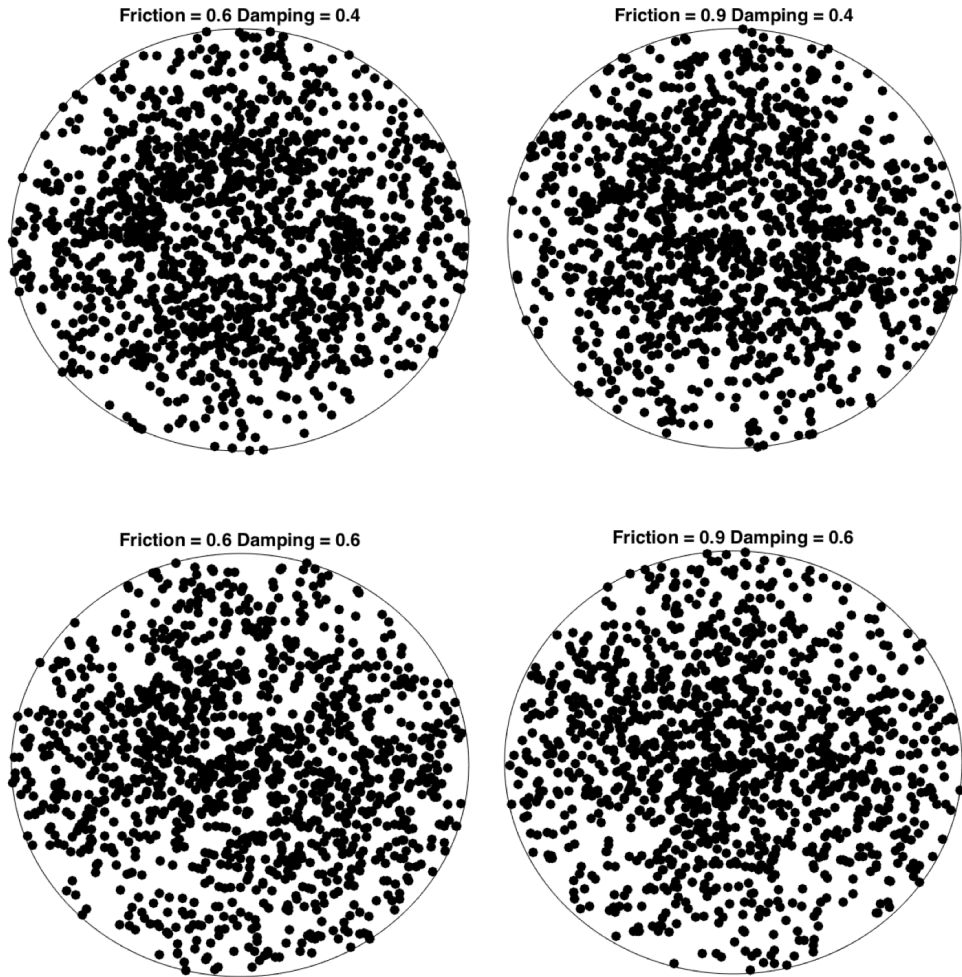


Figure 6.10: Stereographic projections representing the pellet orientations of the numerical simulations with four combinations of friction and damping coefficients.

6.5 Comparison study for packs of spheres and trilobes

A 19 mm inner diameter cylindrical container has been filled first with two thousand glass beads and then with two thousand glass or ceramic trilobes. The spheres that have been packed have a diameter of 2 mm. Trilobes are catalyst supports with a base of approximately 1.3 mm in diameter and 4 mm in width, which gives a 2 mm volume-based particle diameter. As shown in Figure 6.11(a) and 6.11(b), each sphere is discretised with 1372 tetrahedra and each trilobe with 2190 tetrahedra, for a total of approximately two million and seven hundred thousand elements for the whole model. In the numerical simulations the particles are modelled as rigid bodies with a density of 2.5 g/cm^3 . The interaction between each pellet is computed with a Coulomb coefficient of friction of 0.1. The damping coefficient employed to represent the energy loss due to the impacts is 0.1. The values of sliding friction and restitution coefficient were not provided in Nguyen *et al.* (2005). For this reason an informed guess of these two parameters was made with a parametric study, taking into account the values for glass and ceramics that are generally reported in the literature. In order to avoid an artificial regularity of the pack, this time the spheres and trilobes are introduced into the domain above the container base in a random irregular grid of one hundred pellets each, from a fixed height, with random orientations and zero initial velocity, as shown in Figure 6.12(a) and Figure 6.12(b) respectively.

The two Solidity FEMDEM simulations, corresponding to the two particle shapes have been compared to the experimental results but this time only the experimental radial packing density profiles were reported in Nguyen *et al.* (2005). Because of this it has not been possible to compare the other set of data that have been extrapolated from the numerical results. The radial packing density profiles in

Figure 6.14 show a good match between the numerical and the experimental results for the pack of glass beads. Moreover, the periodicity of the boundary effects is well represented by the numerical simulation, showing five distinctive peaks in the density distribution profile. The radial packing density profiles in Figure 6.15 show almost as good a match between the numerical and the experimental results for the pack of trilobes, with the simulated density marginally lower. In this case, both the experimental and numerical results have a single drop, suggesting that the boundary effects are limited to the proximity of the container. This difference in the pack structure for the two particles can be found also when comparing the average packing density perpendicular to the axis of the container extrapolated from the numerical simulations. In Figure 6.16 the glass beads are arranged in concentric rings that propagate from the wall to the centre of the container. For trilobes, the periodicity away from the wall cannot be maintained. In Figure 6.17 the trilobes make just one ring in proximity of the wall, resulting in a less ordered packing structure for the inner part of the container. This difference in the order of the packed structure for the two particle geometries could be explained with the following consideration. For each possible location that a particle may assume, the number of all the possible stable configurations that are available for a trilobe pellet (i.e. all the possible orientations that are allowed by the neighbouring particles) is much larger if compared to the only possible stable configuration of a sphere, since all the orientations of a sphere are equivalent due to its symmetry. For this reason, while the container walls effects are propagated through the whole pack by the spheres, the trilobe pellets attenuate the boundary effects due to their much larger degree of freedom. In Figure 6.18 the axial packing density profile extrapolated from the numerical results of the pack of glass beads is compared to the one obtained from the simulation of trilobes. Again, the boundary effects are much more pronounced in the pack of spheres, with four distinctive peaks in the proximity of the container

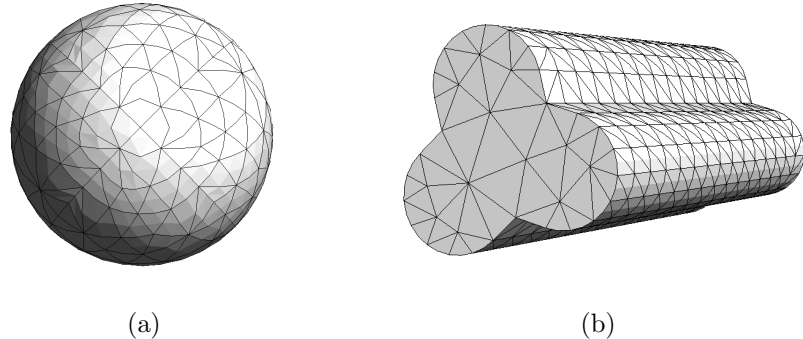


Figure 6.11: Numerical discretisation of particle geometry a) spherical glass bead and b) trilobe ceramic pellet as used for the experiments in Nguyen *et al.* (2005).

base. Both profiles have a negative slope, representing the higher compaction of the deeper layers of particles as determined by the over-burden mass of the particles above which has a more pronounced effect for this low friction packing than the case of solid simple cylinders . Figure 6.19 shows the statistics of the trilobe orientations for the angle between the axis of the pellet and the axis of the container that have been extracted from the numerical simulations. Due to the large aspect ratio of these particles, the configurations nearer to vertical (from 0° to 50°) are unstable upon first contacts and therefore the trilobes in the pack structure are mostly in the horizontal orientations. This is in stark contrast to the cylinders shown in Figure 6.9. The cylinders simulated in the previous Section had an aspect ratio close to one, which encouraged the stability orientations to be more widely distributed and to include virtually all angles including close to the vertical. This difference is expressed very clearly in the stereographic projections for the cylinders in Figure 6.10, which are scattered across all orientations throughout the whole domain, whereas for the trilobes in Figure 6.10, they tend to occupy the outer region of the plot, representing the sub-horizontal configurations.

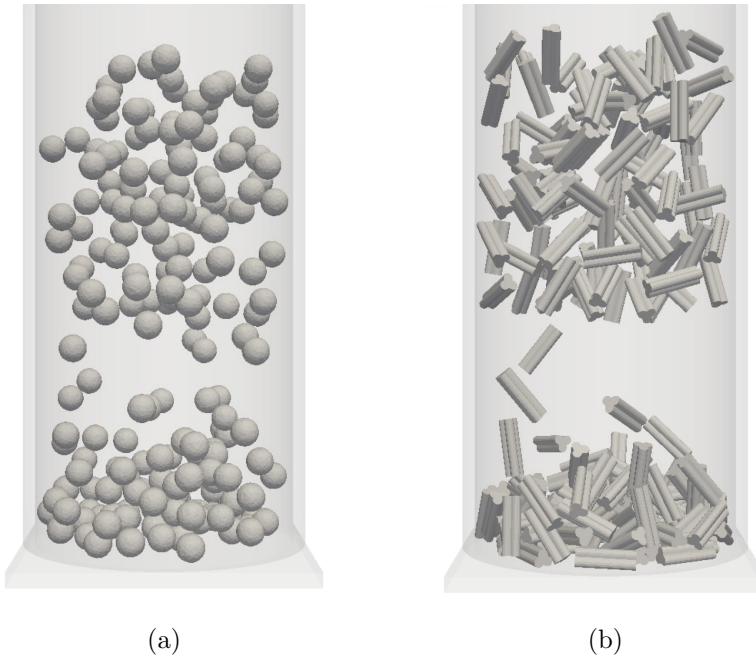


Figure 6.12: Deposition process for the simulated packing structures of the two particle geometries: a) glass beads and b) trilobe pellets.

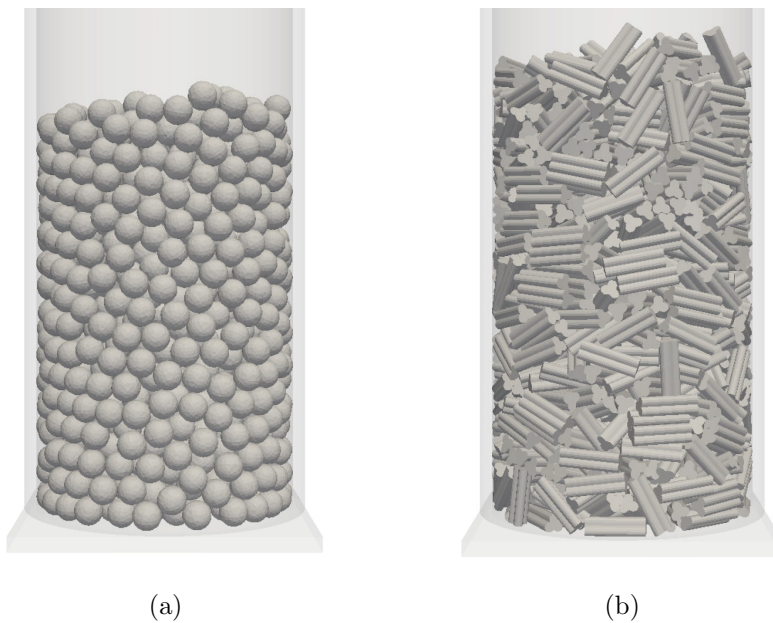


Figure 6.13: Final simulated packing structures of the two particle geometries; pack of a) glass beads and b) trilobe pellets.

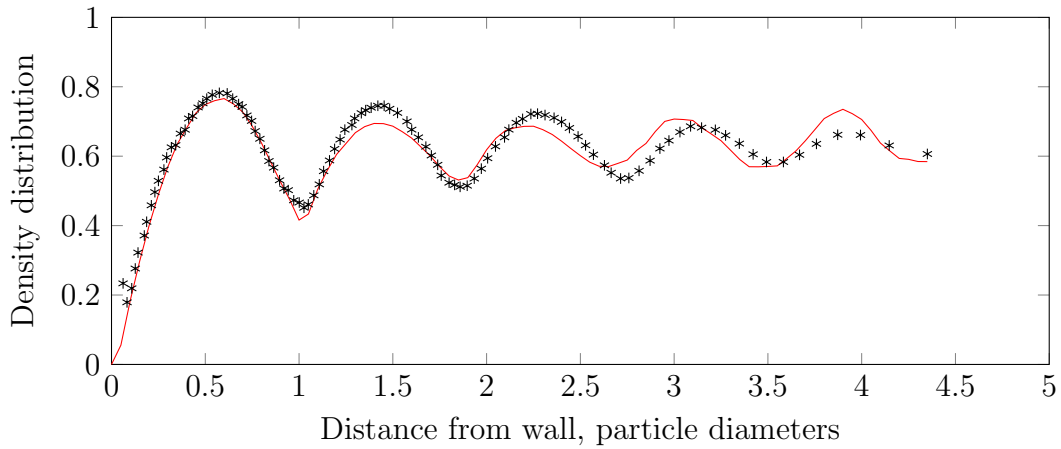


Figure 6.14: Packing density fluctuations in spheres: radial packing density distributions extrapolated from the X-Ray CT scans (in black) from Nguyen *et al.* (2005), and from the numerical simulations in a cylindrical container (red).

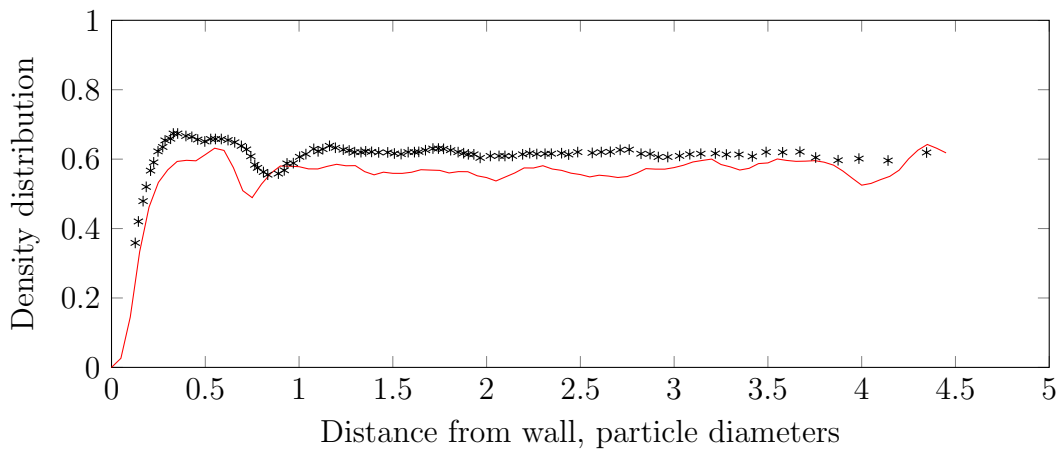


Figure 6.15: Packing density fluctuations in trilobes: radial packing density distributions extrapolated from the X-Ray CT scans (in black) from Nguyen *et al.* (2005), and from the numerical simulations in a cylindrical container (red).

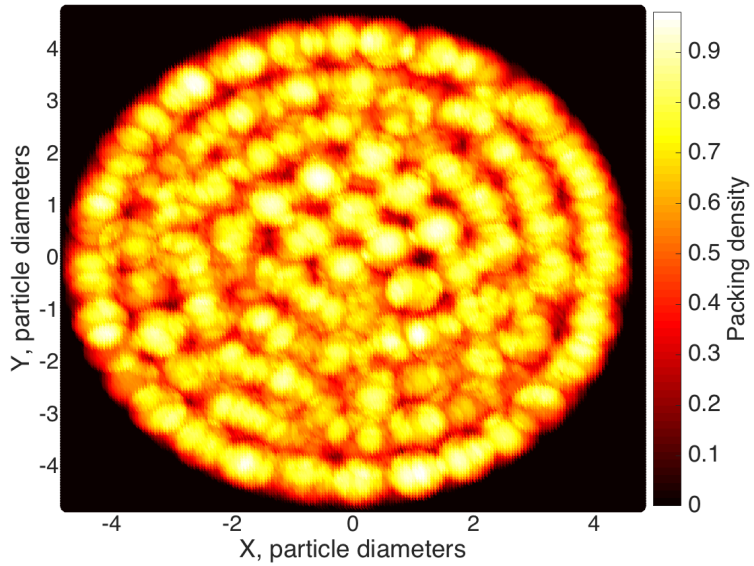


Figure 6.16: Variation of packing density in spheres: average packing density perpendicular to the axis of the container as sampled within each x,y location as described in Section 6.2.

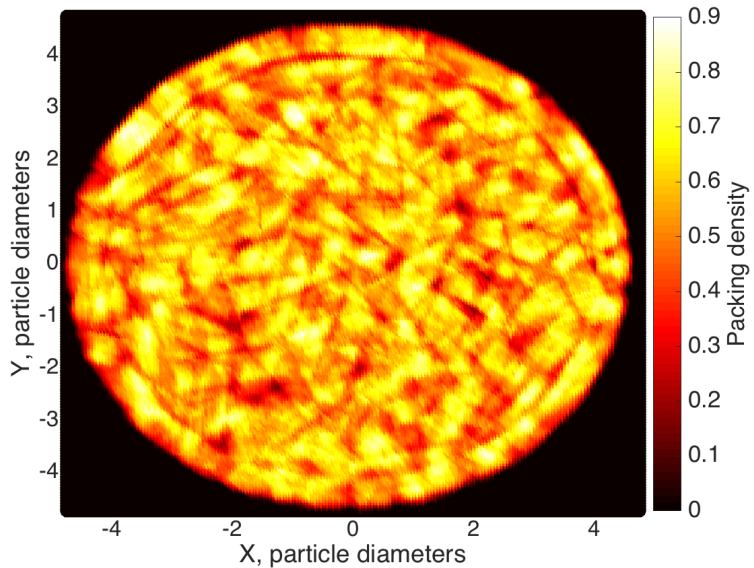


Figure 6.17: Variation of packing density in trilobes: average packing density perpendicular to the axis of the container as sampled within each x,y location as described in Section 6.2.

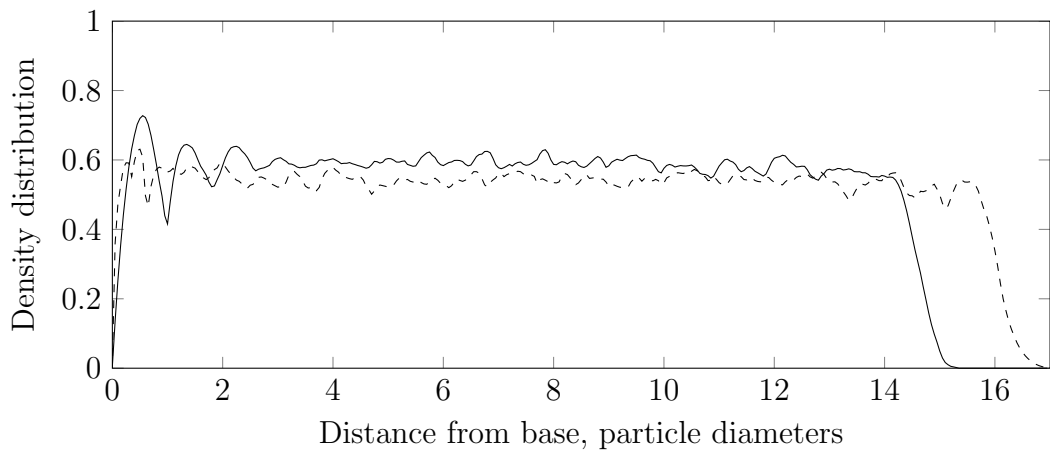


Figure 6.18: Axial packing density variations extrapolated as derived from the numerical simulations of spheres (continuous line) and trilobes (dashed line) in a cylindrical container.

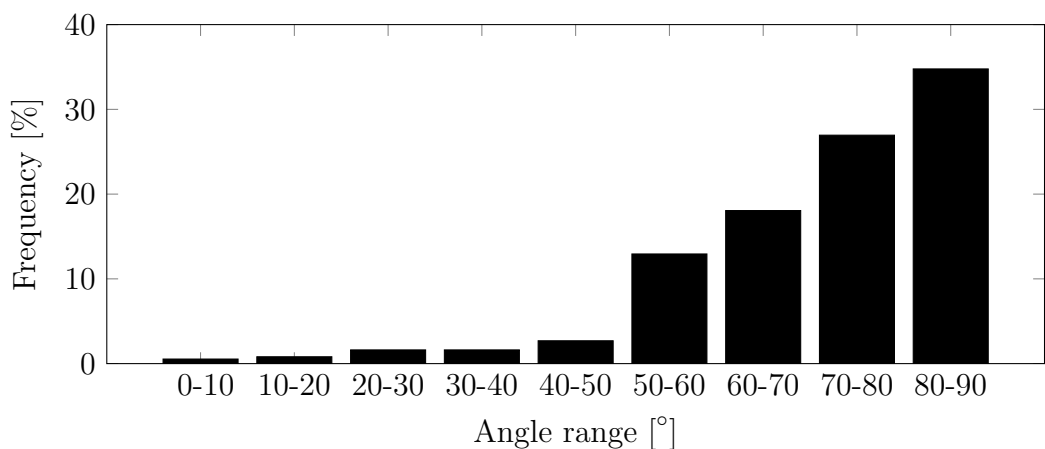


Figure 6.19: Orientation distribution derived from the numerical simulations of packing of trilobes in a cylindrical container.

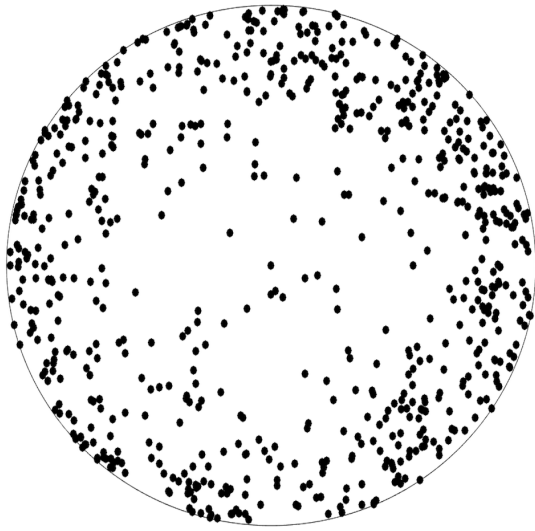


Figure 6.20: Stereographic projections representing the pellet orientations as derived from the numerical simulations of packing of trilobes in a cylindrical container.

6.6 Concluding remarks

Some examples of Solidity FEMDEM simulations for modelling multi-body interactions have been presented in Chapter 6. These have included the representation of the dynamic interactions between the catalyst supports during the loading (i.e. container filling) phase. As has been pointed out in Section 5.2.1, regular deposition grids of particles (i.e. particles with their centres of gravity placed with equal spacing in the two horizontal directions) and with random orientations tended to generate packed structures with artificial regularities. With the purpose of simulating the depositing of pellets in a manner similar to real pouring processes and in ways that can be expected to be highly random, the pre- and post-processing tools (POSITIT and PORSO) have been further improved with algorithms developed in collaboration between the author and supervisor Dr Xiang and finally validated. This has included the specific task to verify that during the container filling stage,

and prior to switching gravity on, particles were generated within the domain with random orientations and a procedure to prevent regular spaced locations in a user-defined deposition volume. This verification has been carried out first by analysing the orientation distributions on a stereo-net of the generated particles and second by examining the distributions of the coordinates of the centroids. It is worth mentioning that the literature has a considerable number of recommended procedures to generate random orientations, but when implemented show a marked lack of randomness. More research needs to be carried out to study in detail the relation between feeding conditions and properties of the obtained packed structures and to design a range of new improved deposition algorithms that can be recommended for different practical cases of particle entry.

6.6.1 Emergent bulk properties

Packing simulations with DEM are normally employed to estimate the packing density and topological structure. As summarised in Stitt *et al.* (2015), in order to characterise natural and industrial packed structures emergent properties of the pack are normally extrapolated from simulation results. For the same reason, these emergent bulk properties, i.e axial and radial packing density profiles, orientation distributions, etc., are the quantities that are employed for packing simulations validations. In Chapter 6, experimental and numerical axial and radial packing density profiles and orientation distributions have been compared, confirming that the Solidity FEMDEM numerical simulations of packing of the A38 cylindrical catalyst supports, glass beads and trilobe pellets deposited in a cylindrical container match the corresponding emergent bulk properties obtained from X-Ray CT scans within very encouraging limits. Future research is needed to quantify the improvements in accuracy comparing the results from Solidity FEMDEM simulations with

corresponding results from other simulation tools (e.g. DigiPack, Rocky, etc.). A different criterion for validation would be to evaluate the contact force statistics in the packing structure and will be discussed in Section 7.2.

Chapter
SEVEN

Conclusions and future research

7.1 Conclusions

Based on the observations and results of the research work presented, the following conclusions were made:

- The mechanical characterisation of engineered high performance materials (e.g. the ceramics employed as catalyst supports) is a crucial field in material science. The material properties of small ceramic samples with different geometries (i.e. prismatic bars, discs and cylindrical pellets with four holes) were needed in order to perform Solidity FEMDEM numerical simulations and thereby evaluate the likely fracture behaviour of complex shaped pellets. The specimens were tested employing different testing techniques, including uniaxial compression (creating indirect tension in disc specimens), ultrasonic test,

nanoindentations, mercury (Hg) intrusion, Brunauer-Emmett-Teller (BET) adsorption and three-point bending test. The prismatic bars that need testing were too small for the standard method to be applied. For this reason a new methodology for the calculation of the full deflection profile from video recordings of bending tests and an optimisation algorithm for the characterisation of Young's modulus were developed. The presented results not only confirmed that the method could be used to estimate the stiffness of the specimens that were to be tested in the present work, but also showed the capabilities of this procedure to evaluate the Young's modulus of small and highly stiff specimens with greater accuracy than previously possible with bending tests, by employing all the available information from the video recording of the tests. In other words, the proposed methodology extends to this class of materials the possibility to evaluate both the elastic modulus and the tensile strength with a single mechanical test, without the need for other experimental tools;

- The series of validation studies that have been conducted have provided first confirmations that the FEMDEM method employed in Solidity can also be applied to the simulation of fragmentation of very strong (by comparison with most geomaterials) porous ceramic bodies;
- The results that have been presented have shown that the simulated structural stiffness is strongly sensitive to the mesh size. This is a strong limitation of the applicability of the code for the simulation of certain types of stiff porous ceramics. The large number of joint elements that is generally needed to correctly discretise the plastic zone during fragmentation can generate an artificial compliance in the simulated elastic behaviour that may not allow the correct representation of the actual deformations of the ceramic samples;
- The experimental results give an insight into the mechanical behaviour of

catalyst supports with four holes, since they quantify the structural strength of this type of pellets for two loading configurations (weak and strong orientations of the holes). Even though limitations in the experimental apparatus reduced the accuracy of the results, the data obtained suggest a consistent relation between loading orientation, tensile strength and the structural strength of the pellets. When normalising the load at failure with the failure load of an equivalent cylinder of identical tensile strength and geometry but without holes, all the results converged to a value of about 2% for the weak orientation and about 20% for the strong orientation;

- The structural strength of complex-shaped pellets under simplified loading conditions was investigated also with numerical simulations. Loading orientations at intervals of 5° have been considered between the weak (0°) and the strong (45°) orientation configuration of the four-hole discs. The load at failure calculated in the numerical simulation for the different orientations has been compared with the experimental data. The values of load normalised with respect to the strength of an equivalent cylinder of identical geometry without holes has not only been shown to be in good agreement with the experimental data for the weak and strong orientations, but also to provide a relation between the loading orientation and the structural strength of four-hole discs which is consistent between different sets of samples. The numerical results slightly overestimate the structural strength of the four-hole specimens at 0° and underestimate the strength at 45°. This might be due to difficulties in the definition of the experimental failure loads and material inhomogeneity defects in the real samples;
- Regular deposition grids of particles (i.e. particles with their centres of gravity placed with equal spacing in the two horizontal directions) and with random orientations tended to generate packed structures with artificial regularities.

The pre-processing tool (POSITIT) has been further improved to simulate the deposition of pellets in a manner similar to real pouring processes and in ways that can be expected to be highly random and finally validated. This improvement was verified by analysing the orientation distributions on a stereo-net of the generated particles and by examining the distributions of the coordinates of the centroids, confirming that the code is capable of depositing pellets with random grids;

- Experimental and numerical axial and radial packing density profiles and orientation distributions have been compared, confirming that the Solidity FEMDEM numerical simulations of packing of the A38 cylindrical catalyst supports, glass beads and trilobe pellets deposited in a cylindrical container match the corresponding emergent bulk properties obtained from X-Ray CT scans within very encouraging limits.

7.2 Future research

Suggested extensions of the presented research work include the following:

- Further research needs to be undertaken to understand how different die compaction and sintering tools can affect the final material properties of catalyst pellets;
- Further research could also be undertaken to extend the method to materials with more complex constitutive behaviour, such as specimens that exhibit significant plastic deformations before failure. Current developments in the Solidity FEMDEM code now allow the simulation of plastic deformations. A possible avenue for future work could be to use the code to perform back analysis of the plastic parameters needed in any given elastic-plastic constitutive

model to simulate the performance of structures with elastic-plastic components;

- New code implementations in the Solidity FEMDEM code should be developed to reduce the artificial compliance due to the large number of joint elements that is generally required to correctly discretise the plastic zone during fragmentation. A possible future research approach to address this shortcoming might be to replace the current employed cohesive law with an extrinsic traction separation law. The strategy would be to calculate the stress and displacement field employing an extrinsic traction separation (or cohesive) law [Kubair & Geubelle (2003) and Nguyen (2014)]. The constraint on the relative displacements between adjacent finite element nodes is then relaxed only when the stresses reach the value of tensile or shear strength and a fracture propagates. The difference between the current and the proposed cohesive laws is schematised in Figure 7.1.

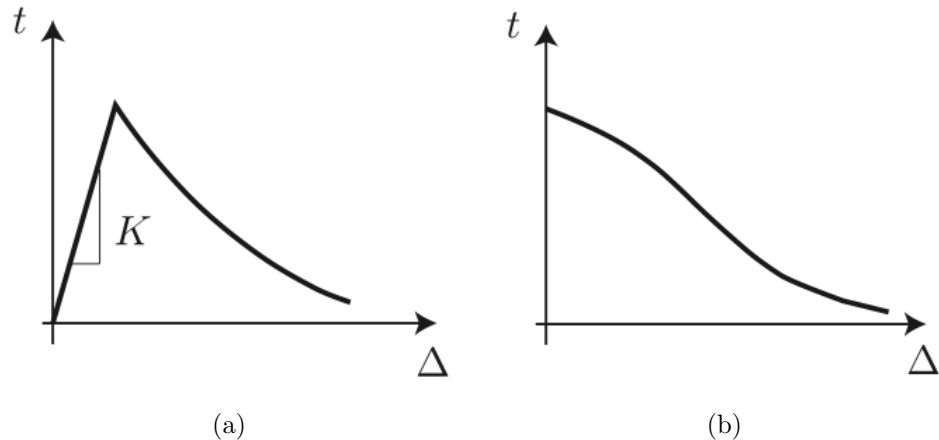


Figure 7.1: (a) Intrinsic and (b) extrinsic cohesive law or traction separation law. They are also known as initially elastic and initially rigid traction separation laws [Nguyen (2014)].

- Experiments on pellets with four holes might be repeated with a different

higher loading capacity apparatus to obtain results for the strongest set of pellets (Set 3), and to increase the level of accuracy in the definition of the load values at failure;

- Apart from the structural strength of catalyst supports, other interesting insights can be obtained from 2D Solidity FEMDEM numerical results. These include the capability of extracting the fragment size distribution from the simulated crushed pellets leading to the characterisation of the post-failure behaviour associated with a certain shape. Future research can be undertaken to determine numerically the tendency of a certain shaped catalyst support to break into fine or bigger fragments which could be of industrial interest by contributing to pressure drop prediction and improvements in the performance of catalysts;
- The Solidity FEMDEM code can also simulate shear failure and given the complex shapes and loading conditions, the importance of this mode of failure may have been under-estimated . Future research on microstructure and its representation in simulating failure with FEMDEM could be carried out to study the alternative modes of failure of catalyst supports.
- A microstructural characterisation of the geometry of elementary elements (i.e. grains) that constitute the porous ceramic microstructure could be carried out. The dissemination of these elementary elements in a representative volume might be used to define the model domain, as shown in Figure 7.2. These data could be recovered with a reasonable accuracy from 3D micro-images of samples where the geometrical features of the structure are carefully resolved and digitally represented in the computer. Such images are available from high-resolution X-ray tomography, also known as CT-scanning. However, high-resolution scanning devices are prohibitively expensive and time

consuming. A statistical reconstruction of 3D volume from 2D sections could be an alternative to avoid expensive pieces of equipment. These sections are relatively easy and cheap to prepare and they can be image-processed to capture void and grain geometries. The statistical properties of this 2D geometry, such as porosity, autocorrelation length, grain size distribution, etc. could then be calculated from the images. Finally, it could be assumed that a 3D space has the same statistical properties as the thin section, and an algorithm (e.g. the sequential indicator simulation, Voronoi tessellation) could be used to create a 3D structure with approximately the same properties distribution, as shown in Figure 7.3. With these assumptions, a representative volume of the microstructure can be defined (generally 50-150 grains). The mechanical behaviour of ceramic grain structures can then be modelled on the basis of the following hypotheses: the single grain behaves as an elastic orthotropic medium, fragmentation is modelled only between grain boundaries with a linear cohesive law, and friction between grains after grain boundary failure and between fragments is implemented with a Coulomb linear model. Applying different boundary conditions to the representative volume it may be possible to reconstruct the mechanical behaviour of the grain structure and infer the parameters that best describe porous ceramics at the macroscale, as shown in Figure 7.4. With the definition of the shear failure parameters, similar simulations to the ones that have been shown in Section 5.2.1 could handle fracturing in arbitrarily complex loadings and shapes as the stresses would be captured in just the same way;

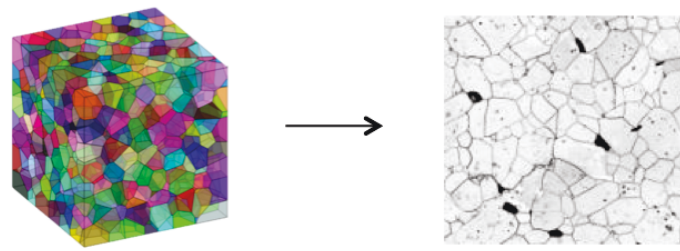


Figure 7.2: Grains constituting the microstructure of a ceramic sample and their equivalent in a simulated volume of ceramic.

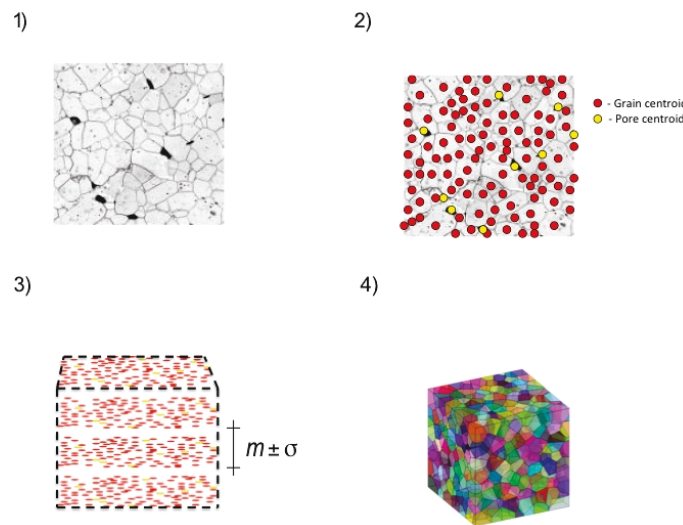


Figure 7.3: A statistical reconstruction of 3D volume from 2D sections.

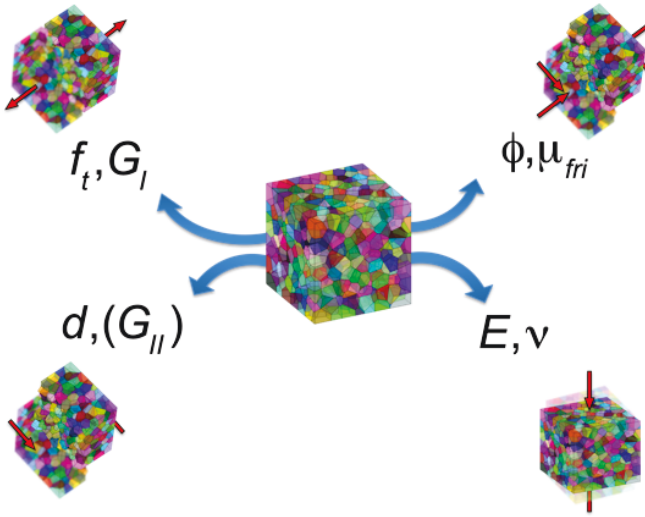


Figure 7.4: Different boundary conditions that can be applied to the representative volume to reconstruct the mechanical behaviour of the grain structure and infer the parameters that best describe both ceramics and rocks at the macroscale.

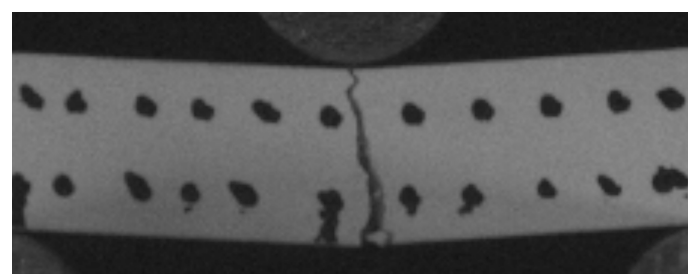
- Catalyst supports could also experience dynamic loads, for instance during the pouring process, when the pellets are deposited inside the reactor. Preliminary investigations of the Solidity FEMDEM code capabilities in the description of pellet fragmentation due to dynamic loads have been conducted and have given first confirmations of the applicability of the code. Future research can be undertaken to further validate the Solidity FEMDEM code for the simulation of dynamic process with porous ceramics. The structural laboratory of the Civil Engineering Department at Imperial has an Instron test machine with a three-point bending test set up. The test machine is completely computerised. Bars from Set 1 were tested with a dynamic three-point flexural test performed on an impact-testing machine, as shown in Figure 7.5. The experiment was performed on the same three-point bending apparatus used for the mechanical characterisation in Chapter 4 (the distance between its two supports is 20 mm). The impactor is a steel cross-head instrumented with a gauge which was placed to record the force experienced by the punch during the experiment: force-

displacement curves was recorded. With the aim of reaching a velocity of 3 m/s, the impactor, which has been attached to a mass of 4 kg, was released about half a meter above the specimen. A high-speed camera was used to record the crack-front propagation process through the specimen thickness. In order to determine the motion of the tested specimen, a set of 22 points were marked on the surface of the beam and the displacements of these markers have been measured by means of a free video analysis software (Tracker). The experiment was modelled with 2D and 3D Solidity FEMDEM simulations. The mesh discretisation for the 2D numerical simulation and the preliminary results from the 3D numerical simulation of a dynamic three-point bending test are shown in Figure 7.6 and 7.6 respectively. Figure 7.6 shows the comparison between the numerical results before and after failure in the 2D simulation and a frame from the high-speed video recording of the actual dynamic three-point bending experiment. Implementing fracture in the 2D and 3D to capture the physical phenomena during a dynamic three-point flexural test with great accuracy is still very much a 'work in progress' as some of the mechanical properties of the specimens need to be achieved and certain aspects of the code that are relevant to the correct representation of fracture need to be validate. One very intriguing development was the observation both in the experimental (Figure 7.9) and simulated test was the occurrence of a double peak in the load deflection response and this would be an interesting target of further research as it points towards the capability to capture complex dynamic stress waves in machine-specimen responses during impact testing.

An example of the possible applications of the code in describing dynamic processes involving catalyst supports can be found in Figure 7.10, where a cylindrical pellet with four holes is fragmenting during an impact at 3 m/s against a steel plate;



(a)



(b)

Figure 7.5: Dynamic three-point bending experiments on bars from Set 1 recorded with (a) standard and (b) high-speed camera.

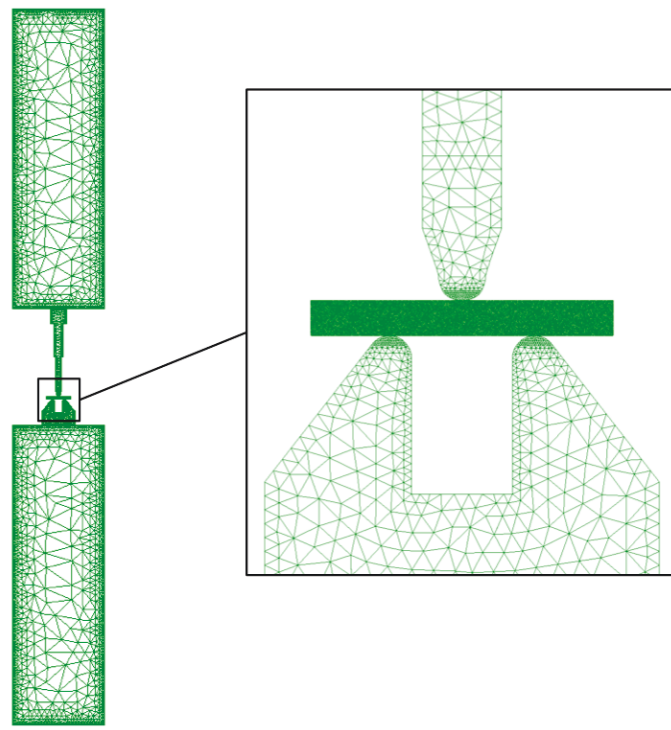


Figure 7.6: Triangular mesh of the 2D numerical simulation of a dynamic three-point bending test.

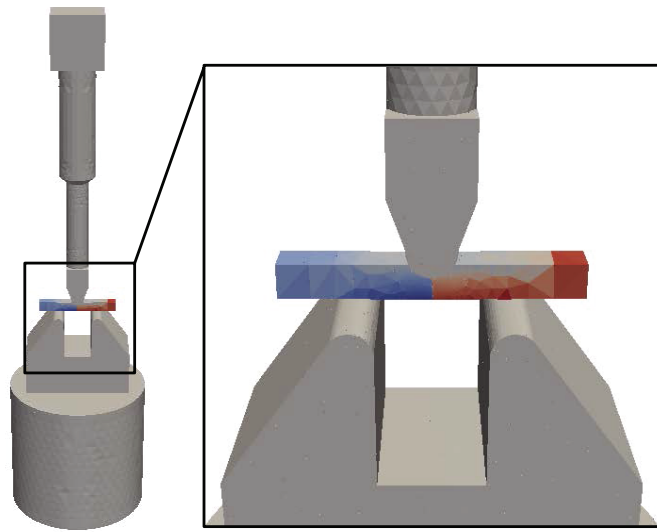
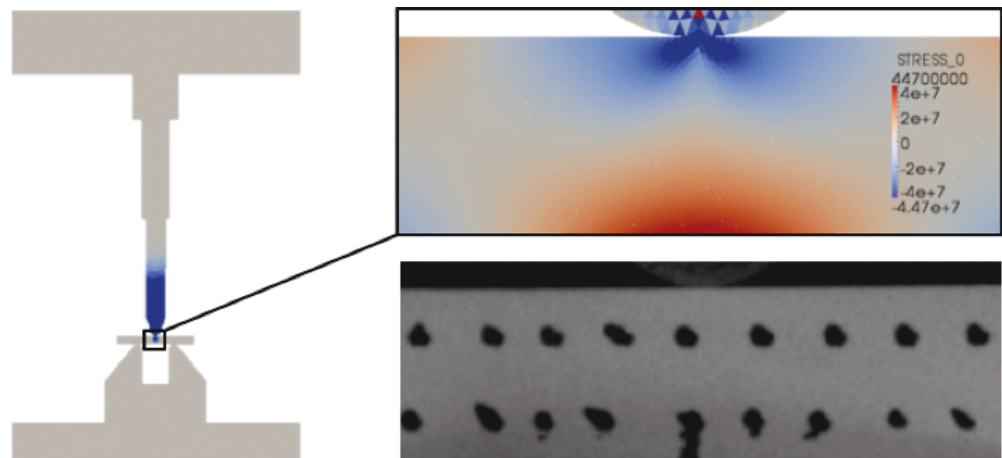
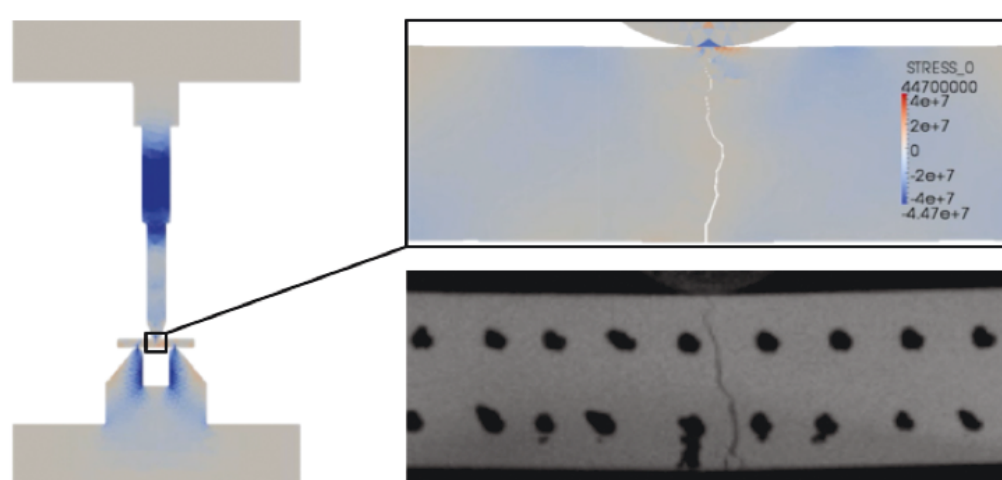


Figure 7.7: Horizontal displacement field in a 3D numerical model of a dynamic three-point bending test.



(a)



(b)

Figure 7.8: Comparison between the model of the specimen (a) before and (b) after failure in the 2D numerical simulation and a frame from the high-speed video recording of the actual dynamic three-point bending experiment.

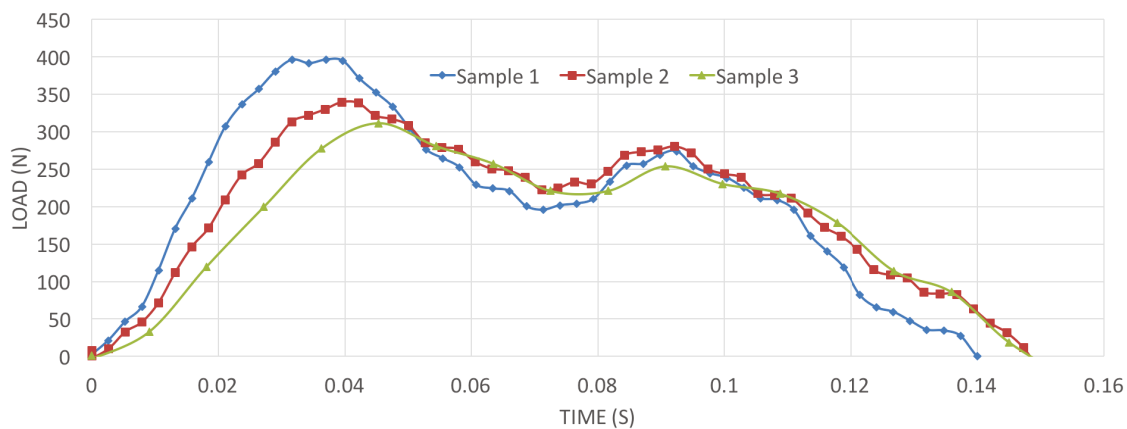


Figure 7.9: Double peak in the load-time response of dynamic three-point bending experiments on three sample bars from Set 1.

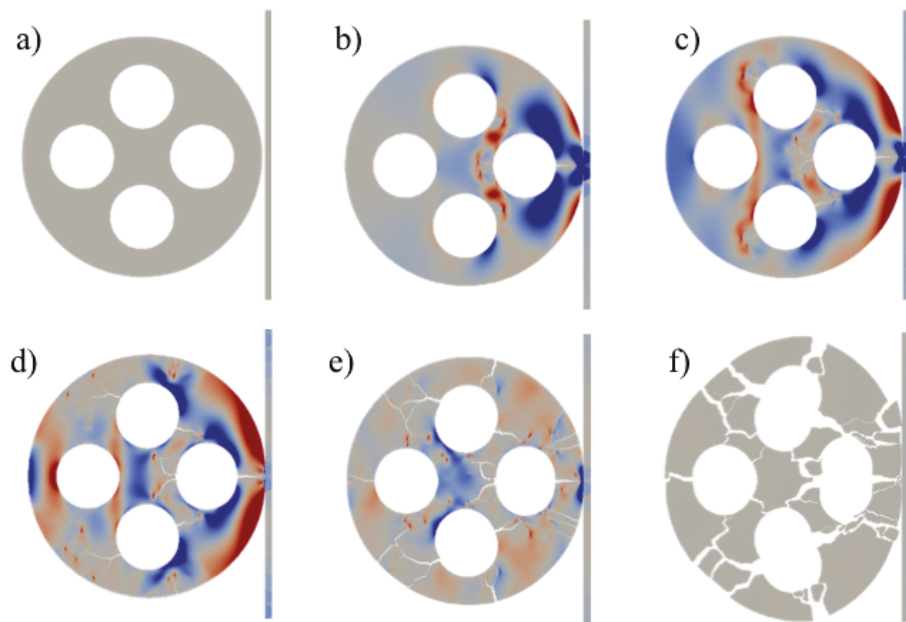


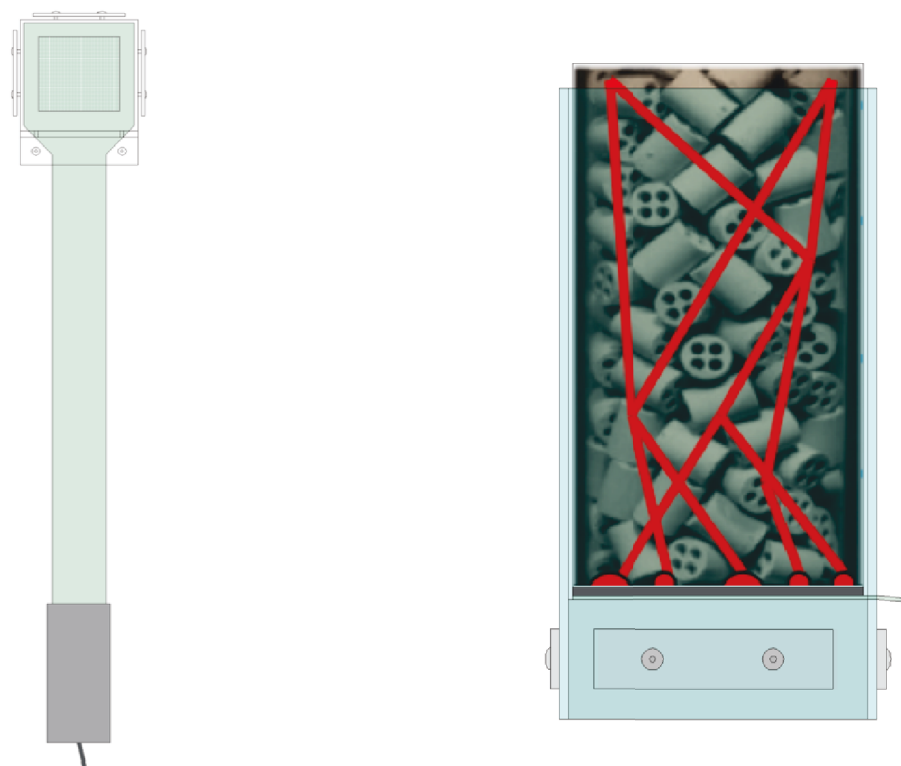
Figure 7.10: Fragmentation of a cylindrical pellet with four holes during an impact at 3 m/s against a steel plate.

- More research needs to be carried out to study in detail the relation between feeding conditions and properties of the obtained packed structures and to design a range of new improved deposition algorithms that can be recommended

for different practical cases of particle entry;

- Future research is needed to quantify the improvements in accuracy comparing the results from Solidity FEMDEM simulations with corresponding results from other simulation tools (e.g. DigiPack, Rocky, etc.);
- A different criterion for validation to the popular one based on packing density would be to evaluate the contact force statistics in the packing structure. This type of work has been done by evaluating the maximum contact force statistics in experiments with photo-elastic stress analysis [Da Silva M & Rajchenbach (2000) and Majmudar & Behringer (2005)] and compare them with corresponding numerical results [Majmudar *et al.* (2007)]. Future research can be carried out to obtain experimental statistics of the contact force history against the container floor and walls during particle deposition. The AMCG at Imperial College London acquired two different load and frequency range pressure sensor pads (supplied by Teckscan) and has undertaken preliminary research to obtain experimental statistics of the contact force history against a surface that has been instrumented with such sensors, as shown in Figure 7.11. The research group has also been provided with about five hundred complex-shaped catalyst supports. As shown in Figure 7.12(a), these pellets have a cylindrical caged shape with four holes. The shape of these pellets has been reconstructed with photogrammetry and CAD software, in order to define the equivalent numerical mesh shown in Figure 7.12(b). Figure 7.13 shows the mesh discretisation from the preliminary results of a pile test with four hundred and ninety of these complex-shaped pellets. Future research can be undertaken to perform pile experiments on a surface that has been instrumented with the pressure sensor to obtain the contact force history of a collapsing pile against the flat surface during the filling and lifting of the container. Figure 7.14 shows the time-lapse of the corresponding nu-

merical simulation from which the contact force history can be extracted and compared with the experimental results;



(a)



(b)

Figure 7.11: (a) Scheme and (b) actual rig for the AMCG's pressure sensors that can be employed to obtain experimental statistics of contact force history.

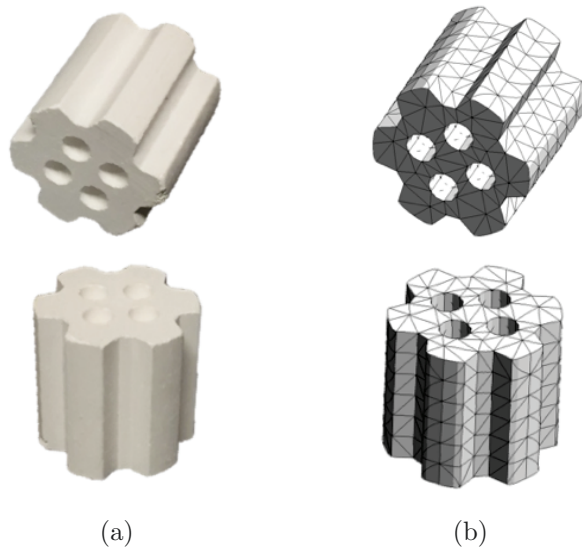


Figure 7.12: Cylindrical cogged shaped pellet with four holes: (a) photograph and (b) its equivalent numerical mesh.

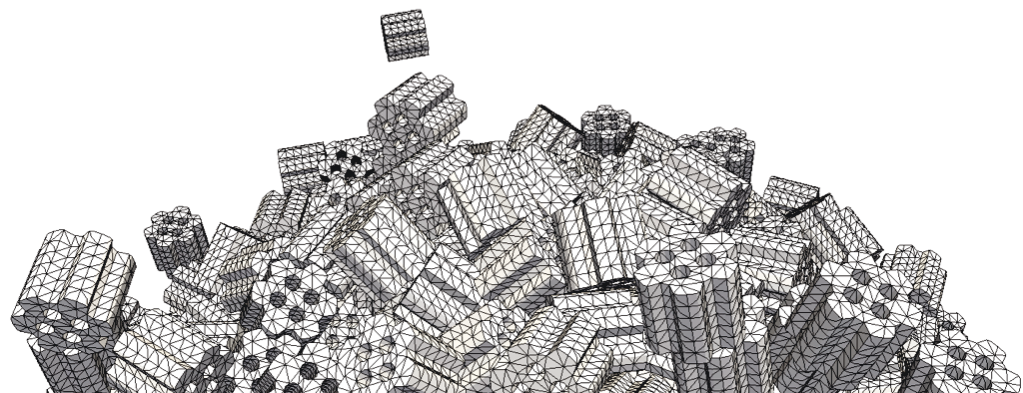


Figure 7.13: Mesh discretisation of the collapsed pile after lifting the container.

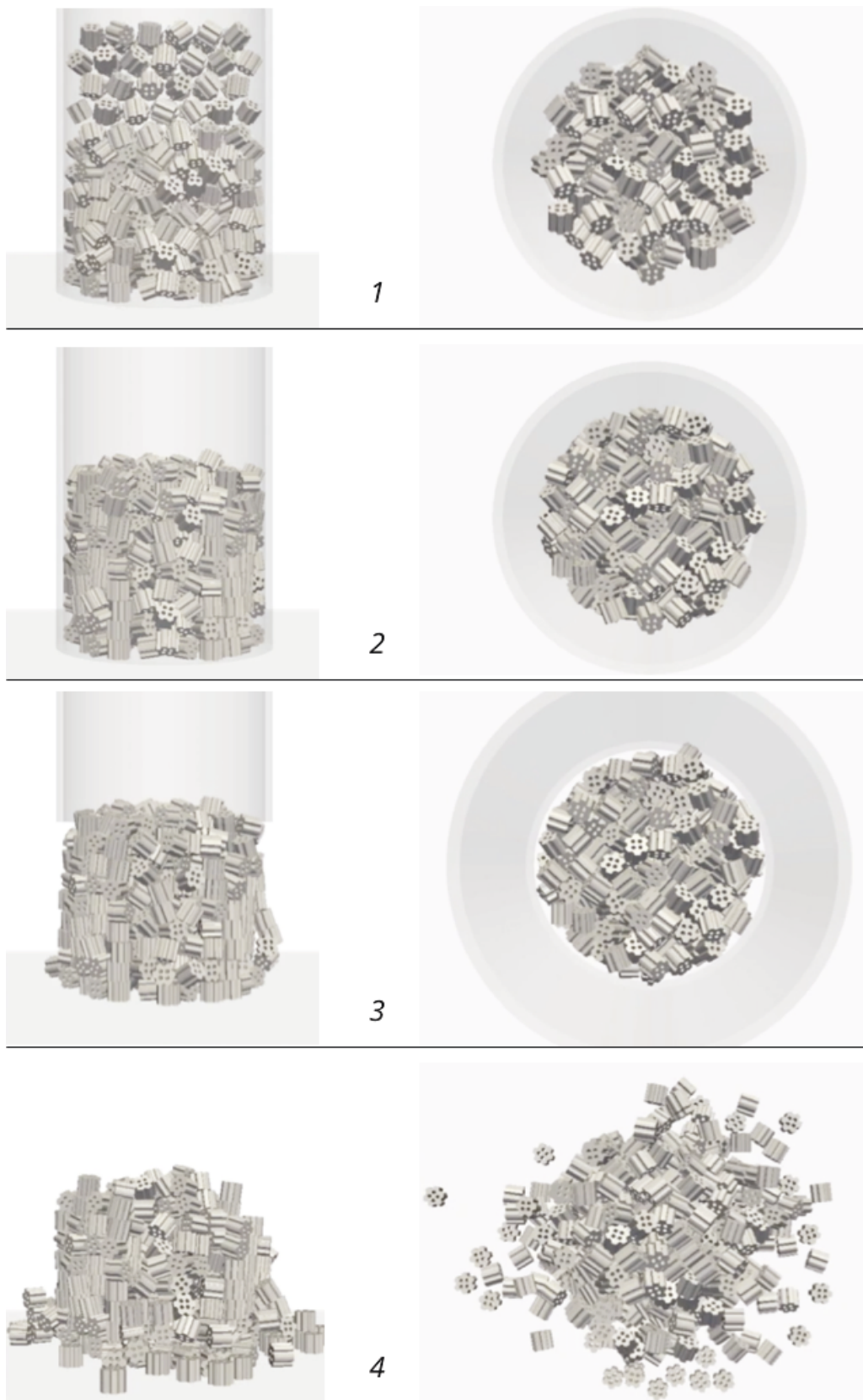


Figure 7.14: Collapsing pile after filling a cylinder (1-2) and lifting it up (3-4).

- The results that have been shown in Chapter 6 have given a first confirmation of the capabilities of the Solidity FEMDEM code in the simulation of packed structures of catalysts in fixed-bed reactors. In Chapter 6 the code has also been used to investigate the structural strength of complex-shaped pellets under simplified loading conditions. The natural extension of the research work that has been undertaken, is to use the Solidity FEMDEM code to represent more realistic loading conditions that can lead to the crushing of catalyst supports when in service inside a reactor. Preliminary simulations have been done to study the effects of a vertical load on a pack of pellets. A pack of one thousand cylindrical pellets, each with one hole in a 19 mm diameter cylindrical container have been simulated. Each pellet has an equivalent diameter of 2 mm and a mass of 10 milligrams. After deposition, the pack is uniaxially compressed with a weight of 250 g. Figure 7.14 shows the force chains and the magnitude of the maximum contact force in [N] experienced by the pellets in the chains. These simulation results show the mechanism utilised by the structure of pellets to transmit the load that have been applied at the top of the pack to the container walls. Since the pellets in the chains are transmitting most of the load, these are also the most vulnerable particles in the pack. The topology and magnitude of the contact force that is transmitted in the force chains is strictly related to the properties of the pack and ultimately to the shape of the pellets. Future research can be undertaken to study the relation between pellet shapes and quality of the force chains;

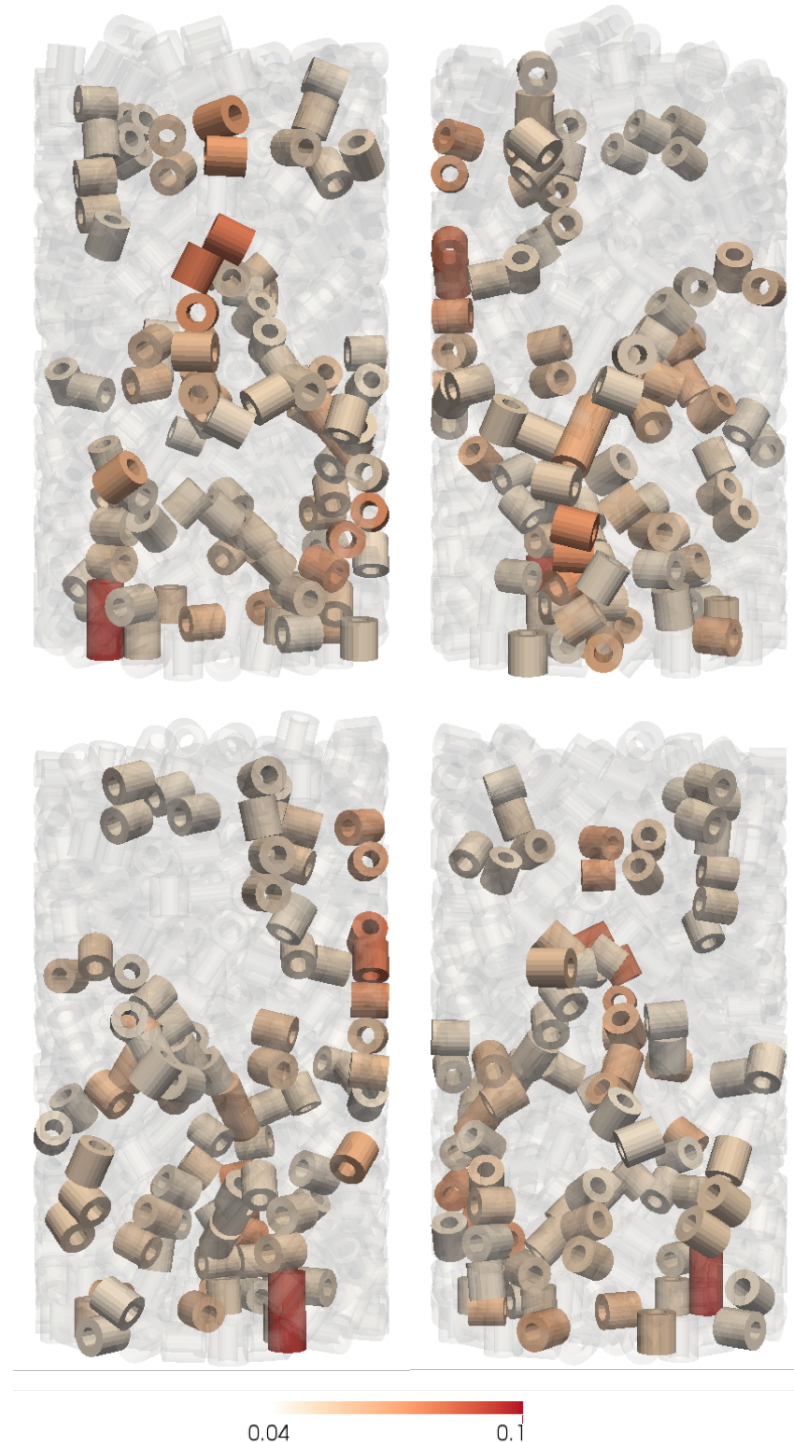


Figure 7.15: Force chains and the magnitude of the maximum contact force [N] experienced by cylindrical pellets of 2mm diameter with one central hole.

- The industrial problem that has been investigated in this research work is

mainly focused on preventing fracture and fines production in fixed bed reactors. For this reason, the ability to evaluate contact forces and stresses in packed structures remains a major future objective. This is especially the case in the light of strong evidence that 2D and 3D FEMDEM simulations can provide excellent fracture prediction. In principle, the 3D structure meshes representing an at-rest packed equilibrium state from rigid Solidity FEMDEM simulations (e.g. the packs simulated in Chapter 6) can be used as input meshes to the deformable Solidity FEMDEM code. Readjustments in the packing structure can then be simulated in order to represent an even more realistic pack where stress varies within particles. However, there are still algorithmic problems to be solved, such as ways to relax the magnitudes of the initially unstably high repulsion forces caused by the inevitably present small but significant overlaps carried over from the rigid simulation. Figure 7.16 shows some preliminary simulations of the stresses experienced by cylindrical pellets in a container. Future work needs to be done to improve the compatibility and interchangeability of the rigid and deformable solvers in the Solidity FEMDEM code and to obtain stable numerical simulations of the stresses experienced by the catalyst supports in a fixed bed reactor. Further code developments are needed to exploit a range of coupled physical processes such as the thermal coupling. Work on introducing many of these in Solidity is underway [Joulin *et al.* (2017)] (i.e. heat conduction, expansion/contraction and thermal transmission at contacts). Solidity has also been coupled with the advanced CFD code Fluidity. It seems reasonable to suggest that thermal and fluid interactions with the solid catalyst pellets in a fixed-bed reactor could, in the near future, be investigated with the simulation methods built from use of the Solidity FEMDEM code;

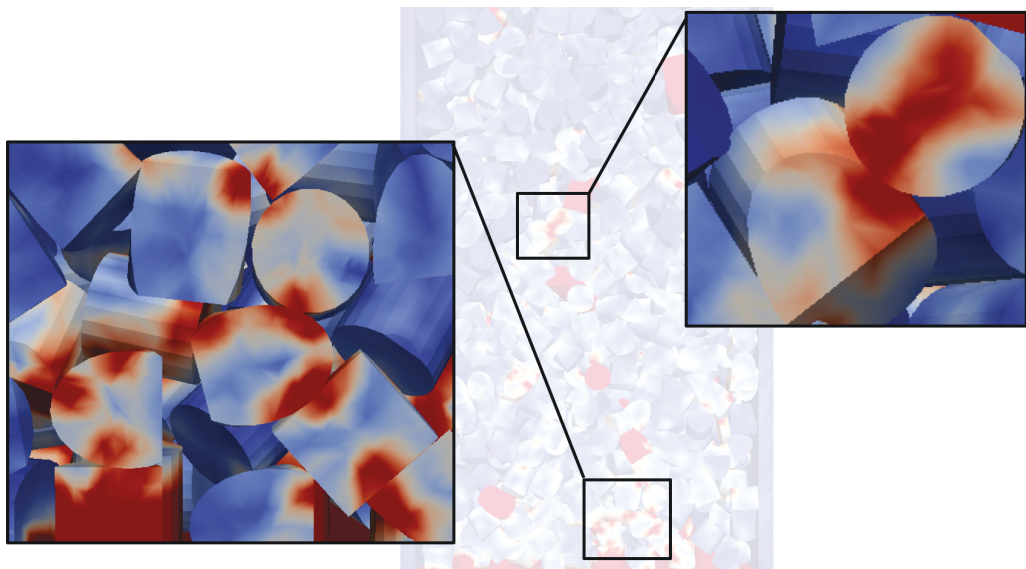


Figure 7.16: Preliminary simulations of the stresses experienced by cylindrical pellets in a container.

References

- Asmani, M, Kermel, C, Leriche, A, & Ourak, M. 2001. Influence of porosity on Young's modulus and Poisson's ratio in alumina ceramics. *Journal of the European Ceramic Society*, **21**.
- Asmar, B.N., Langston, P.a., Matchett, A.J., & Walters, J.K. 2002. Validation tests on a distinct element model of vibrating cohesive particle systems. *Computers and Chemical Engineering Chemical Engineering*, **26**(6), 785–802.
- Berryman, JG. 1983. Random close packing of hard spheres and disks. *Physical Review A*, **27**(2).
- Bordas, S, & Nguyen, PV. 2007. An extended finite element library. *International Journal for Numerical Methods in Engineering*, **71**(January), 703–732.
- Borst, R, Remmers, JC, Needleman, A, & Abellán, MA. 2004. Discrete vs smeared crack models for concrete fracture: bridging the gap. *International Journal for Numerical and Analytical Methods in Geomechanics*, **28**(78), 583–607.
- British Standards Institution. 2007. *Advanced technical ceramics. Mechanical properties of monolithic ceramics at room temperature. Determination of Young's modulus, shear modulus and Poisson's ratio*.

References

- Campbell, CS. 1990. Rapid granular flows. *Annual Review of Fluid Mechanics*.
- Carter, BJ. 2000. Automated 3-D crack growth simulation. *International Journal for Numerical Methods in Engineering*, **47**(1-3), 229–253.
- Caulkin, R, Jia, X, & Xu, C. 2008. Simulations of structures in packed columns and validation by X-ray tomography. *Industrial and Engineering Chemistry Research*, 202–213.
- Caulkin, R, Tian, W, Pasha, M, Hassanpour, A, & Jia, X. 2015. Impact of shape representation schemes used in discrete element modelling of particle packing. *Computers and Chemical Engineering*, **76**, 160–169.
- Chang, L. S., Chuang, T. H., & Wei, W. J. 2000. Characterization of alumina ceramics by ultrasonic testing. *Materials Characterization*, **45**(3), 221–226.
- Cleary, PW, Morrisson, R, & Morrell, S. 2003. Comparison of DEM and experiment for a scale model SAG mill. *International Journal of Mineral Processing*, **68**(1-4), 129–165.
- Da Silva M, & Rajchenbach, J. 2000. Stress transmission through a model system of cohesionless elastic grains. *Nature*, **406**(6797), 708–10.
- David, E. 2015. Mechanical strength and reliability of the porous materials used as adsorbents / catalysts and the new development trends. *Archives of Materials Science and Engineering*, **73**(1), 5–17.
- de Saint-Venant, AJC Barré. 1856. Venant,Memoire sur la torsion des prismes, avec des considerations sur leur flexion, Mem. *Savants Etrang*, **14**, 233–560.
- Denape, J., & Lamon, J. 1990. Sliding friction of ceramics: Mechanical action of the wear debris. *Journal of Materials Science*, **25**(8), 3592–3604.

- Deng, Z. Y., Fukasawa, T., Ando, M., Zhang, G. J., & Ohji, T. 2001. Bulk alumina support with high tolerant strain and its reinforcing mechanisms. *Acta Materialia*, **49**(11), 1939–1946.
- Dupré, J.C., Bornert, M., Robert, L., & Wattrisse, B. 2010. Digital image correlation: displacement accuracy estimation. *EPJ Web of Conferences*, **6**, 31006.
- Eissa, E. A., & Kazi, A. 1988. Relation between static and dynamic Young's moduli of rocks. *International Journal of Rock Mechanics and Mining Sciences and*, **25**(6), 479–482.
- Forterre, Y., & Pouliquen, O. 2008. Flows of Dense Granular Media. *Annual Review of Fluid Mechanics*, **40**(1), 1–24.
- Fu, Q., Saiz, E., & Tomsia, AP. 2011. Bioinspired strong and highly porous glass scaffolds. *Advanced Functional Materials*, **21**(6), 1058–1063.
- Goldhirsch, I. 2003. R Apid G Ranular F Lows. *Annual Review of Fluid Mechanics*, **35**(1), 267–293.
- Green, DJ, Brezny, R., & Nader, C. 1988. The Elastic Behavior of Partially-Sintered Materials. *MRS Proceedings*, **119**(jan), 43.
- Guises, R. 2008. *Numerical simulation and characterisation of the packing of granular materials*. Ph.D. thesis, Imperial College London.
- Guo, L. 2014. *Development of a three-dimensional fracture model for the combined finite-discrete element method*. Ph.D. thesis, Imperial College London.
- Helper, T, Michel, B, Proix, JM, Salvo, M, Sercombe, J, & Casella, M. 2015. Introducing the open-source mfront code generator: Application to mechanical behaviours and material knowledge management within the PLEIADES fuel element

References

- modelling platform. *Computers and Mathematics with Applications*, **70**(5), 994–1023.
- Hild, F, & Roux, S. 2006. Digital Image Correlation: from Displacement Measurement to Identification of Elastic Properties a Review. *Strain*, **42**, 69–80.
- Huang, HL, Detournay, EL, & Bellier, BL. 1999. Discrete element modelling of rock cutting. *Pages 224–230 of: Vail Rocks 1999*, vol. 7.
- International Society for Rock Mechanics. 1978. Suggested Methods For Determining Tensile Strength of Rock Materials. *Pages 99–103 of: International Society for Rock Mechanics Commission on Standardization of Laboratory and Field Tests*, vol. 15.
- Irwin, GR, Kies, JA, & Smith, HL. 1958. Fracture strengths relative to onset and arrest of crack propagation. *Pages 640–657 of: Proc. ASTM*.
- Jirasek, M. 1998. Nonlocal models for damage and fracture: comparison of approaches. *International Journal of Solids and Structures*, **7683**(97), 4133–4145.
- Joulin, C, Xiang, J, Latham, JP, & Pain, C. 2017. *A New Finite Discrete Element Approach for Heat Transfer in Complex Shaped Multi Bodied Contact Problems*. Singapore: Springer Singapore. Pages 311–327.
- Karantzoulis, N, Xiang, J, Izzuddin, B, & Latham, J P. 2013. Numerical implementation of plasticity material models in the combined finite-discrete element method and verification tests.
- Ketterhagen, WR. 2011. Modeling the motion and orientation of various pharmaceutical tablet shapes in a film coating pan using DEM. *International Journal of Pharmaceutics*, **409**(1-2), 137–149.

- Knight, E. E., Rougier, E., Sussman, A.J., Broome, S. T., & Munjiza, A. 2013. Split Hopkinson Pressure Bar Experiment Simulation using MUNROU. *In: 47th US Rock Mechanics.*
- Kubair, Dhirendra V., & Geubelle, Philippe H. 2003. Comparative analysis of extrinsic and intrinsic cohesive models of dynamic fracture. *International Journal of Solids and Structures*, **40**(15), 3853–3868.
- Lam, DCC, Lange, FF, & Evans, AG. 1994. Mechanical properties of partially dense alumina produced from powder compacts. *Journal of the American Ceramic Society*, **77**(8), 2113–2117.
- Latham, John-Paul, Anastasaki, Eleni, & Xiang, Jiansheng. 2013. New modelling and analysis methods for concrete armour unit systems using FEMDEM. *Coastal Engineering*, **77**(jul), 151–166.
- Latham, JP, & Munjiza, A. 2004. The modelling of particle systems with real shapes. *Philosophical transactions. Series A, Mathematical, physical, and engineering sciences*, **362**(1822), 1953–72.
- LaVision Inc. *DaVis Strainmaster*.
- Ledbetter, H. 1993. Dynamic vs. static Young's moduli: a case study. *Materials Science and Engineering A*, **165**(1), 9–10.
- Lewis, JA, Smay, JE, Stuecker, J, & Cesarano, J. 2006. Direct ink writing of three-dimensional ceramic structures. *Journal of the American Ceramic Society*, **89**(12), 3599–3609.
- Li, Y, Xu, Y, & Thornton, C. 2005. A comparison of discrete element simulations and experiments for sandpiles' composed of spherical particles. *Powder Technology*, **160**(3), 219–228.

References

- Lin, XB, & Smith, RA. 1999. Finite element modelling of fatigue crack growth of surface cracked plates: Part I: The numerical technique. *Engineering Fracture Mechanics*, **63**, 503–522.
- Lisjak, a., & Grasselli, G. 2014. A review of discrete modeling techniques for fracturing processes in discontinuous rock masses. *Journal of Rock Mechanics and Geotechnical Engineering*, **6**(4), 301–314.
- Lisle, RJ, & Leyshon, PR. 2004. *Stereographic Projection Techniques for Geologists and Civil Engineers*. Second edn. Cambridge University Press.
- Liu, L., Kafui, K.D., & Thornton, C. 2010. Impact breakage of spherical, cuboidal and cylindrical agglomerates. *Powder Technology*, **199**(2), 189–196.
- Lorentz, E. 2008. A mixed interface finite element for cohesive zone models. *Computer Methods in Applied Mechanics and Engineering*, **198**(2), 302–317.
- Mack, S, Langston, P, Webb, C, & York, T. 2011. Experimental validation of polyhedral discrete element model. *Powder Technology*, **214**(3), 431–442.
- Mahabadi, O. K., Cottrell, B. E., & Grasselli, G. 2010a. An Example of Realistic Modelling of Rock Dynamics Problems: FEM/DEM Simulation of Dynamic Brazilian Test on Barre Granite. *Rock Mechanics and Rock Engineering*, **43**(6), 707–716.
- Mahabadi, O. K., Grasselli, G., & Munjiza, A. 2010b. Y-GUI: A graphical user interface and pre-processor for the combined finite-discrete element code, Y2D, incorporating material heterogeneity. *Computers and Geosciences*, **36**(2), 241–252.
- Mahabadi, O. K., Lisjak, A., Munjiza, A., & Grasselli, G. 2012. Y-Geo: New Combined Finite-Discrete Element Numerical Code for Geomechanical Applications. *International Journal of Geomechanics*, **12**(6), 676–688.

- Majmudar, T., Sperl, M., Luding, S., & Behringer, R. 2007. Jamming Transition in Granular Systems. *Physical Review Letters*, **98**(5), 058001.
- Majmudar, TS, & Behringer, RP. 2005. Contact force measurements and stress-induced anisotropy in granular materials. *Nature*, **435**(7045), 1079–82.
- Michel, B., Sercombe, J., Thouvenin, G., & Chatelet, R. 2008. 3D fuel cracking modelling in pellet cladding mechanical interaction. *Engineering Fracture Mechanics*, **75**(11), 3581–3598.
- Morrell, R, Hendrix, M, De With, G, Vandermeulen, W, Le Doussal, H, Kromp, K, & Rudolph, E. 1999. Young's modulus of ceramic materials - an intercomparison of methods. *Institute of Materials*, **718**(2), 565–566.
- Mueggenburg, NW, Jaeger, HM, & Nagel, SR. 2002. Stress transmission through three-dimensional ordered granular arrays. *Physical Review E*.
- Munjiza, A. 2004. *The Combined Finite-Discrete Element Method*. Wiley.
- Munjiza, A, & Andrews, K R F. 2000. Penalty function method for combined finite discrete element systems comprising large number of separate bodies. *International Journal for Numerical Methods in Engineering*, **49**(January), 1377–1396.
- Munjiza, A., Xiang, J., Garcia, X., Latham, J. P., D'Albano, G. G Schiava, & John, N. W M. 2010. The Virtual Geoscience Workbench, VGW: Open Source tools for discontinuous systems. *Particuology*, **8**(2), 100–105.
- Munjiza, A, Rougier, E, & Knight, EE. 2015. *Large strain finite element method*.
- Nguyen, N. L., Van Buren, V., Von Garnier, A., Hardy, E. H., & Reimert, R. 2005. Application of Magnetic Resonance Imaging (MRI) for investigation of fluid dynamics in trickle bed reactors and of droplet separation kinetics in packed beds. *Chemical Engineering Science*, **60**(22), 6289–6297.

References

- Nguyen, Vinh Phu. 2014. Discontinuous Galerkin/extrinsic cohesive zone modeling: Implementation caveats and applications in computational fracture mechanics. *Engineering Fracture Mechanics*, **128**(C), 37–68.
- O'Hern, C, Langer, S, Liu, A, & Nagel, S. 2001. Force Distributions near Jamming and Glass Transitions. *Physical Review Letters*, **86**(1), 111–114.
- Oliver, C, & Pharr, M. 1992. *An improved technique for determining hardness and elastic modulus using load and displacement sensing indentation experiments*.
- Oliver, W.C., & Pharr, G.M. 2004. Measurement of hardness and elastic modulus by instrumented indentation: Advances in understanding and refinements to methodology. *Journal of Materials Research*, **19**(01), 3–20.
- Palma, V, Ricca, A, Meloni, E, Martino, M, Miccio, M, & Ciambelli, P. 2016. Experimental and numerical investigations on structured catalysts for methane steam reforming intensification. *Journal of Cleaner Production*, **111**, 217–230.
- Paluszny, A, & Zimmerman, RW. 2011. Numerical simulation of multiple 3D fracture propagation using arbitrary meshes. *Computer Methods in Applied Mechanics and Engineering*, **200**(9-12), 953–966.
- Pan, B, Qian, K, Xie, H, & Asundi, A. 2009. Two-dimensional digital image correlation for in-plane displacement and strain measurement : a review. *Meas. Sci. Technol.*, **20**, 1–17.
- Pan, Yihui, Zhan, Yuexing, Ji, Huanyun, Niu, Xinrui, & Zhong, Zheng. 2016. Can hyperelastic material parameters be uniquely determined from indentation experiments? *RSC Advances*, **6**(85), 81958–81964.
- Potyondy, D.O., & Cundall, P.a. 2004. A bonded-particle model for rock. *International Journal of Rock Mechanics and Mining Sciences*, **41**(8), 1329–1364.

- Roohani-Esfahani, SI, Newman, P, & Zreiqat, H. 2016. Design and Fabrication of 3D printed Scaffolds with a Mechanical Strength Comparable to Cortical Bone to Repair Large Bone Defects. *Scientific Reports*, **6**(February 2015), 19468.
- Rostrup-Nielsen, J. R., & Rostrup-Nielsen, T. 2002. Large-scale hydrogen production. *CATTECH*, **6**(4), 150–159.
- Rougier, E, Knight, EE, & Sussman, AJ. 2011. The Combined Finite-Discrete Element Method applied to the Study of Rock Fracturing Behavior in 3D. *In: 45th U.S. Rock Mechanics*.
- Rougier, E, Knight, EE, Broome, ST, Sussman, AJ, & Munjiza, A. 2014. Validation of a three-dimensional Finite-Discrete Element Method using experimental results of the Split Hopkinson Pressure Bar test. *International Journal of Rock Mechanics and Mining Sciences*, **70**(sep), 101–108.
- Roux, St, Hild, F, & Leclerc, H. 2012. Mechanical assistance to DIC. *Procedia IUTAM*, **4**, 159–168.
- Sargent, RG. 2005. Verification and validation of simulation models. . . . *of the 37th conference on Winter simulation*, 130–143.
- Schlereth, D, & Hinrichsen, O. 2014. Comparison of a pseudocontinuous, heterogeneous 2D conductive monolith reactor model to a 3D computational fluid dynamics model. *Industrial and Engineering Chemistry Research*, **53**(28), 11550–11556.
- Schlesinger, S. 1979. Terminology for model credibility. *Transactions of The Society for Modeling and Simulation International*, **32**(3), 103–104.
- Schöllmann, M, Fulland, M, & Richard, HA. 2003. Development of a new software for adaptive crack growth simulations in 3D structures. *Engineering Fracture Mechanics*, **70**, 249–268.

References

- Silling, S. A., Zimmermann, M., & Abeyaratne, R. 2003. Deformation of a peridynamic bar. *Journal of Elasticity*, **73**(1-3), 173–190.
- Silling, S.A. 2000. Reformulation of elasticity theory for discontinuities and long-range forces. *Journal of the Mechanics and Physics of Solids*, **48**(1), 175–209.
- Sitharam, TG. 2000. Numerical simulation of particulate materials using discrete element modelling. *Current Science*, **78**(7).
- Smallman, R. E. 1969. Plasticity of crystals with special reference to metals by E. Schmid and W. Boas. *Acta Crystallographica Section A*, **25**(4), 587–588.
- Song, Y, Turton, R, & Kayihan, F. 2006. Contact detection algorithms for DEM simulations of tablet-shaped particles. **161**, 32–40.
- Stitt, Hugh, Marigo, Michele, Wilkinson, Sam, & Dixon, Tony. 2015. How Good is Your Model? *Johnson Matthey Technology Review*, **59**(2), 74–89.
- Takeuchi, H, Nakamura, H, Iwasaki, T, & Watano, S. 2012. Numerical modeling of fluid and particle behaviors in impact pulverizer. *Powder Technology*, **217**(feb), 148–156.
- Takeuchi, H, Nakamura, H, & Watano, S. 2013. Numerical simulation of particle breakage in dry impact pulverizer. *AICHE Journal*, **59**(10), 3601–3611.
- Tavarez, FA. 2007. *Discrete element method for modelling solid and particulate materials*. Ph.D. thesis, UNIVERSITY OF WISCONSIN-MADISON.
- The MathWorks Inc. *MATLAB*.
- Timoshenko, S. 1970. *Theory of Elasticity*. 3rd editio edn. Mcgraw-Hill College.
- Wagman, D.D., Kilpatrick, J.E., Taylor, W.J., Pitzer, K.S., & Rossini, F.D. 1945. Heats, free energies, and equilibrium constants of some reactions involving O₂,

- H₂, H₂O, C, CO, CO₂, and CH₄. *Journal of Research of the National Bureau of Standards*, **34**(2), 143.
- Wan, Y. 2011. *Discrete Element Method in Granular Material Simulations*. Ph.D. thesis, Technical University of Kaiserslautern.
- Wang, Q. Z., Jia, X. M., Kou, S. Q., Zhang, Z. X., & Lindqvist, P. a. 2004. The flattened Brazilian disc specimen used for testing elastic modulus, tensile strength and fracture toughness of brittle rocks: Analytical and numerical results. *International Journal of Rock Mechanics and Mining Sciences*, **41**(2), 245–253.
- Wang, W, Fu, Z, Wang, H, & Yuan, R. 2002. Influence of hot pressing sintering temperature and time on microstructure and mechanical properties of TiB₂ ceramics. *Journal of the European Ceramic Society*, **22**, 1045–1049.
- Westergaard, H M. 1939. *Bearing pressures and cracks*.
- Wötting, G., & Ziegler, G. 1985. Influence of powder properties and processing conditions on microstructure and mechanical properties of sintered Si₃N₄. *Ceramics International*, **11**(4), 155.
- Xiang, J, Munjiza, A, & Latham, JP. 2009a. Finite strain, finite rotation quadratic tetrahedral element for the combined finite-discrete element method. *International Journal for Numerical Methods in Engineering*, **79**(8), 946–978.
- Xiang, J, Munjiza, A, Latham, JP, & Guises, R. 2009b. On the validation of DEM and FEM/DEM models in 2D and 3D. *Engineering Computations*, **26**(6), 673–687.
- Xiang, J, Latham, JP, & Farsi, A. 2017. *Algorithms and Capabilities of Solidity to Simulate Interactions and Packing of Complex Shapes*. Singapore: Springer Singapore. Pages 139–149.

References

- Zheng, X Y, Lee, H, Weisgraber, T H, Shusteff, M, DeOtte, J, Duoss, E B, Kuntz, J D, Biener, M M, Ge, Q, Jackson, J A, Kucheyev, S O, Fang, N X, & Spadaccini, C M. 2014. Ultralight, Ultrastiff Mechanical Metamaterials. *Science*, **344**(6190), 1373–1377.
- Zhou, Y.C., Wright, B.D., Yang, R.Y., Xu, B.H., & a.B. Yu. 1999. Rolling friction in the dynamic simulation of sandpile formation. *Physica A: Statistical Mechanics and its Applications*, **269**(2-4), 536–553.